ELECTRON IMPACT IONISATION OF MOLECULAR CLUSTERS AND SPATIALLY ORIENTED MOLECULES.

A thesis presented for the degree of

Doctor of Philosophy in Chemistry,

at the

University of Canterbury,

Christchurch,

New Zealand.

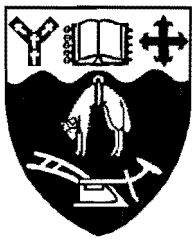

by

Craig George Aitken

1995.

I hear and I forget,

I see and I remember,

I do and I understand.

- Chinese Proverb

If you make every game a life-and-death proposition, you're going to have problems. For one thing, you'll be dead a lot.

- Dean Smith

Abstract

A pulsed supersonic molecular beam apparatus has been used to determine the appearance energies of the cluster ions $(CO_2)_n^+$ $(2 \leq n \leq 4)$, $(N_2O)_n^+$ $(2 \leq n \leq 4)$, $(NH_3)_nNH_4^+$ $(0 \leq n \leq 7)$ and the cluster ion fragments $(N_2O.O)^+$ and $(N_2O.NO)^+$ by electron impact ionisation. The measured appearance energies were used to estimate cluster ion binding energies and to deduce possible mechanisms for the formation of the cluster fragment ions $(N_2O.O)^+$ and $(N_2O.NO)^+$.

A discussion is given on the transformation of the molecular beam machine to accommodate the study of electron impact ionisation of spatially oriented molecules. Characterisation of the inhomogeneous electrostatic hexapole field is described. Electron impact ionisation asymmetry results were measured for CH_3Cl, CH_3Br, CF_3Br and $CHCl_3$ using a quadrupole mass spectrometer and mass insensitive rotatable particle multiplier. Measurement of the asymmetry effect for formation of the molecular ions CH_3Cl^+, CH_3Br^+ and the fragment ions CH_3^+ from CH_3Cl and CH_3Br, CF_3^+ from CF_3Br and $CHCl_2^+$ from $CHCl_3$ are determined and discussed. Each molecule showed a preference for electron impact to occur at the positive end of the molecule. The effect of hexapole voltage and electron energy on the asymmetry effect is also discussed. A simple model is presented for electron impact ionisation at either end of a molecule which accounts qualitatively with the asymmetry results determined.

Acknowledgements

Many people have, in various ways, assisted me with my Ph.D. research and in the preparation of this dissertation. I hope I do not forget anyone that I should have remembered, if I do I am sorry.

I would like to thank Dr. Peter Harland for his guidance, support and friendship in both this research and in other areas. I would like to thank my parents for their continued support even when the light at the end of the tunnel seemed to be a distant flicker (at least it's getting closer now).

The Chemistry Department technicians were invaluable in this research. Without their services and ability to decipher my questions and frequent ignorant requests the research would have come to a standstill many times over. In particular I would like to thank Derek Williams for his electronics expertise, Wayne Mackay for his electrical talents and his willingness to respond to our frequent distress calls and, in particular, Barrie Wood who effectively made the majority of the components described in this dissertation but which my diagrams do not do justice. My friends and colleagues deserve thanks for their friendship and humour they have given over the past years. Without the coffee breaks, discussions, laughter and social occasions I don't think I would have enjoyed it as much as I did.

Financial support from the Chemistry Department and University of Canterbury are gratefully acknowledged.

Finally I would like to thank Mandy Anderson for her support and friendship. By being there is more than enough.

Table of Contents

List of Figures

List of Tables

Chapter 1

Introduction

This dissertation presents a number of new results concerning the appearance potentials of atomic and molecular van der Waals clusters by electron impact ionisation and also presents a new extension to the field of spatially oriented molecule collisions by determining the effect of spatial orientation on electron impact ionisation. The purpose of this chapter is to describe how these studies evolved and to provide a short outline of each subsequent chapter presented in this dissertation.

The initial objective of the research programme was to determine if there was any asymmetry towards electron impact ionisation of spatially oriented molecules. To achieve this objective, extensions to the existing molecular beam machine to facilitate the inclusion of the hexapole rod assembly were required. Fortunately, while the new extensions were being constructed within the Department, I was able to be associated with the determination of appearance potentials of small positive cluster ions. These measurements represented the final stage of the old molecular beam machine and the beginning of a new research area for this laboratory.

The extension of the existing molecular beam machine, to include the hexapole rod assembly, involved the addition of two extra chambers to the machine and was completed in July 1991. Comprehensive characterisation of the molecular beam machine was completed, using the available range of symmetric top molecules, to confirm that the hexapole electrostatic filter was operating correctly and to determine the most likely molecular species to use initially in the electron impact ionisation asymmetry studies.

Planned major modifications to the molecular beam machine included construction of a new frame and scattering chamber. The construction had been on-going for two and a half years with the change to the new machine design being prompted by a mechanical pump failure. The disassemble, cleaning and reassemble of the molecular beam machine onto the new frame required four months and was operational in October 1993.

Asymmetry measurements had been performed in the previous two years but the results had high associated errors and were non-reproducible. Reproducible asymmetry measurements were obtained, following the major modifications to the machine, over a year period using both a thermal ion detector and a quadrupole mass spectrometer at different stages throughout the year.

The preceding paragraphs have given a brief overview of how the different areas of this dissertation merged together and a general time line of the evolution of the molecular beam machine. It is now appropriate to give a brief outline of the content of the following chapters.

Chapter 2 provides an introduction to the general principles of beam production, ionisation, detection and hexapole state selection. Section 2.1 introduces the previously reported oriented molecule research and summarises the transition from the first atom-oriented molecule collisions through to the probing of the electron transfer step in the harpoon mechanism and the subsequent direct probing of electron impact ionisation asymmetry reported here. Sections 2.2 through 2.5 were designed to be specific for the experimental configuration used during this dissertation.

Chapter 3 describes the main constructional features and vacuum components at each stage of the molecular beam machine development. It is split into three stages which correspond to the machine used to study the appearance potentials of clusters, the initial extension and characterisation of the hexapole and, finally, the major modifications and transition to the new frame.

Chapter 4 reviews the appearance potential measurements on the cluster ions $(CO_2)_n^+$ and $(N_2O)_n^+$ $(2 \leq n \leq 4)$, $(NH_3)_nNH_4^+$ $(0 \leq n \leq 7)$ and the cluster ion fragments $(N_2O.O)^+$ and $(N_2O.NO)^+$ from electron impact ionisation [Cameron 1994]. The results are in general agreement with previously reported appearance potentials with the appearance potentials of $(N_2O.O)^+$ and $(NH_3)_nNH_4^+$ $(3 \leq n \leq 7)$ being determined for the first time.

Chapter 5 discusses the effect of orientation on electron impact ionisation and fragmentation. This represents a new area of research with no previous reports of direct electron impact ionisation of spatially oriented molecules. Section 5.1 describes the data collection and data analysis used for the results presented in Sections 5.2 through 5.4. In Sections 5.2 and 5.4 the results obtained from an Amptektron thermal ion detector are presented and in Section 5.3 the results from a quadrupole mass spectrometer are presented. The comparative analysis between each of the Sections 5.2 through 5.4 are presented in Section 5.5 with a description of the additional experimental tests used to verify the asymmetry measured was not an anomaly. The results are qualitatively consistent with electron impact ionisation being more favourable at the positive CH_3-end of CH_3Cl than the negative Cl-end [Aitken 1994]. Section 5.6 introduces a simple model which qualitatively agrees with the asymmetry results measured.

Chapter 6 is the final chapter of this dissertation and provides a summary of the results presented in Chapters 4 and 5 and offers some suggestions for future directions for oriented molecule research.

Chapter 2

General Principles

The purpose of this Chapter is to introduce the general techniques, theory and background of atomic and molecular beam production, detection and state selection to form spatially oriented molecular distributions which are specifically used in Chapter 3.

Section 2.1 gives a brief review of reaction dynamics involving oriented molecules with an emphasis on the hexapole electrostatic field technique. Section 2.2 describes molecular beam production using supersonic nozzles and Section 2.5 discusses the detection principles of the quadrupole mass spectrometer, one of the detectors used in this dissertation. Section 2.3 offers some background theory towards understanding electron impact processes, specifically electron impact ionisation. Section 2.4 describes the principles behind state selection in the hexapole electrostatic field and, consequently, the spatial orientation of the state selected molecules in a homogeneous electric field.

Each of the following sections are specific to the techniques used in this study. There are, of course, many other techniques for beam production, beam detection, spatial orientation and other, more advanced theories, for electron impact ionisation which are beyond the scope of this dissertation.

2.1 Previous Research

The relative spatial orientation of molecules in a reaction and the idea of steric requirements is intuitive and second only to the energetic requirement for a successful reaction. The steric factor ρ is included in the pre-exponential factor for the reaction rate constant and represents the fraction of collisions in which the reagents are properly oriented. However, because of the variability of the steric factor value, it is often considered a fudge factor which merely brings experiment and theory together. Similarly, with the activated complex theory the orientation consideration still survives as the entropy of activation.

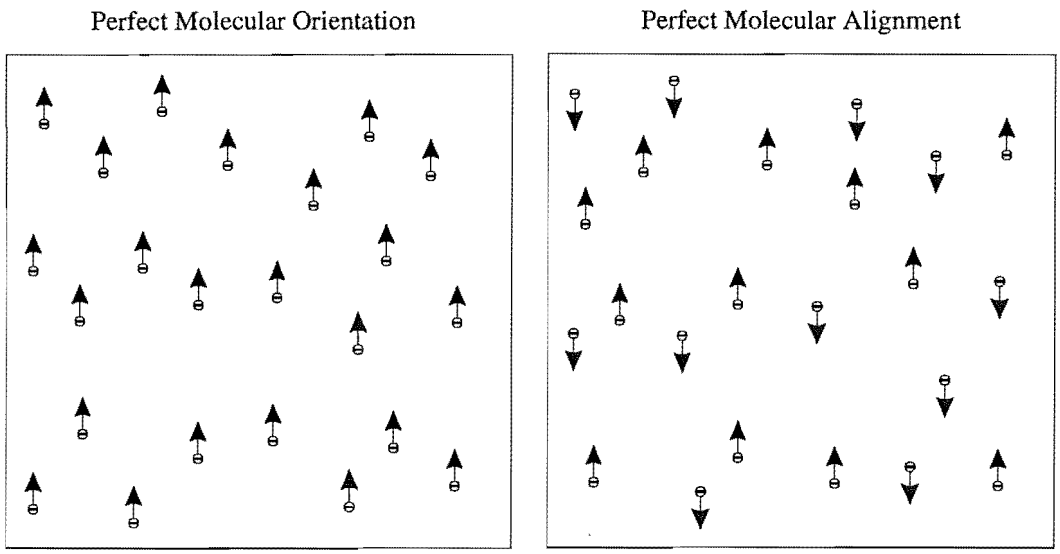

Figure 2.1.1: Perfect molecular orientation requires the electric dipole to be pointing in one direction. Perfect molecular alignment can have the direction of the dipole parallel or antiparallel.

Steric effects in molecular reactions are also supported by a variety of indirect evidence, most notably the Walden inversion or S_N2 reaction mechanism. The desire to obtain direct evidence and to improve the theoretical concept of potential energy surfaces requires control of the orientation of the reactant molecules. To measure the steric effect a requirement is to form an orientation distribution and also to keep the distribution throughout the reaction. The advent of molecular beams and their collision free nature (Section 2.2) presented the opportunity to acquire direct experimental evidence for a steric effect by eliminating re-orienting collisions.

Methods to study the steric effect fall into two categories: alignment and orientation methods. Alignment methods compare parallel or antiparallel (can not differentiate between the two) to broadside spatial distributions. Orientation methods compare parallel to antiparallel to broadside spatial distributions. The difference between the methods is shown graphically for a molecule with an electric dipole in Figure 2.1.1.

Alignment methods using polarised laser excitation of diatomics [Karny 1978, de Vries 1982, de Vries 1983, Hoffmeister 1987] and atoms [Rettner 1982] have been used to study the effect of molecule and orbital alignment on product state distribution and reactivity. Alignment methods give valuable steric information but, if the molecule is asymmetric with distinguishable ends, then alignment methods possibly miss the main steric effect. For this reason only orientation methods shall be considered further.

At the present time the major technique for orienting molecules involves the selection of specific rotational states in higher Stark states by a six-pole electrostatic hexapole field and subsequent orientation in a homogeneous electric field. The hexapole technique can only orient symmetric top molecules or pseudo-symmetric top molecules.

These include some asymmetric top molecules, linear polyatomic molecules excited in bending vibrations (N_2O) and diatomics with electronic angular momentum (NO). The theory of the hexapole technique is explained in Section 2.4 and experimental studies using the hexapole are reviewed later in this section.

Orientation methods are not solely constrained to the use of hexapole fields. Polanyi *et al* has taken advantage of constrained geometry and studied reactions of species oriented and trapped on a surface [Polanyi 1988]. Similarly, reactions within the van der Waals adduct have been studied [Scherer 1987, Buelow 1987, Jouvet 1987] where the formation of van der Waals clusters, from supersonic nozzle expansions (Section 2.2), constrains a molecular geometry relative to its cluster partner. Formation of reagent molecules with a defined geometry in a molecular cluster and then optically exciting the adduct to trigger the reaction has been used by Zewail and co-workers to observe the dissociation of the collision complex in real-time [Scherer 1987].

The brute force method of orientation [Loesch 1990, Friedrich 1991, Loesch 1991, Loesch 1992] requires a strong homogeneous electric field within the reaction volume to physically twist the molecules into a statistical rotational state orientation distribution. Previously the brute force method was impractical [Brooks 1976] because of the extremely high voltages required to overcome the thermal rotation of the molecules in an effusive beam. However, with the advent of supersonic nozzle beams, where the molecules are highly relaxed (Section 2.2) and only low total angular momentum J-states are populated (hence low rotational temperatures), moderate electric fields of ~ 1 MVm^{-1} [Loesch 1990] can achieve adequate orientation.

The advantage of the brute force method is that it can orient any molecule with a permanent electric dipole including symmetric top molecules and diatomics. The disadvantage of the method is that it requires a high electric field within the scattering volume which limits the versatility of the method towards charged particle reactions.

Loesch and co-workers have tested the brute force method with K + oriented CH_3I [Loesch 1991], where well known steric properties exist from hexapole experiments, and found similar steric behaviour with previous results. Following this the three centre K + oriented ICl reaction was studied where asymmetry was observed in product species and product scattering distribution [Loesch 1992]. Only the brute force technique can orient ICl at this time.

Although each of the above orientation techniques have unique advantages the hexapole technique has become the most widely used and versatile technique to spatially orient molecules. The history and development of the hexapole technique is considered below.

In 1955 Bennewitz *et al* [Bennewitz 1955] showed theoretically that a six-pole electric field would be suitable for focusing polar symmetric top molecules via the first order Stark effect. At the time it was thought that individual rotational states could not be separated, unlike polar diatomics in a quadrupole field [Bennewitz 1955], because of the additional M quantum number (projection of the total angular momentum, J, about

the space fixed or electric field axis) giving rise to a larger number of rotational states populated at normal effusive beam temperatures.

Kramer and Bernstein [Kramer 1965] experimentally demonstrated the focusing effect of enhanced signal with increasing hexapole voltage for CH_3I and CHI_3 molecules. The first asymmetric studies involving oriented molecules were simultaneously completed by two groups: Brooks *et al* [Brooks 1966] studying the K + oriented CH_3I reaction and Bernstein *et al* [Beuhler 1966] studying the Rb + oriented CH_3I reaction. Both groups used differential surface ionisation to detect the scattered KI or RbI product. Both studies showed marked asymmetry with the reaction being more favourable when the alkali atom was incident on the iodine end of the molecule. It also showed that a direct Rb/K-I collision was probably required for reaction with the Rb reaction having a cone of non-reaction of ~ 53° about the CH_3-I axis for reaction at the CH_3-end of the molecule [Choi 1985]. These results agreed with previous crossed beam studies of K + random CH_3I [Herschbach 1961] which showed a small angle of ejection of backward scattered KI product from the centre of mass, and a small total reaction cross section, which indicated a direct K-I collision being required for reaction.

Experimental investigation of the asymmetric nature of reaction mechanisms then split into two different paths: one of creating a beam of pure JKM rotational states, to gain greater specificity, and the other of studying reactive asymmetry with an average orientation population.

Bernstein and co-workers concentrated on the analysis of the orientation distribution produced by a hexapole field [Stolte 1982a, Choi 1985, Levine 1986] and on improving the experimental characteristics to provide pure JKM rotationally state selected molecules [Gandhi 1986, Gandhi 1987a]. This was achievable through the development and use of supersonic nozzle beams instead of the thermal effusive beams used in the initial studies. Obtaining specific JKM rotational state selection [Gandhi 1986] gave Bernstein and co-workers the opportunity of measuring the degree of orientation for a range of symmetric top molecules using laser-induced photofragmentation [Gandhi 1987b, Xu 1988, Gandhi 1988a, Xu 1989] and to measure the retention of orientation in DC electric fields [Gandhi 1988a]. With the greater specificity of Bernstein's machine there was no scope to study reactive oriented beam systems similar to the initial Rb + oriented CH_3I because of the reduced beam intensity from state selection.

Brooks and co-workers, however, continued with their reactive asymmetry studies. They followed the K + oriented CH_3I work with K + oriented CF_3I [Brooks 1969a, Brooks 1973] and in determining the focusing behaviour of other symmetric top and asymmetric top molecules [Brooks 1969b, Jones 1970]. The results from the K + oriented CF_3I reaction were found to be quite different from the K + oriented CH_3I results. In the CF_3I case the KI product was found to be scattered into both backward and forward centre of mass angles for K approaching the I-end and CH_3-end respectively. The reaction probability was roughly equal in both orientations. For K + oriented $(CH_3)_3CI$ [Marcelin 1975] results were similar to the K + oriented CH_3I reaction

with only backward scattered KI products preferentially formed when the K attacks the I-end of the molecule.

The difference in scattered product for the K + oriented CF_3I reaction was qualitatively interpreted by the harpoon mechanism [Magee 1940] where there is initially an electron transfer (harpoon) from the alkali atom to the molecule at large internuclear separations, dissociation of the molecular negative ion ejecting I^- in the direction which it was pointing and then positive-negative ion recombination to form the neutral KI product. To test the harpoon model Brooks and co-workers reacted K + sideways oriented CF_3I [Brooks 1979]. Electron transfer for the harpoon mechanism should be independent of orientation in this case which was experimentally confirmed in support of a harpoon mechanism.

Studies on K + oriented CF_3Br [Carman 1986] gave results consistent with the K + oriented CF_3I reaction. However, in the CF_3Br case it was found that the reaction on the Br-end was about threefold more reactive than the CF_3-end of the molecule. It was proposed that the difference in reactivity for the two ends of CF_3Br resulted from either the precession of the CF_3Br molecule inhibiting the recombination of KBr or because the initial electron transfer step was orientation dependent.

Many new groups began using the hexapole field to orient molecules through the 1980's with better state selection, detection techniques and analysis becoming available. Van den Ende and Stolte studied the chemiluminescence reaction $NO + O_3 \rightarrow NO_2^* + O_2$ [van den Ende 1982, van den Ende 1984] by state selecting the $^2\Pi_{3/2}$ state of NO via its electronic angular momentum. The orienting electric field is either directed parallel or antiparallel to the NO relative velocity in order to collide the NO molecule N-end or O-end with O_3 in the scattering volume [van den Ende 1984]. In two different apparatus [van den Ende 1982] the relative chemiluminescence cross sections for NO_2^* were measured for each M_J state of NO and the angular distribution of NO_2 from oriented NO was measured giving evidence for a direct reaction with two different reaction mechanisms leading to products: a direct collision giving backward scattered product and a broadside collision giving sideways scattered product [Parker 1987].

Stolte and co-workers have also measured the chemiluminescence of BaO^* from Ba + N_2O where vibrationally excited N_2O is oriented by a hexapole field. Through a series of studies [Jalink 1986a, Jalink 1986b, Parker 1987] Stolte and co-workers have investigated the dependence of chemiluminescence on internal excitation of the N_2O molecule and the dependence of the BaO^* chemiluminescence polarisation on the N_2O orientation. Similar work has been completed for the chemiluminescence reaction of $Ca^* + CH_3X \rightarrow CaX^* + CH_3$ with X being F, Cl or Br [Janssen 1991].

Kuwata and co-workers have studied the chemiluminescence of CF_3^* and CN^* from Ar^*+ oriented CF_3H [Ohoyama 1987] and oriented CH_3CN [Kasai 1989] respectively. In each case it was found that Ar^* impinging on the CF_3-end or CN-end of the oriented molecule gave increased chemiluminescence emission.

The work by Brooks and co-workers on the K + oriented CF_3I and K + oriented CF_3Br reactions were partially explained by the harpoon mechanism with the suggestion that the initial electron jump step could be orientation dependent. To determine whether this was the case Brooks and co-workers studied collisions of fast K atoms with oriented molecules [Harland 1989, Harland 1990, Harland 1991, Brooks 1992]. These reactions produce K^+ and either the molecular negative ion, or a halide negative ion, which removes any pseudo-orientation effects from the recombination, ionisation or detection processes for KX as encountered in previous studies. It was found that for all molecules the most reactive orientation involves the end that ejects the negative ion being directed towards the fast K beam. This, however, can still be explained by an exit channel effect with the K^+ and halide negative ion trajectories being in an antiparallel formation and so giving a higher probability of K^+ escaping and being detected by the channeltron multiplier. Preliminary results for K^+ formation near threshold indicated a significant orientation effect in the threshold energy for ion formation indicating that orientation effects are important in the entrance channel [Harland 1991].

In order to further appreciate the entrance channel effect of electron transfer, fast K atoms + oriented molecules were studied more accurately to threshold [Xing 1994]. For the CF_3Br reaction, energies below 4.04 eV were found to produce only the parent molecular ion CF_3Br^-. It was determined that impact on the Br-end of CF_3Br has a lower threshold, with reaction only occurring at the Br-end for energies between 3.4-4.0 eV [Xing 1994] indicating that the electron is transferred preferentially to the Br-end of the molecule.

Application of the hexapole technique for oriented molecules includes determination of the orientation dependence of collisional cross sections [Stolte 1972, Stolte 1973], photoionization [Kaesdorf 1985], electron scattering [Volkmer 1992, Bowering 1994, Meier 1994], indirect electron impact ionisation [Kasai 1993], surface absorption [Kuipers 1989, Tenner 1988], scattering from surfaces [Curtiss 1989, Curtiss 1990, Kuipers 1988, Tenner 1988, Kuipers 1989], the characterisation of supersonic beam clusters [Ohashi 1988] and, in this dissertation, the electron impact ionisation and fragmentation of CH_3Cl [Aitken 1994].

At this time the number of studies which use oriented molecules is small. The continued improvement of existing techniques, and development of new techniques and applications, will expand the knowledge of the steric effect and increase the experimental control over the dynamics of the reaction mechanism.

2.2 Beam Production

The feasibility of all beam experiments is dependent on the vacuum system minimising the density of background gas molecules within the collision region or cross beam region. Conjointly with the need to reduce the vacuum background density is the requirement to provide the greatest possible beam density at the detector.

Most thermal energy beam sources utilise a flow system where the beam material flows as a gas or vapour from an oven into a chamber of lower pressure. Collimation is then used to produce a final well defined beam in the collision chamber. This type of source can operate under two different regimes [Fluendy 1973] depending on the value of the Knudsen number, K_n, where

$$K_n = \frac{\text{mean free path in source}}{\text{smallest dimension of source orifice}}$$

and where the mean free path is given by

$$\lambda = \frac{1}{\sqrt{2}\,\sigma n}$$

with σ the collision cross section and n the background particle density.

If $K_n>1$ then the source is referred to as an effusive source and if $K_n<1$ then it is referred to as a hydrodynamic or supersonic source.

2.2.1 Effusive Sources

The earliest type of source was the effusive source where the vapour leaves the oven or source chamber through a narrow slit. The gas pressure in the source is adjusted to keep the Knudsen number greater than one, so the beam molecules exit the slit without undergoing collisions.

Under effusive conditions the number of molecules exiting the source per second in solid angle $d\omega$ at an angle θ relative to the source normal is [Fluendy 1973]

$$dQ = \left(\frac{d\omega}{4\pi}\right) n\bar{v}A_s\cos\theta$$

where n is the number density in the source chamber, $\bar{v}$ is the mean velocity in the source chamber and A_s the area of the exit orifice. Integrating over the spherical co-ordinates $\phi(0 \rightarrow 2\pi)$ and $\theta(0 \rightarrow \pi/2)$ and with $d\omega = \sin\theta d\theta d\phi$, the total number of molecules exiting the source per second becomes

$$Q = \frac{n\bar{v}A_s}{4}.$$

Inside the source the particle velocities are in accordance with the Maxwell Boltzmann velocity distribution

$$f_{MB}(v) = \frac{4}{\sqrt{\pi}}\frac{1}{\alpha^3}v^2\exp\left(-\frac{v^2}{\alpha^2}\right)$$

where $\alpha = \sqrt{\frac{2kT}{m}}$ is the most probable molecular velocity within the source.

The probability of a molecule exiting the source is dependent on the velocity of the molecule since faster molecules have a greater probability of crossing the source plane in a given time. The velocity intensity distribution of the beam is then proportional to the Maxwell Boltzmann distribution multiplied by the velocity, with the proportionality constant determined by normalising the beam velocity distribution over all velocities. The velocity distribution within an effusive beam then becomes

$$f_b(v) = \frac{2}{\alpha^4} v^3 \exp\left(-\frac{v^2}{\alpha^2}\right) = \left(\frac{v}{\bar{v}}\right) f_{MB}(v).$$

The advantage of the effusive source is that it has a well defined and easily calculable velocity distribution and intensity. However, the disadvantage of the effusive source is that the broadness of the velocity distribution requires velocity selection which diminishes the intensity of the beam species.

2.2.2 Hydrodynamic (Free Jet) Sources

To overcome the intensity limitations of the effusive beam source Kantrowitz and Grey [Kantrowitz 1951] suggested the replacement of the Maxwellian gas inside the effusive source by a jet of gas already moving in the beam direction. The hydrodynamic source or supersonic source was shown to yield intensities several orders of magnitude greater than those obtainable from an effusive source [Kistiakowsky 1951].

The supersonic source is formed from the expansion of gas from a region of high pressure (10^2-10^3 torr), through a small orifice, into a low background pressure (10^{-6}-10^{-8} torr). The nozzle exit diameter is significantly greater than the mean free path of the molecules within the source (K_n<1). The pressure difference between the source and the background accelerates the molecules towards the source exit. As the molecules pass through the nozzle they experience a large number of collisions with the most effective collisions serving to drive the molecules out of the source, i.e. those that have a large component of velocity perpendicular to the source plane. This results in the random motion of the molecules in the source being converted to directed mass flow along the beam axis which is observed as a narrowing of the beam velocity distribution and a cooling of the random motion or temperature within the beam.

The basic form of the expansion is shown in Figure 2.2.1. The Mach number, M, is defined as the ratio of the mean velocity within the source, u, to the local speed of sound, a

$$M = \frac{u}{a}$$

where $a = \sqrt{\frac{\gamma kT}{m}}$ and γ is the ratio of the heat capacities, $\gamma = \frac{C_p}{C_v}$.

At the source exit the Mach number is equal to one and the gas flow expands to meet the boundary conditions imposed by the background gas pressure [Scoles 1988]. As the gas expands the beam velocity becomes greater, the beam rapidly cools (so

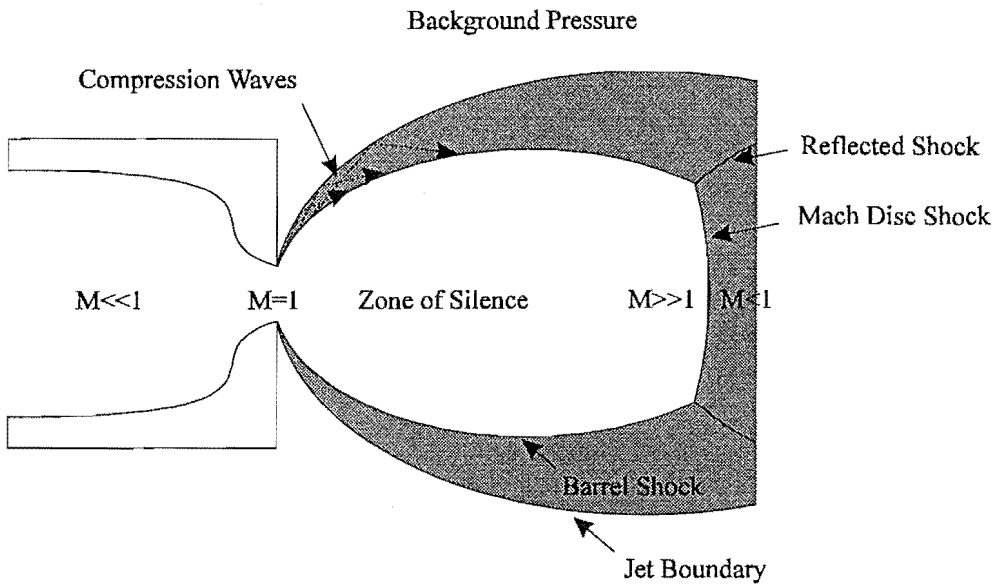

Figure 2.2.1: The form of a supersonic expansion indicating the major components of the expansion structure. From the nozzle source the gas expands forming a shock wave which attaches to the skimmer (not shown) situated in the zone of silence region.

decreasing the local speed of sound) and so the Mach number becomes greater than one. As the Mach number increases the formation of shock waves, thin regions of high density, pressure, temperature and velocity gradients, occur to satisfy the boundary conditions of the expansion. The barrel shock and Mach disc shock (Figure 2.2.1) would ultimately thermalise the beam further downstream of the nozzle if not for a hyperbolic cone or skimmer which doubles as the first collimation device for the beam. The skimmer tip is placed in the zone of silence region of the expansion, upstream of the Mach disc, and allows the attachment of the barrel shock onto the skimmer surface. The surrounding barrel shock forms a high density cylinder that the thermal background molecules cannot penetrate to degrade the beam. The skimmer shape also prevents beam degradation by reflecting background and beam molecules, impinging on the surface, away from the collimated beam axis.

The position of the nozzle with respect to the skimmer surface is important for correct formation of the flow properties of the expansion. If the nozzle is too far from the skimmer then the barrel shock and the Mach disc shock will thermalise the expansion and disrupt the flow characteristics of the beam. If the nozzle is too close to the skimmer then the skimmer will act as a virtual source and the beam will have effusive beam characteristics. The optimum nozzle-skimmer distance is determined by experiment and is discussed in Section 3.3.13.

The final stage of the expansion is when the gas density of the beam decreases to a point where effectively no further collisions occur (i.e. the mean free path for collision within the beam is longer than the experimental apparatus) and the flow is considered to be free molecular (this situation is generalised as there will always be collisions between

the beam and background molecules and between beam molecules due to the finite width of the beam velocity distribution).

The two major characteristics of the supersonic nozzle expansion is the directed flow and cooling of the beam. The directed flow of the beam increases the fraction of the beam that is available to the scattering volume. The reduction in beam temperature reduces the width of the velocity distribution so that no velocity selector is required and also reduces the number of collisions to free molecular. Both characteristics combine to increase the usable beam density within the scattering volume.

For an ideal gas, the flow velocity u, is related by conservation of energy to the enthalpy change of the gas

$$\frac{1}{2}Wu^2 = \int_{T_o}^{T_s} C_p dT$$

where W is the molecular weight of the beam species, T_o the final beam temperature and T_s the source temperature.

If the heat capacity, C_p, is assumed to be constant over the temperature range $T_s \rightarrow T_o$ and which, for an ideal gas, is given by

$$C_p = \left[\frac{\gamma R}{(\gamma - 1)}\right]$$

then the maximum velocity [Scoles 1988] obtainable by the beam species is

$$u_\infty = \sqrt{\frac{2R}{W}\left(\frac{\gamma}{\gamma - 1}\right)T_s}$$

where $T_o << T_s$ since the beam is cooled during the expansion. In terms of the Mach number the ratio of final beam temperature to the source temperature can be determined [Scoles 1988] as

$$\frac{T_o}{T_s} = \left[1 + \frac{1}{2}(\gamma - 1)M^2\right]^{-1}. \qquad (2.2.1)$$

For argon [Cameron 1993] typically $M \sim 25$ which gives a degree of cooling of $\frac{T_o}{T_s} \sim 0.005$.

The velocity distribution for a supersonic expansion is not fully understood but is assumed to be a three dimensional Maxwell Boltzmann distribution for the final beam temperature superimposed on the mean flow velocity u

$$f_s(v) = N\left(\frac{v}{\alpha_s}\right)^2 \exp\left(-\frac{(v-u)^2}{\alpha_s^2}\right) \qquad (2.2.2)$$

where

$$\alpha_s = \sqrt{\frac{2kT_o}{m}}$$

is the most probable random velocity in the beam, and where u and T_o can be determined by fitting Equation 2.2.2 to experimentally measured arrival time distributions [Cameron 1993].

The narrow velocity distribution for the supersonic beam source compared to the effusive beam source is shown in Figure 2.2.2 for argon (u=557 ms^{-1}, T_o=2 K and $\gamma = 1.666$). For polyatomic beam molecules there is rotational and vibrational as well as translational cooling. However, the degree of cooling for polyatomic species is less than for monatomic species as $\gamma \rightarrow 1$ for polyatomics in Equation 2.2.1 and so the velocity distribution is broadened.

The multiple collisions between the nozzle gas species during the expansion process results in all the beam molecules tending towards the same velocity. If a few percent of a seed gas is mixed with a buffer gas then the seed gas obtains nearly the same velocity and temperature as the buffer gas in a supersonic expansion (the equations stated above are equally applicable to a mixture by replacing C_p and W by the respective molar average values $\bar{C}_p = \Sigma X_i C_{p_i}$ and $\bar{W} = \Sigma X_i W_i$ where X_i is the mole fraction of species i). Depending on the individual masses of the buffer and seed gas species the energy of the seed can be well above or below that obtainable in a pure beam. Usually noble carrier gases are chosen as the buffer or carrier gas since they are chemically inert and they are more effective in the conversion of random translational motion into mass flow. A further consequence of seeding molecules in a buffer gas is hydrodynamic focusing. Because of the pressure gradients in the expanding jet the hydrodynamic focusing effect causes the concentration of the heavier species onto the beam axis, resulting in a higher beam intensity for the heavier species at the detector.

Another aspect of the supersonic expansion is the formation of molecular clusters within the beam. If the temperature within the nozzle exit is low enough while the beam density and collision frequency still remains high, then the beam species may condense and form clusters, which are bound by weak van der Waals forces. Since Becker *et al* [Becker 1956] first experimental observation of the formation of atomic clusters it is now possible to virtually form any variety of clusters containing either pure species or a mixture of species. Cluster size can vary from simple dimers through to hundreds of monomer units. The determination of cluster size distributions has been intensified recently by the observation of enhanced signal intensity for specific cluster sizes which has been attributed to the existence of particularly stable geometries, e.g. $NH_4^+(NH_3)_4$, $H_3O^+(H_2O)_3$, C_{60} and C_{70}. However, the determination of cluster size distributions is made difficult by the fragmentation of the cluster ion during ionisation. Appearance energies of molecular clusters are discussed further in Chapter 4.

Nozzles can be operated in two modes: pulsed or continuous. The experimental situation determines which of the modes is best suited. During an experiment the

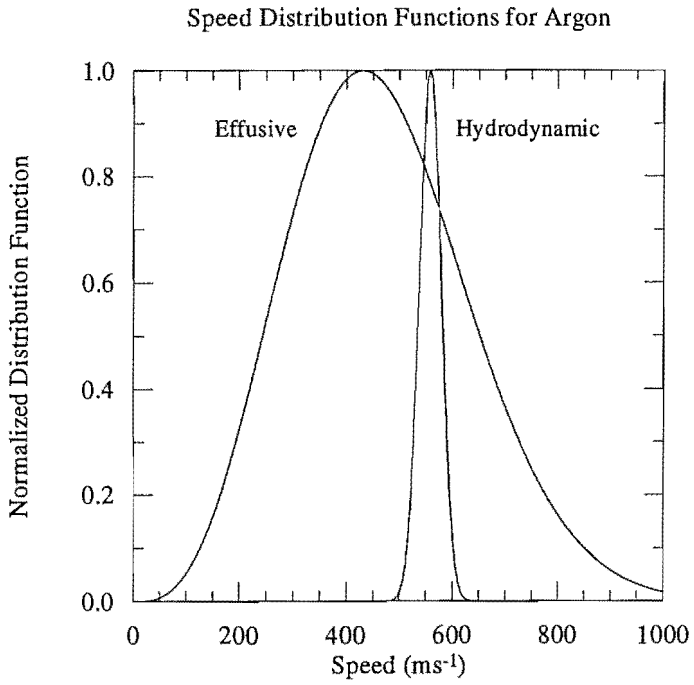

Figure 2.2.2: Speed distributions for argon using effusive and hydrodynamic sources. The beams originate at a source temperature of 298 K. The hydrodynamic or supersonic source has beam characteristics u=557 ms^{-1}, T_o=2 K and γ=1.666.

residual gas pressure within the chambers can not exceed the pumping capacity of the vacuum pumps, hence this limits the backing pressure that can be used. In pulsed nozzle operation much higher backing pressures can be used while keeping the residual background pressure low, or lower pumping speed can be used for the same backing pressure. One disadvantage of the pulsed nozzle operation is the low duty cycle of the nozzle (typically about 1 ms open time at 10 Hz). However many systems use low duty cycles for pulsed lasers or pulsed detection so this disadvantage is dependent on the experimental conditions. Possibly the main disadvantage of pulsed beams is that the beam characterisation, especially cluster size, velocity and temperature, are not uniform throughout the pulse [Scoles 1988] because of the finite time required for complete expansion.

The useful energy range of the supersonic source, even with seeding techniques, is still less than one electronvolt. For higher energy beams a more specialised beam source is required (e.g. a plasma jet or charge exchange beam source). However the supersonic nozzle source is probably the most widely used source in molecular dynamics.

2.3 Electron Impact Processes

Electron impact ionisation of atoms and molecules has been known since the early 1900's with quantitative measurements of total ionisation cross sections measured using various experimental methods from the 1920's [Tate 1932, Fite 1958]. Despite this relatively early beginning there is still no definitive theoretical treatment of the electron impact ionisation process and only fragmentary calculations of electron impact ionisation fragmentation patterns (mass spectra).

The major electron impact ionisation process is a direct single step ionisation [Ehrhardt 1986]

$$e^- + A \rightarrow A^+ + e^- + e^-.$$

A typical ionisation cross section curve exhibits three distinct regions; zero ionisation cross section until the electron energy reaches the ionisation potential, an increasing ionisation cross section until reaching a maximum around 50-100 eV and, finally, a gradual decline of the ionisation cross section as the electron energy is further increased [Field 1957]. Special features of the ionisation cross section, such as linearity above the threshold and fine structure from ionisation to different electronic states, are not of a concern for this dissertation. The general features of the ionisation cross section can be qualitatively understood by determining the transference of energy required for the transition between two given electronic states. When the electron energy is near the ionisation potential then the transference must be such that all the energy is transferred to the molecular system and, crudely, it can be thought that the electron must strike the exact centre of the system. As the electron energy is increased then only a fraction of the electron's energy must be transferred and so glancing impacts will result in ionisation with an associated increase in the ionisation cross section [Field 1957]. Field also gives a rationale for the decrease in ionisation cross section as the electron energy is increased beyond the maximum: the passage of the bombarding electron subjects the molecule to a pulsed disturbance with the probability of the molecule absorbing energy sufficient for ionisation being dependent on the magnitude of the Fourier component in the pulse which is in resonance with the energy change in the molecule. As the electron energy increases the pulse narrows and the magnitude of the lower frequency components in it decrease with a resultant decrease in the ionisation cross section [Field 1957]. From these initial qualitative theories there had been limited theoretical models developed for the ionisation process until the last 20 years with the measurement of accurate experimental data.

For electron impact ionisation of an atom at high impact energies (electron energies greater than ten times the ionisation potential) there are two outgoing electrons. One being a fast scattered electron which, considering particle and momentum exchange being negligible at high impact energies, has nearly all the excess energy and is scattered into the forward direction about a narrow angular cone around the direction of the initial incoming electron. The second electron is a slow ejected electron which is ejected uniformly in all directions [Ehrhardt 1986].

The theoretical treatment of the ionisation process is a complex problem with the involvement of three charged particles in the final exit channel [Ehrhardt 1986]. Even for the simplest ionisation involving atomic hydrogen the long range Coulomb force forbids free motion of the particles even at infinite interparticle separation [Brauner 1989].

Experimental and theoretical development of electron impact processes (electron scattering and ionisation) first began in the 1930's when electron diffraction was used to investigate molecular structure (see [Massey 1969, Ehrhardt 1986] for a review of early experimental and theoretical development). The theoretical description of the electron impact processes have improved in recent years with the development of more accurate experimental methods. The two experimental methods mentioned here are triply differential cross sections for electron impact ionisation and elastic electron scattering from oriented molecules.

Electron impact ionisation triple differential cross sections are explicit functions of all collision parameters such that all outgoing momenta of the three particles are specified [Ehrhardt 1986, Brauner 1989]. The majority of triple differential cross sections have been measured for hydrogen atoms [Brauner 1989] and helium [Srivastava 1988] since these simple systems can determine the ranges of validity for the various theoretical models in the description of the collision mechanism [Ehrhardt 1986].

Elastic electron scattering of oriented molecules has only been a recent advance [Volkmer 1992, Bowering 1994, Meier 1994]. By spatially orienting symmetric top molecules, using an electrostatic hexapole filter and homogeneous electric field, measurement of the electron scattering elastic differential cross section for each orientation can be determined. The scattering of electrons from a molecule depends on the potential of the charge distribution within the molecule [Bowering 1994]. Elastic electron scattering from oriented molecules then offers the possibility of obtaining three dimensional information, similar to that obtained from x-ray diffraction, from the electron diffraction patterns [Volkmer 1992].

Theoretical models have been developed to reproduce the various scattered electron intensities from electron impact ionisation and elastic electron scattering results. The complexity of the models has been greatly increased, especially for electron impact ionisation, as different modified potentials, for the ions and electron particles in the entrance and exit channels, are developed to better approximate the scattering data [Ehrhardt 1986]. However, for this dissertation, the complexity is reduced somewhat as the interest is based not on the scattered electrons but on the incoming or bombarding electron for electron impact ionisation.

The initial models for electron impact ionisation were based on the first Born approximation which represented the incoming electron as a plane wave and assumes that there is limited interaction between the incident electron and the target atom [Bates 1974]. The first Born approximation did not predict fully the experimental data at the time [Ehrhardt 1986] which saw the development of other higher order models with the

incident electron being described by a distorted wave calculated in the field of a neutral atom [Jones 1993].

Although the representation of the incident electron may change, the theory for the ionisation process has remained effectively the same. For electron impact ionisation at high electron energies (greater than ten times the ionisation potential) the fast moving electric field of the impinging electron induces a perturbation in the electronic state with the interaction potential being the sum of all the individual Coulomb potentials between the incoming electron and the target electrons and nucleus [Ehrhardt 1986]. The resultant excitation of the molecule causes an electronic transition according to the Frank-Condon principle which may result in ionisation of the molecule depending on the potential energy curves of the initial and final electronic states [Massey 1969].

When the atomic system is replaced by a molecular system extra effects may cause changes in the theoretical models. In the electron diffraction results from oriented molecules discussion has been given to the possible effect of the modification of the molecular charge distribution caused by bond formation, the effect of the potential from the molecular dipole moment and the effect of polarisation of the molecule to account for the deviations of the theoretical and experimental results [Meier 1994].

Until more experimental data is obtained for oriented molecule electron impact ionisation a more specific formalism of the entrance channel mechanism can not be made.

2.4 Spatially Oriented Molecules

The inhomogeneous hexapole electrostatic field technique requires a strong electric field to selectively transmit rotational states in the higher Stark state. The quantum state selected molecules then pass adiabatically into a weak homogeneous electric field where they are spatially oriented.

2.4.1 Rotation (Classical)

The classical rotational energy of a rigid rotor is [Atkins 1995]

$$T = \frac{I_a \omega_a^2}{2} + \frac{I_b \omega_b^2}{2} + \frac{I_c \omega_c^2}{2}$$

or in terms of angular momentum

$$T = \frac{P_a^2}{2I_a} + \frac{P_b^2}{2I_b} + \frac{P_c^2}{2I_c}$$

where the subscripts abc refer to the figure axis co-ordinate system of the molecule. Since the hexapole technique selects molecules in the higher Stark state the molecule must have a permanent electric dipole moment that does not average to zero over

rotation to the first approximation. Hence the hexapole technique is mostly used to select symmetric top molecules (e.g. CH_3I , CCl_3H). However, the hexapole can also select some asymmetric top molecules, diatomics with electronic angular momentum or linear polyatomics excited in bending vibrations (Section 2.1). For the remainder of this dissertation only symmetric top molecules are considered where two of the moments of inertia are equal.

The moments of inertia are assigned such that $I_c \geq I_b \geq I_a$. If $I_c = I_b > I_a$ then the molecule is a prolate symmetric top molecule such as CH_3I and if $I_c > I_b = I_a$ then the molecule is an oblate symmetric top molecule such as CCl_3H. For the equations that follow an oblate symmetric top molecule is taken as the representative molecule with the symmetry axis denoted as the c-axis (the following is the same for a prolate symmetric top molecule with appropriate changes in the subscripts from abc $\rightarrow$ bca). The classical rotational energy then becomes

$$T = \frac{I_b}{2}(\omega_a^2 + \omega_b^2) + \frac{I_c\omega_c^2}{2} .$$

When an external field is applied the field defines the z-axis of the space fixed co-ordinate system. The orientation of the molecule fixed axis with reference to the space fixed axis can be best specified by the three Euler angles $\theta\phi\chi$ (Figure 2.4.1). The rotational energy in terms of Euler's angles becomes [Goldstein 1981]

$$T = \frac{I_b}{2}\left(\dot{\theta}^2 + \dot{\phi}^2\sin^2\theta\right) + \frac{I_c}{2}\left(\dot{\chi} + \dot{\phi}\cos\theta\right)^2$$

The potential energy of a symmetric top molecule in an electric field is [Goldstein 1981]

$$W = \mu \cdot \varepsilon = -\mu\varepsilon\cos\theta$$

where μ is the electric dipole moment vector, ε the electric field vector and θ the angle between the electric dipole moment vector and the electric field vector. The negative sign occurs due to the relative assignment of the direction of the electric field and the electric dipole moment vectors[1]. The potential energy decreases when the negative end of the dipole is directed towards the positive field.

Since energy and momentum are conserved, the total energy E in an external electric field is constant with time and is given by

$$E = T + W = \frac{I_b}{2}\left(\dot{\theta}^2 + \dot{\phi}^2\sin^2\theta\right) + \frac{I_c}{2}\left(\dot{\chi} + \dot{\phi}\cos\theta\right)^2 - \mu\varepsilon\cos\theta$$

with the Lagrangian becoming

[1] The electric field vector points from the positive field towards the negative field whereas the electric dipole vector points from the negative end of the dipole to the positive end of the dipole.

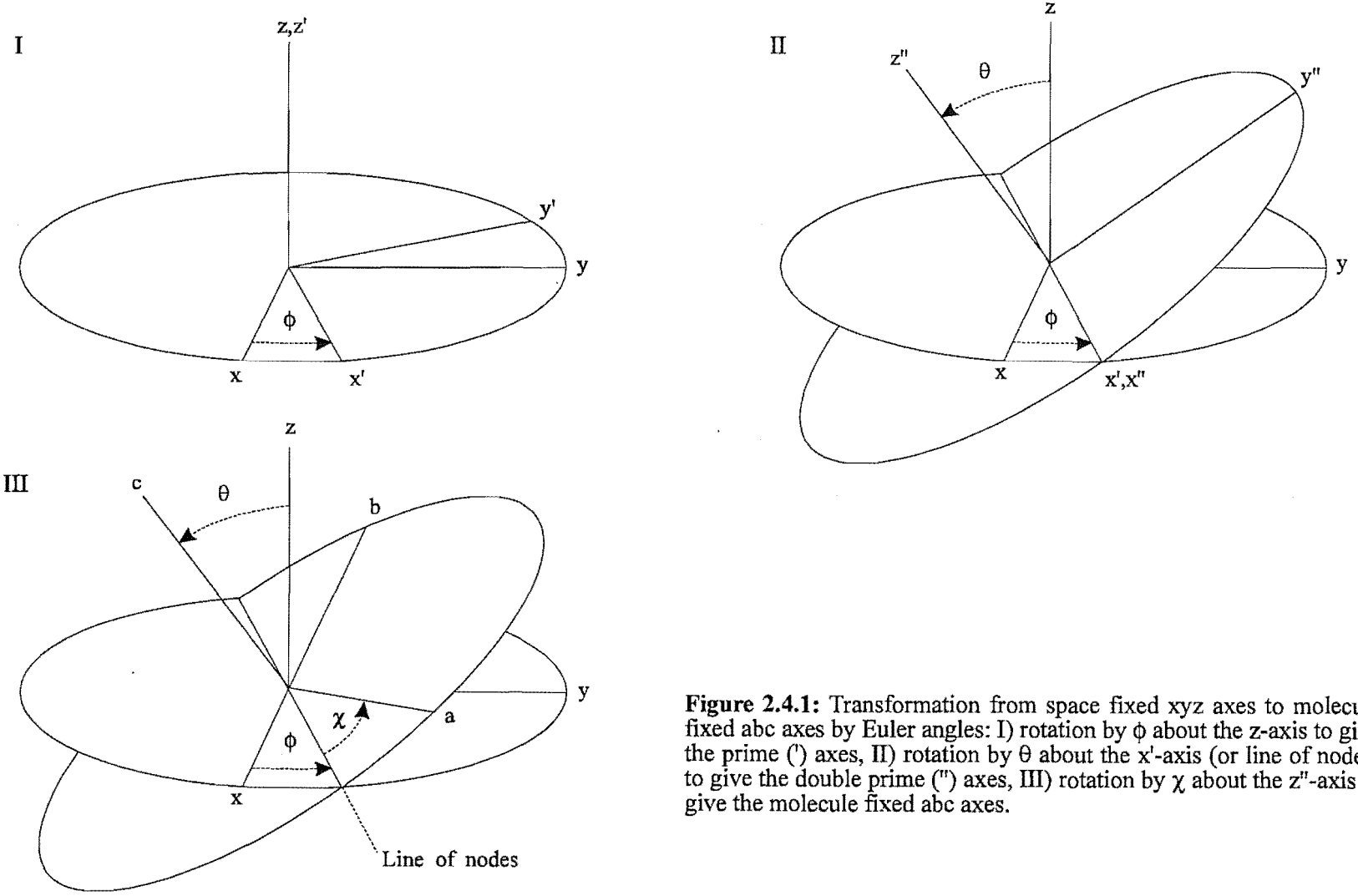

Figure 2.4.1: Transformation from space fixed xyz axes to molecule fixed abc axes by Euler angles: I) rotation by ϕ about the z-axis to give the prime (') axes, II) rotation by θ about the x'-axis (or line of nodes) to give the double prime (") axes, III) rotation by χ about the z"-axis to give the molecule fixed abc axes.

$$L = T - W = \frac{I_b}{2}\left(\dot{\theta}^2 + \dot{\phi}^2 \sin^2\theta\right) + \frac{I_c}{2}\left(\dot{\chi} + \dot{\phi}\cos\theta\right)^2 + \mu\varepsilon\cos\theta.$$

Solving the Lagrangian gives several classical qualitative results (see Appendix A) shown in Figure 2.4.2.

- the component of angular momentum along the field direction is constant, P_z,
- the component of angular momentum along the molecule fixed symmetry axis is constant, P_c,
- P_c precesses around the total angular momentum P with a frequency of $\frac{P}{2\pi I_b}$ causing θ to vary between θ_{min} and θ_{max},
- the torque exerted by the field on the dipole causes μ (or P_c) and P to precess about the field direction.

2.4.2 Rotation (Quantum Mechanical)

The quantum mechanical solution for the motion of a symmetric top molecule in an external electric field begins with the Hamiltonian for the system. This is used to set up the Schrödinger wave equation which, in turn, is used to solve the wave function for the system.

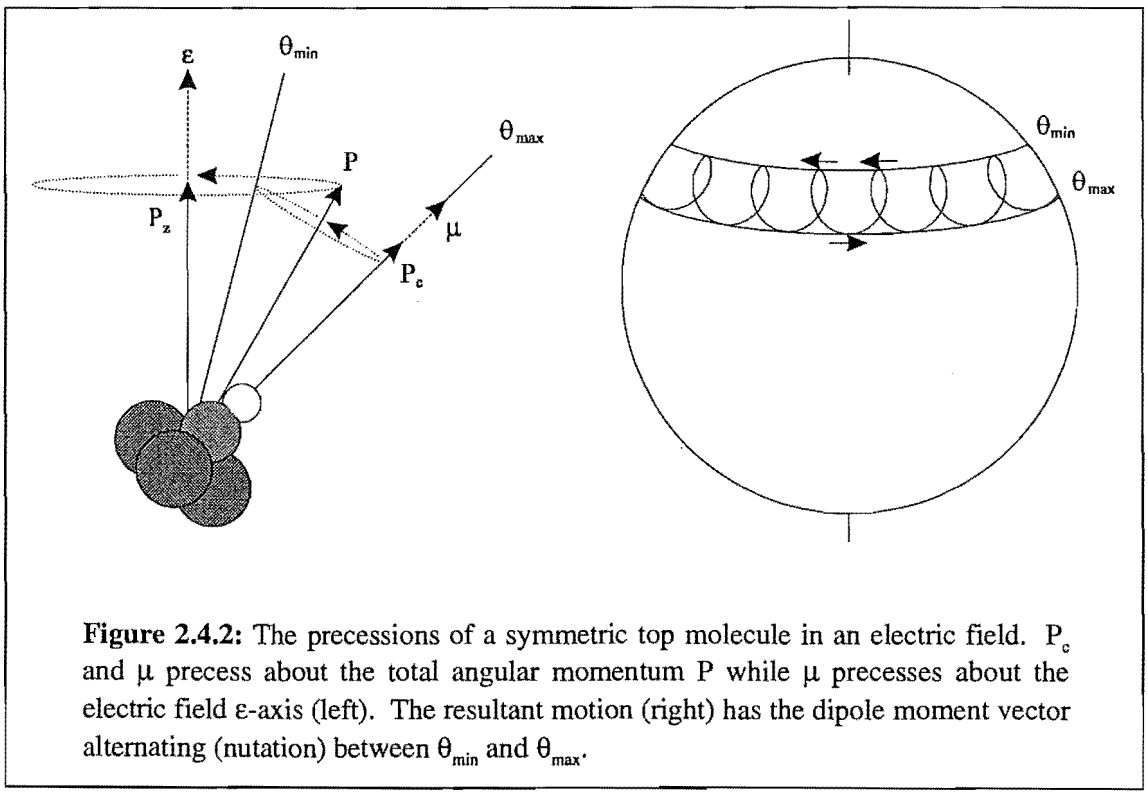

Figure 2.4.2: The precessions of a symmetric top molecule in an electric field. P_c and μ precess about the total angular momentum P while μ precesses about the electric field ε-axis (left). The resultant motion (right) has the dipole moment vector alternating (nutation) between θ_{min} and θ_{max}.

The rotational Hamiltonian for an oblate symmetric top molecule in terms of angular momentum operators (using the correspondence principle from the classical result) is

$$\hat{H}^o = \frac{1}{2I_b}\left(\hat{P}_a^2 + \hat{P}_b^2\right) + \frac{1}{2I_c}\hat{P}_c^2$$

or, in terms of Euler's angles, the Hamiltonian reduces to [Townes 1955]

$$\hat{H}^o = -\frac{h^2}{8\pi^2 I_b}\left[\frac{1}{\sin\theta}\frac{\partial}{\partial\theta}\left(\sin\theta\frac{\partial}{\partial\theta}\right) + \frac{1}{\sin^2\theta}\frac{\partial^2}{\partial\phi^2} + \left(\frac{\cos^2\theta}{\sin^2\theta} + \frac{I_b}{I_c}\right)\frac{\partial^2}{\partial\chi^2} - \frac{2\cos\theta}{\sin^2\theta}\frac{\partial^2}{\partial\phi\partial\chi}\right].$$

The rotational Hamiltonian for an oblate symmetric top molecule in an external electric field in terms of Euler's angles is then

$$\hat{H} = \hat{H}^o - \mu\varepsilon\cos\theta.$$

The Schrödinger equation $\hat{H}\Psi = W\Psi$ can be solved by separation of variables [Townes 1955] with the solutions of the form

$$\Psi = \Theta(\theta)\exp(iM\phi)\exp(iK\chi)$$

where M and K are integers $(0, \pm1, \pm2, \ldots)$ such that the wave function remains single valued.

The function $\Theta(\theta)$ [Shirley 1963], using the dimensionless parameters $\lambda = \mu\varepsilon\left(\frac{8\pi^2 I_b}{h^2}\right)$ and $\xi = W\left(\frac{8\pi^2 I_b}{h^2}\right)$, satisfies the equation

$$\frac{1}{\sin\theta}\frac{\partial}{\partial\theta}\left(\sin\theta\frac{\partial\Theta}{\partial\theta}\right) - \left[\frac{M^2}{\sin^2\theta} + \left(\frac{\cos^2\theta}{\sin^2\theta} + \frac{I_b}{I_c}\right)K^2 - \frac{2\cos\theta}{\sin^2\theta}KM + \lambda\cos\theta - \xi\right]\Theta = 0.$$

For the zero field case $\lambda = 0$ and the differential equation for Θ may be solved using the hypergeometric series which gives the eigenvalues to be [Shirley 1963]

$$\xi_o = J(J+1) + \left[\left(\frac{I_b}{I_c}\right) - 1\right]K^2$$

where J is the total angular momentum quantum number, M the projection of J onto the space fixed z-axis (electric field axis) and K the projection of J onto the molecule fixed c-axis (electric dipole axis). Note that when there is zero electric field the $\pm K$ quantum states are degenerate and there are no M quantum states as there is no electric field to define the z-axis.

When there is an external electric field present ($\lambda \neq 0$) the Schrödinger equation must be solved by other means. Using the zero field case wavefunctions as a basis set,

the Hamiltonian including the field may be represented by an infinite matrix with elements in Dirac notation [Shirley 1963]

$$\langle J'K'M'/\hat{H}/JKM\rangle = \left(\frac{h^2}{8\pi^2 I_b}\right)\xi_o\delta_{JJ'}\delta_{KK'}\delta_{MM'} - \mu\varepsilon\langle J'K'M'/\cos\theta/JKM\rangle \quad .$$

As shown by Shirley [Shirley 1963] the eigenvalues of this matrix give the Stark energies for the molecule. However, the iterative technique used for $\lambda > 1$ tend to converge slowly and are time consuming.

If the field is weak such that the Stark energy term is a small correction to the zero field energy ($\lambda << 1$) then the Stark energy may be found from perturbation theory [Townes 1955]. The first order Stark energy is found by averaging the perturbation over the appropriate unperturbed wavefunctions

$$W_1 = -\varepsilon\int\Psi^*(\mu\cos\theta)\Psi d\tau$$

$$= -\mu\varepsilon\langle JKM/\cos\theta/JKM\rangle$$

where the matrix element is evaluated by Townes [Townes 1955] as

$$W_1 = -\mu\varepsilon\frac{MK}{J(J+1)} = -\mu\varepsilon\langle\cos\theta\rangle$$

where $\langle\cos\theta\rangle$ is the average value of $\cos\theta$ over a precession period.

The Stark energy removes the degeneracy of the M and ±K quantum states. The trajectory of the symmetric top molecule is dependent on the sign of MK with $MK > 0$ causing molecules to travel towards higher electric field strength and those molecules with $MK < 0$ to travel towards lower electric field strengths.

The second order Stark energy can also be calculated by perturbation theory. The second order term tends to be much smaller than the first order Stark energy term except in certain situations such as linear molecules, symmetric top molecules with K=0 and NH_3, where it is rapidly inverting.

The probability of finding a molecule with rotational state Ψ_{JKM} (/JKM⟩) with a specific orientation to the z-axis is [Choi 1986]

$$P_{JKM}(\rho)d\rho = 4\pi^2(\Psi^*_{JKM}\Psi_{JKM})\sin\theta d\theta$$

$$= \frac{(2J+1)}{2}(D^{J*}_{KM}D^{J}_{KM})d\rho$$

where D^J_{KM} is the rotation function matrix element (angular momentum eigenfunction) and the orientation probability function $P_{JKM}(\rho)$ is a function only of θ ($\rho = \cos\theta$).

The probability density function is dependent on $\cos\theta$ terms and is symmetrical about the electric field vector hence it can be expressed conveniently in terms of Legendre polynomials $P_n(\cos\theta)$ by

$$P_{JKM}(\rho) = \frac{(2J+1)}{2} \sum_{n=0}^{2J} C_n(JKM) P_n(\rho) \qquad (2.4.1)$$

where the expansion coefficients C_n are determined as a function of (JKM) values [Choi 1986, Zare 1988]. For example, using the values of $C_n(JKM)$'s the orientation distribution functions for the /111⟩ and /212⟩ states can be expressed as

$$P_{111}(\rho) = \frac{1}{2}P_0(\rho) + \frac{3}{4}P_1(\rho) + \frac{1}{4}P_2(\rho)$$

$$P_{212}(\rho) = \frac{1}{2}P_0(\rho) + \frac{1}{2}P_1(\rho) - \frac{5}{14}P_2(\rho) - \frac{1}{2}P_3(\rho) - \frac{1}{7}P_4(\rho)$$

which are shown with the classical probability distribution functions [Choi 1986] in Figure 2.4.3. The quantum mechanical calculation gives a finite probability of finding the symmetric top molecule with an orientation which is classically forbidden.

2.4.3 Hexapole Electric Field

For a 2n-pole hyperbolic electrostatic field the potential is given in cylindrical co-ordinates as

$$U(r,\phi) = U_o\left(\frac{r}{r_o}\right)^n \cos(n\phi)$$

where r_o and ϕ are shown in Figure 2.4.4. For a hexapole field, where 2n=6, the potential becomes

$$U(r,\phi) = U_o\left(\frac{r}{r_o}\right)^3 \cos(3\phi).$$

The electric field vector is given by the negative gradient of the potential

$$\mathbf{E} = -\nabla U(r,\phi)$$

where $\nabla = \frac{\partial}{\partial r}\hat{e}_r + \frac{\partial}{\partial \phi}\hat{e}_\phi + \frac{\partial}{\partial z}\hat{e}_z$ in cylindrical co-ordinates and hence

$$\mathbf{E} = 3U_o\left(\frac{r^2}{r_o^3}\right)\cos(3\phi)\hat{e}_r - 3U_o\left(\frac{r^2}{r_o^3}\right)\sin(3\phi)\hat{e}_\phi$$

and hence the electric field strength is

$$\varepsilon = (\mathbf{E}\cdot\mathbf{E})^{\frac{1}{2}} = 3U_o\frac{r^2}{r_o^3}.$$

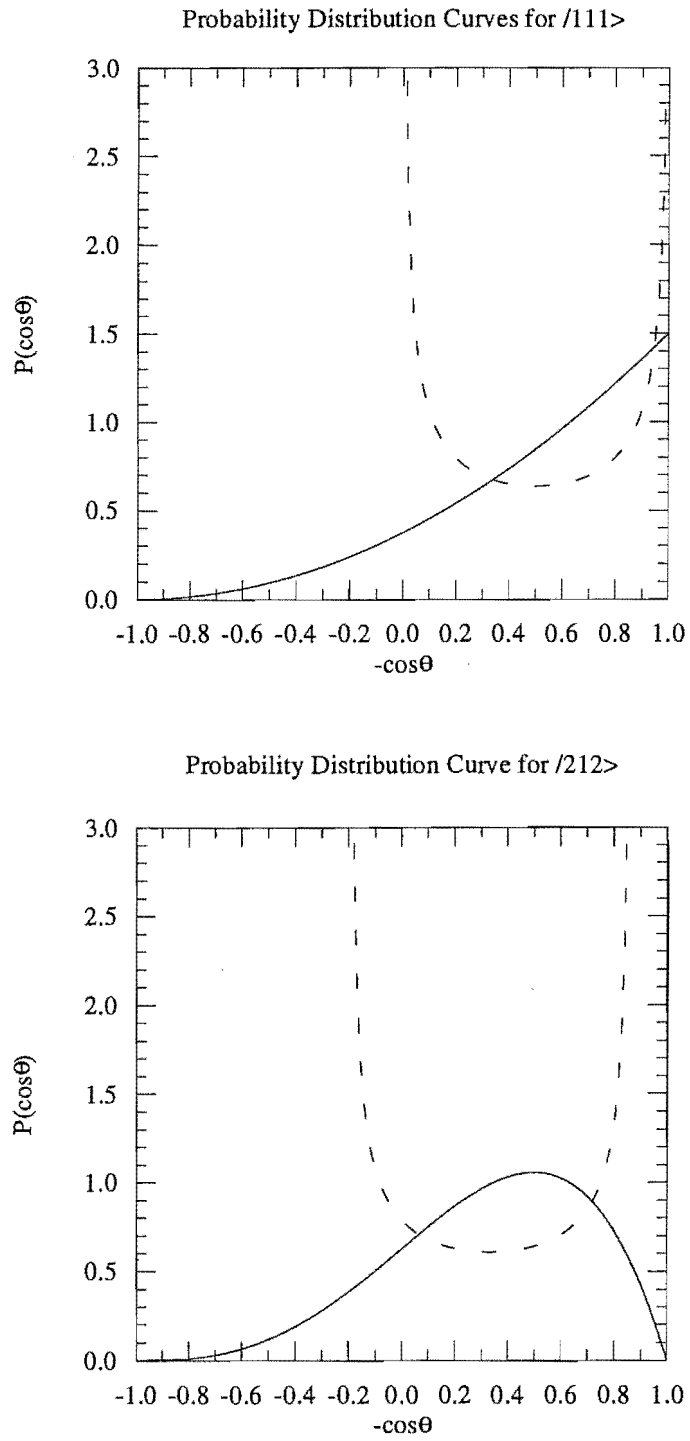

Figure 2.4.3: Classsical (dashed line) and quantum mechanical (full line) probability distribution functions for finding a molecule with an orientation of cosθ between the space fixed axis and molecule fixed axis for the quantum /JKM> states /111> and /212>.

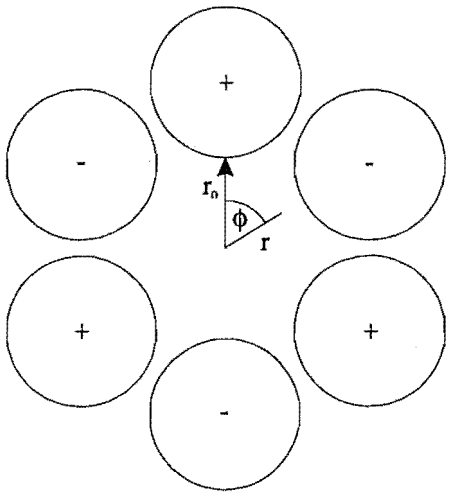

Figure 2.4.4: Schematic of a hexapole rod configuration using cylindrical rods showing the inscribed radius r_o. For complete description of the potential between the rods both the radial distance r and angle ϕ must be given.

The Stark energy of a symmetric top molecule in an electric field is given by [Townes 1955]

$$W_1 = -\mu\varepsilon\cos\theta = -\mu\varepsilon\frac{MK}{J(J+1)} = -\mu_{eff}\varepsilon$$

where $\mu_{eff} = \mu\cos\theta$. The radial force on a charged particle is given by $F_r = -\frac{\partial W_1}{\partial r}$ where W_1 is the potential energy of the system. Hence

$$F_r = -\frac{\partial W_1}{\partial \varepsilon}\frac{\partial \varepsilon}{\partial r}$$

$$= \mu_{eff} 6U_o \frac{r}{r_o^3}$$

$$= \frac{6U_o\mu_{eff}}{r_o^3} r.$$

In cylindrical co-ordinates the radial force is given by $F_r = m\ddot{r} - mr\dot{\phi}^2$. When the molecule enters the hexapole field the angular rotation about the centre of the hexapole axis is zero, such that $\dot{\phi} = 0$, and $F_r = m\ddot{r}$. This gives the equality

$$F_r = \frac{6U_o\mu_{eff}}{r_o^3} r = m\ddot{r}$$

or

$$\ddot{r} = \frac{6U_0\mu}{mr_0^3}\frac{MK}{J(J+1)}r = \omega^2 r.$$

If $MK > 0$ then the solutions for r are $r(t) = A\exp(\omega t) + B\exp(-\omega t)$. This solution would give a trajectory which is divergent from the beam axis and so would be lost to any detection device on axis. If $MK < 0$ then the solution for r is of the form $r(t) = A\cos(\omega t) + B\sin(\omega t)$. This solution would give a sinusoidal trajectory which would focus the molecule back to the hexapole axis as shown in Figure 2.4.5.

2.4.4 Transmission through a Hexapole Electrostatic Field

From the equation of motion, the constants A and B are determined by the initial conditions for the system. Let time $t = 0$ be the time that the molecule enters the hexapole electric field. The radial off axis distance that the molecule will experience, assuming that the nozzle can be taken as a point source due to its small aperture relative to the aperture of the hexapole, is $r(t) = A = l_1\tan\alpha$ (Figure 2.4.6). The radial velocity will be $\dot{r}(t) = B\omega = v\sin\alpha$ (Figure 2.4.6). Hence the two constants of motion become

$$A = l_1\tan\alpha = l_1\alpha$$

$$B = \frac{v}{\omega}\sin\alpha = \frac{v\alpha}{\omega}$$

where, for small α, $\sin\alpha \approx \tan\alpha \approx \alpha$. Hence, the equation of motion through a hexapole electric field by a symmetric top molecule is given by

$$r(t) = l_1\alpha\cos(\omega t) + \frac{v\alpha}{\omega}\sin(\omega t).$$

For transmission through the hexapole electric field several physical conditions must be met;

- the molecule must be able to enter the hexapole electric field,
- the molecule can not hit the hexapole rods,
- the molecule must be able to exit the hexapole.

2.4.4.1 Transmission - entry into the hexapole field.

To enter the hexapole electric field the angle that the molecule can make to the axis must fall between that made to the entry aperture, α_A, and that made to the beam stop, α_{BS} (Figure 2.4.7). Hence it is required that

$$\alpha_{BS} < \alpha_{IN} < \alpha_A.$$

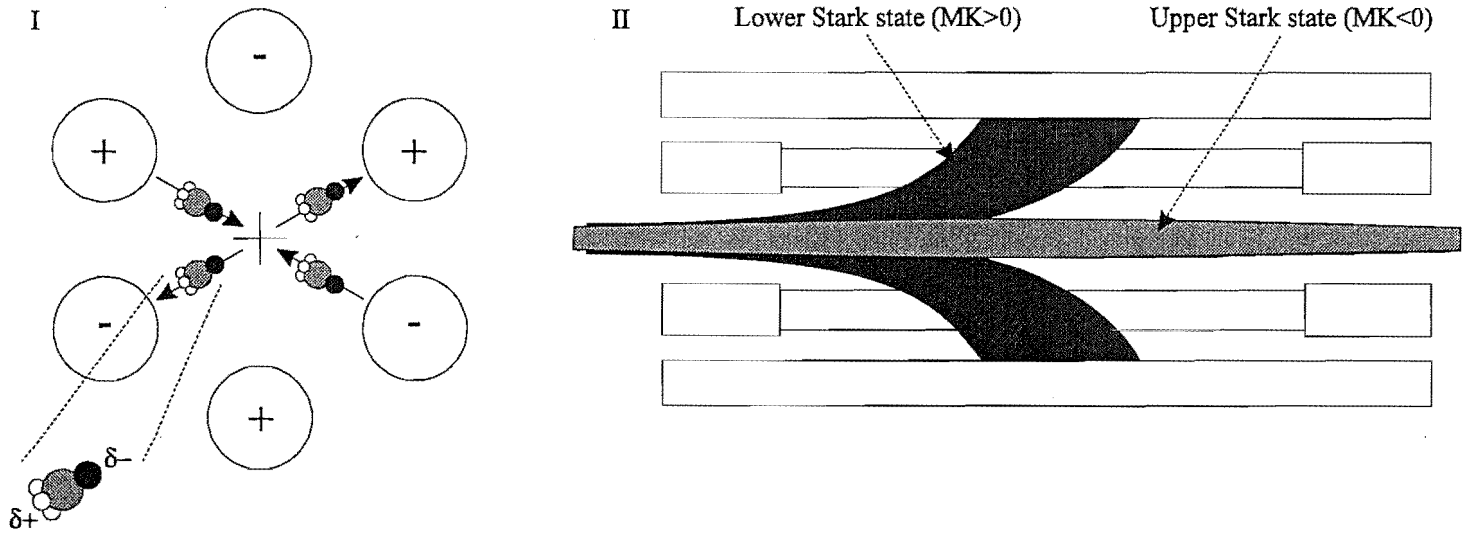

Figure 2.4.5: I) Depending on the direction of the electric dipole the molecule will either be pushed towards the axis (upper Stark state) or pulled away from the axis (lower Stark state), II) the effect of the electric dipole direction on transmission through the hexapole field. Lower Stark state is attracted towards the rods, upper Stark state is focused to the axis.

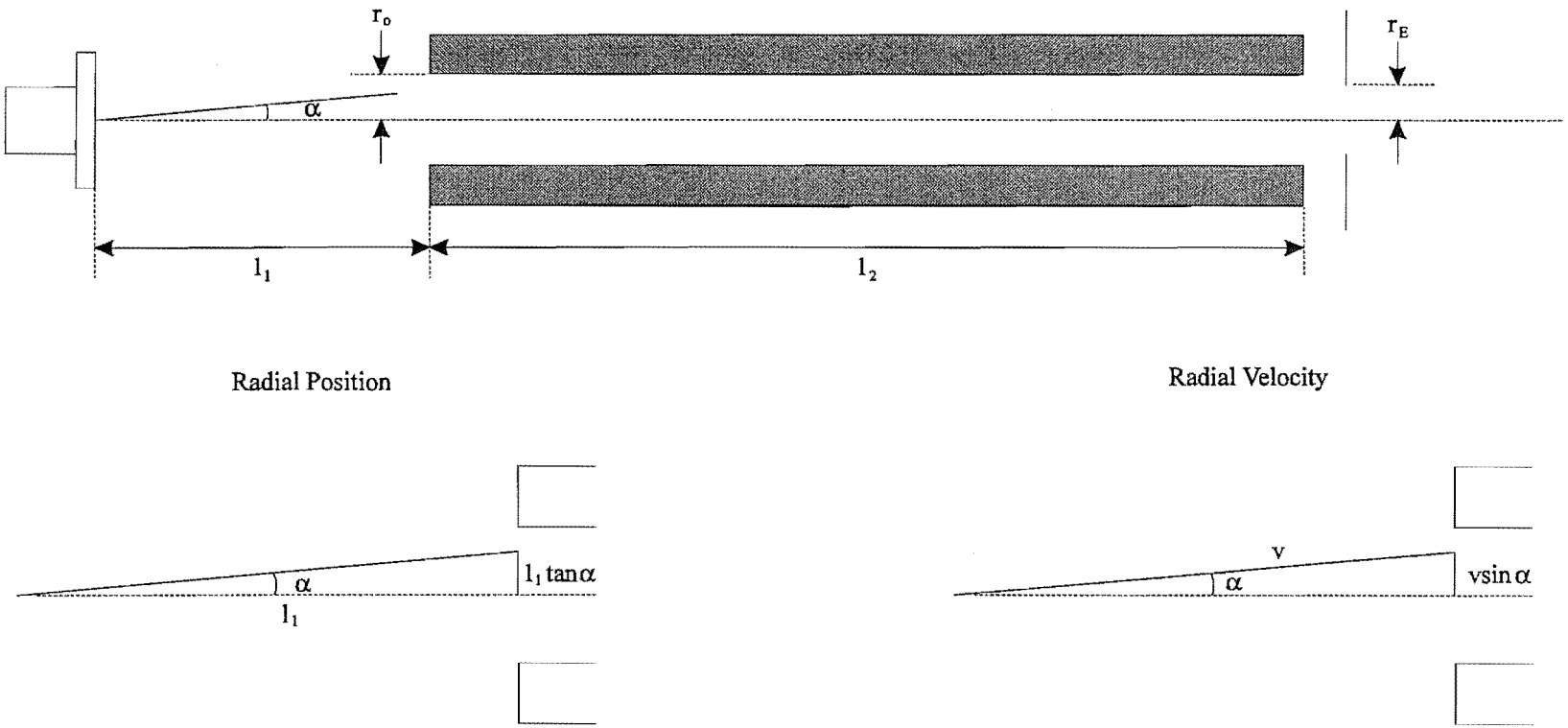

Figure 2.4.6: Distance and aperture size assignments for a generalised hexapole configuration showing the radial position and velocity when the molecule enters the hexapole electric field.

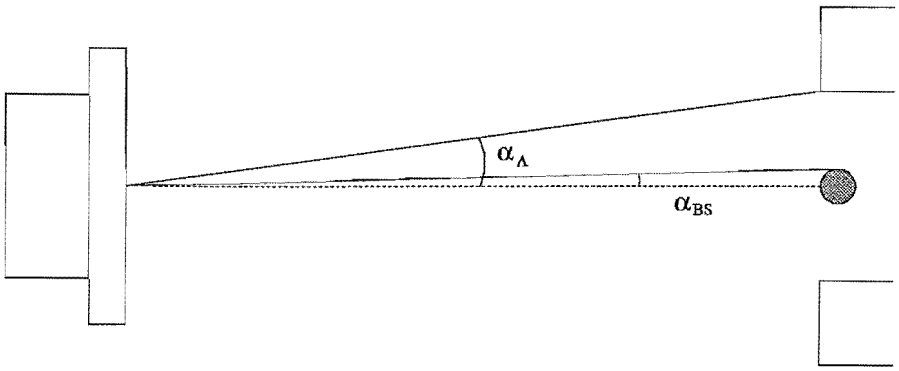

Figure 2.4.7: Angular requirement for a molecule to enter the hexapole field: $\alpha_{BS}<\alpha_{IN}<\alpha_A$.

2.4.4.2 Transmission - through hexapole rods.

The maximum off-axis radial distance experienced by the molecule occurs at a time, t_m, when $\dot{r}(t_m)=0$. This radial distance, r_m, can not exceed the radius of the hexapole field, r_o. The time that the maximum radial distance occurs is

$$\dot{r}(t_m) = -\omega l_1 \alpha \sin(\omega t_m) + v\alpha \cos(\omega t_m) = 0$$

$$\frac{v\alpha}{\omega l_1 \alpha} = \frac{\sin(\omega t_m)}{\cos(\omega t_m)} = \tan(\omega t_m)$$

$$\omega t_m = \tan^{-1}\left(\frac{v}{\omega l_1}\right)$$

Hence the maximum radial distance that the molecule reaches on the passage through the hexapole electric field is then

$$r_m = l_1 \alpha \cos(\omega t_m) + \frac{v\alpha}{\omega}\sin(\omega t_m)$$

$$= l_1 \alpha \left(\frac{\omega l_1}{\sqrt{v^2+\omega^2 l_1^2}}\right) + \frac{v\alpha}{\omega}\left(\frac{v}{\sqrt{v^2+\omega^2 l_1^2}}\right)$$

$$= \frac{\alpha v^2 + \alpha\omega^2 l_1^2}{\omega\sqrt{v^2+\omega^2 l_1^2}}$$

$$= \frac{v\alpha}{\omega}\sqrt{1+\frac{\omega^2 l_1^2}{v^2}}$$

$$= \frac{v\alpha}{\omega}\sqrt{1+\beta_1^2}$$

where $\beta_1 = \frac{\omega l_1}{v}$. Since $r_m < r_o$ then

$$r_o > \frac{v\alpha}{\omega}\sqrt{1+\beta_1^2}$$

or, the maximum angle of incidence allowable for successful transmission through the hexapole rods,

$$\alpha_F^2 < \frac{r_o^2\omega^2}{v^2(1+\beta_1^2)}.$$

2.4.4.3 Transmission - exit from hexapole.

The molecule will exit the hexapole electric field at a time, t_e, where $t_e = \frac{l_2}{v}$. Hence the exit aperture radius, r_E, must be greater than the off axis radial distance at t_e

$$r(t_e) = l_1\alpha\cos\left(\frac{\omega l_2}{v}\right) + \frac{v\alpha}{\omega}\sin\left(\frac{\omega l_2}{v}\right) < r_E$$

$$\cos(\beta_2) + \frac{1}{\beta_1}\sin(\beta_2) < \frac{r_E}{l_1\alpha}$$

where $\beta_2 = \frac{\omega l_2}{v}$. Hence the angle of incidence for successful exiting becomes

$$\alpha_E^2 < \frac{\omega^2 r_E^2}{v^2[\beta_1\cos\beta_2 + \sin\beta_2]^2}.$$

The maximum angle of incidence for transmission is the lesser of α_E^2, α_F^2 or α_A^2. The minimum angle of incidence is determined by the beam stop α_{BS}^2.

2.4.5 Probability Functions

Once each maximum and minimum angle of incidence (α_{max} and α_{min}) has been calculated for each velocity v and each quantum state /JKM⟩, it is then possible to calculate the fraction of molecules that will exit the hexapole, relative to the direct beam signal that impinges into the hexapole when there is no hexapole voltage and no beam stop. Assuming that the angular distribution of beam intensity is uniform near the beam axis, as the range of the angle of incidence is small, and taking $\alpha_{BS} = 0$ hence $\alpha_{min} = 0$, then the fraction of molecules transmitted at a specific hexapole voltage, velocity and orientation is

$$A(U_o, v, \rho) = \frac{\alpha_{max}^2}{\alpha_A^2}$$

Integrating $A(U_o, v, \rho)$ over the beam velocity distribution, given by Equation 2.2.2, gives the transmitted intensity for a specific quantum state /JKM⟩ at a set hexapole voltage U_o

$$F_{JKM}(U_o) = \int_0^\infty A(U_o, v, \rho) f_s(v) dv.$$

The total transmitted intensity for a set hexapole voltage U_o can then be determined by the summation of $F_{JKM}(U_o)$, multiplied by the partition function for the specific quantum state, over all quantum states within the beam

$$T(U_o) = \sum_{JKM} F_{JKM}(U_o) f_{JK}$$

where [Townes 1955]

$$f_{JK} = \frac{S(I,K)(2J+1)\exp(-W/kT_{rot})}{\sum_{J=0}^{\infty}\sum_{K=0}^{J} S(I,K)(2J+1)\exp(-W/kT_{rot})}$$

with T_{rot} the rotational temperature of the beam, W the rotational energy at zero electric field, I the nuclear spin of the symmetric top molecule and S(I,K) is the degeneracy of nuclear spin given by [Townes 1955]

$S(I,K) = 2(4I^2+4I+3)$ for K equal to a multiple of 3 but not equal to 0,

$= (4I^2+4I+3)$ for K equal to 0 and

$= 2(4I^2+4I)$ for K not a multiple of 3.

The transmitted orientation distribution function for a set hexapole voltage U_o is similar to the total transmitted intensity at voltage U_o, with additional summation over the orientation probability density function $P_{JKM}(\rho)$ of Equation 2.4.1

$$P(\rho, U_o) = \sum_{JKM} P_{JKM}(\rho) F_{JKM}(U_o) f_{JK}. \qquad (2.4.2)$$

This is the theoretical orientation distribution that passes into the homogeneous orienting field.

2.4.6 Orienting Field

Molecules that have been transmitted by the hexapole field are in their upper Stark state. They exit the hexapole and enter a weak homogeneous electric field (typically 10-20 Vcm^{-1}) which provides the reference space fixed z-axis around which the molecules precess. This homogeneous field is referred to as the orienting field.

The transition from the strong electric field of the hexapole to the weak homogeneous electric field of the parallel plates must be an adiabatic transfer to retain

the state selection and hence, the orientation. Maltz *et al* [Maltz 1972] discussed the concept of reprojection of angular momentum for an electric dipole in a varying electric field, which is similar to Majorana flops experienced in magnetic fields [Ramsey 1956]. The adiabatic criterion [Maltz 1972] for reorientation of the angular momentum requires that $\omega_E << \omega_{\Delta M}$ where ω_E is the angular frequency of rotation of the electric field and $\omega_{\Delta M}$ the angular frequency of the transition between M-levels [Maltz 1972].

The brute force method of orientation (Section 2.1) also requires adiabatic transitions from the field free region to the strong field region of the scattering volume. Loesch and Remscheid [Loesch 1990] justified an adiabatic transition by stating that the time for a rotation about the field is orders of magnitude less than the time to travel through the strong field. Hence, the molecules experience no sudden field effects but only a gradual changing field.

Within the strong field regime of the hexapole the nuclear spin I is decoupled from the rotational angular momentum J and so states of /JKM⟩ are focused. In the weak field of the orienting field however, the nuclear spin can re-couple with the rotational angular momentum to give a total angular momentum F=J+I, J+I-1,...,$|J-I|$ and so one parent state /JKM⟩ can become an ensemble of states whose average orientation is reduced [Parker 1989]. Limited experimental determination of the degree of re-orientation is available. Gandhi and Bernstein [Gandhi 1988], using polarised photofragmentation time-of-flight, determined that re-coupling occurs rapidly for CH_3I but did not determine how this affected the degree of orientation. Until accurate orientation distributions are able to be determined the degree of smearing of the molecular orientation will remain unknown. In a reactive oriented molecule experiment the comparison is between one end and the other, hence any re-coupling could reduce the experimental determined steric factor but, as long as the re-coupling does not randomise the orientations, the steric effect will still be present.

The orientation distribution within the scattering volume is assumed to be identical to the theoretical transmitted orientation distribution of Equation 2.4.2. Trajectory simulations written by Prof. P.R.Brooks at Rice University, Houston, Texas, were performed with our experimental conditions (Section 3.3) and the transmitted orientation distribution of Equation 2.4.2 for CH_3Cl is shown in Figure 2.4.8. The theoretical transmitted orientation distribution has no specific rotational state selection (i.e. no selective preference to a particular orientation) because of the experimental choice of aperture diameters to obtain maximum beam intensity. The distribution shows that the average $\cos\theta$ orientation has $\langle\cos\theta\rangle = 0.15$ with there being a finite probability of molecules having orientations with $\cos\theta < 0$ within the scattering volume.

2.5 Beam Detection

There are many different techniques available for the detection of molecules, whether they be in a directed beam or random background. One of the most specific

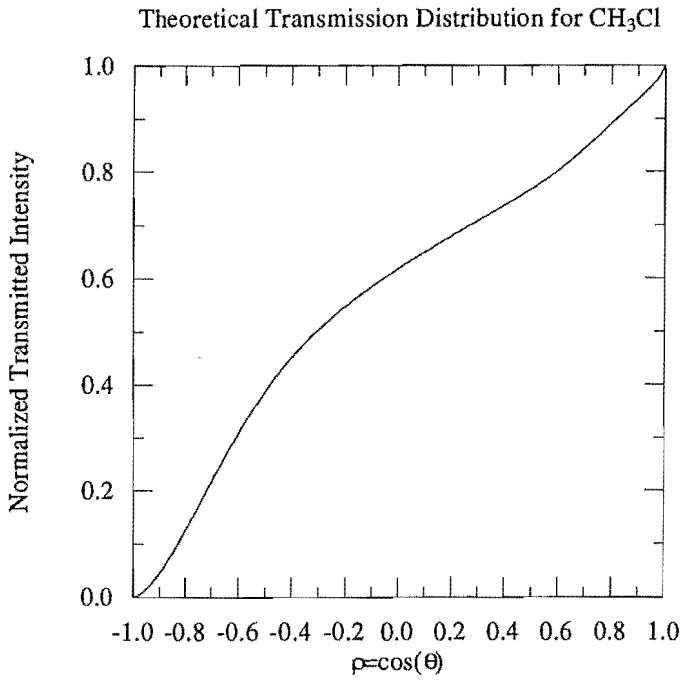

Figure 2.4.8: Theoretical transmission distribution function for CH_3Cl at 5.5 kV using the experimental configuration of Section 3.3.

methods is the use of a quadrupole mass filter. The quadrupole filter has been used in this research and the general principles of the filter will be described here.

2.5.1 Quadrupole Filter

Ions that enter the quadrupole mass filter are selected solely on their mass to charge (m/z) ratio with no preference to the ion polarity. The quadrupole mass filter rod assembly is shown in Figure 2.5.1. Ideally it has four parallel hyperbolic rods to which a direct current (DC) potential and a radio frequency (RF) potential are applied simultaneously. Ions enter the field along the z-axis, parallel to the direction of the rods, and experience an electric field given by [March 1989]

$$P(x,y,z) = \frac{[U + V\cos(2\pi ft)](x^2 - y^2)}{r_o^2}$$

where f is the frequency of the RF potential, r_o is given on Figure 2.5.1, V is the peak to zero amplitude of the RF potential and U the DC potential. The rods lying on the x-axis experience a potential of $[U + V\cos(2\pi ft)]$ and the rods on the y-axis experience a potential of $-[U + V\cos(2\pi ft)]$. The RF potential applied to each pair of rods is out of phase by 180°, with the amplitudes being swept in a saw tooth manner which constitutes a mass scan.

The motion of the ions as they enter the potential field are complex trajectories described by Mathieu's equations [March 1989]. Solutions to the Mathieu's equations

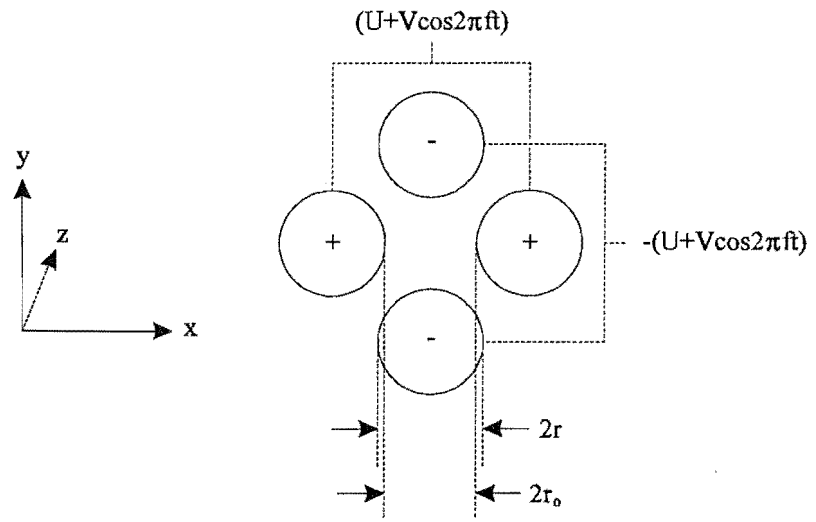

Figure 2.5.1: Quadrupole mass filter rod configuration using cylindrical rods. Potentials on each rod are out of phase by 180°. The ratio r/r_o=1.1487 to approximate a hyperbolic field. The z-axis is into the page down the length of the quadrupole rods.

are non-trivial and outside the scope of this dissertation, however, it is sufficient to note that ions will only follow stable trajectories if their maximum displacement from the z-axis is less than the field radius r_o. In the x-z plane (positive potential plane) the ions near the centre are in an electrostatic potential well and will oscillate under the action of the RF field. The oscillation amplitude decreases with ion mass so as the lighter ions are more likely to collide with the quadrupole rods. Simultaneously the ions will sample an attractive DC potential in the y-z plane with the superimposed RF field tending to guide lighter ions towards the axis. The various combinations of DC and RF potentials are represented in stability diagrams where a and q values are plotted as shown in Figure 2.5.2. Only the positive (a,q) quadrant of the stability diagram is shown as there is symmetry around both axes with the bounded regions representing stable trajectories [March 1989].

Also shown in Figure 2.5.2 is the operating line or scan line which has a fixed a/q or U/V ratio. As the values of U and V are varied the masses that fall within the stable trajectory region also vary. The line segment that intersects the stable area represents those masses which will pass through the quadrupole filter for those particular conditions of U, V and f. Increasing the slope of the scan line so that it passes closer to the apex of the stability region increases the resolution but decreases the sensitivity. The mass spectrum is scanned by the simultaneous variation of U and V amplitudes at fixed RF frequency f. The scan line crosses the stability region at two points corresponding to the upper and lower limits of the mass filter band pass Δm. The mass resolution is then given as

$$R = \frac{m}{\Delta m}$$

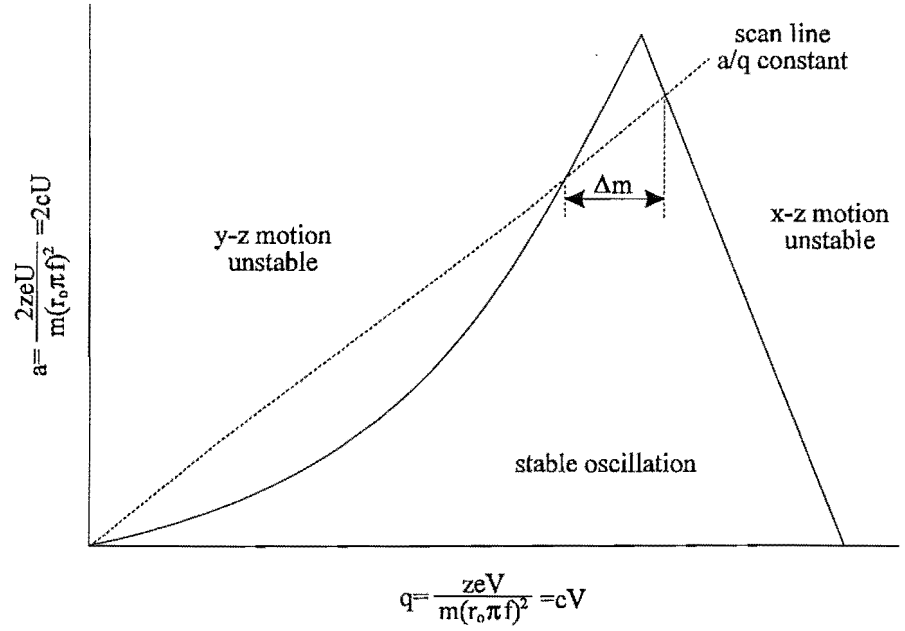

Figure 2.5.2: Stability diagram representing stable and unstable oscillations for different masses as determined by the a,q values. The dashed line represents a scan line with Δm an indicator of the resolution of the quadrupole mass filter.

which is dependent on the slope of the scan line.

For real quadrupole systems the performance and mass resolution may differ significantly from the ideal system due to limitations on both construction of the rods and electrical non-idealities. The machining of hyperbolic rods is a difficult process and so circular rods are used (Figure 2.5.1). To approximate the hyperbolic field the radius of the circular rods, r, is made to the ratio $r/r_0=1.1487$ [March 1989]. The resolution of the quadrupole mass filter will be reduced due to the mechanical tolerance of the radius of the rods, however, through proper mechanical machining and accurate alignment of the rods on their insulating supports this tolerance can be minimised.

Electrical instabilities can occur due to the presence of contamination of the rod surfaces which build up insulating layers or zones which can change the local electric field. Fringe fields at the entrance of the quadrupole have the effect of degrading the transmission of the filter for the higher masses. Ions entering the quadrupole cross a transition region where both the DC and RF fields sweep from zero to the internal value of the quadrupole i.e. the ion moves up the scan line on Figure 2.5.2 from the origin, where both DC and RF fields are zero, to the operating point in the stability region passing through the x-z instability region. One solution to the problem of fringing fields is to have the ions initially pass through a RF only pre-quadrupole, such that the ions experience a region where a=0, and a is only increased once q is already at the operating value. This pre-filter then acts as a wide band ion transmitter which reduces the loss of ions.

2.5.2 Electron Multipliers

The simplest means of detecting an ion beam is the Faraday cup collector. Positive ions are collected by a cylindrical cup partially surrounded by a negatively polarised shield to enhance collection efficiency and to prevent detection of spurious electrons emitted from the ion source. The Faraday cup is cheap, stable with time and unaffected by air exposure, however, it has no gain of the detected ion current, is susceptible to noise (which limits sensitivity) and often has poor response times.

The detector of choice tends to be the electron multiplier which gives a substantial enhancement in both sensitivity and response time. The electron multiplier converts the positive ion current into an electron current which is further amplified by means of the secondary emission effect shown in Figure 2.5.3. The front cone of the multiplier is held at a high negative potential (between -1 kV to -3 kV) to attract the ions. Ions incident on the dynode resistive coating cause the multiplier to emit electrons. These primary electrons flow down the potential gradient of the multiplier tube to the ground potential of the collector, continuously colliding with the walls and emitting further secondary electrons (Figure 2.5.3).

The expected output current i of an electron multiplier is given by [Scoles 1988]

$$i = -e.F.p.G$$

where e is the unit electronic charge of an electron, F the flux of ions impinging on the input stage of the multiplier, p the ion-electron conversion probability and G the multiplier gain. The ion-electron conversion probability largely determines the efficiency of a multiplier by determining the fraction of impinging ions that will stimulate the production of primary electrons on the surface of the multiplier. The gain is typically in the range of 10^6-10^8 which is sufficient to detect single ions in pulse counting mode. The output of electron multipliers is a stream of narrow electron current pulses with a width of about 10^{-8} seconds with varying heights superimposed on any electronic noise that is present. The random pulse noise from an electron multiplier may be as low as 10^{-2} counts per second.

Electron multipliers can be operated in two modes: pulse counting mode or analogue mode. In analogue mode the electron current is converted to a voltage signal by a load resistor which is then amplified and measured. The voltage level is then proportional to the number of ions detected by the multiplier.

When the flux of the ions is sufficiently low (10^6 per second) such that there is little overlap between successive electron current pulses the electron multiplier can be operated in pulse counting mode. The electron current pulses are sent to the input stage of a preamplifier and converted into a voltage pulse. The voltage pulse is then passed to an amplifier to give +5V followed by a voltage comparator or discriminator which removes the thermal noise of the detector from the signal pulses. The pulse intensity can vary due to fluctuations in the multiplier gain but it is always much greater than the thermal noise. The output from the discriminator is then fed to a digital counter that

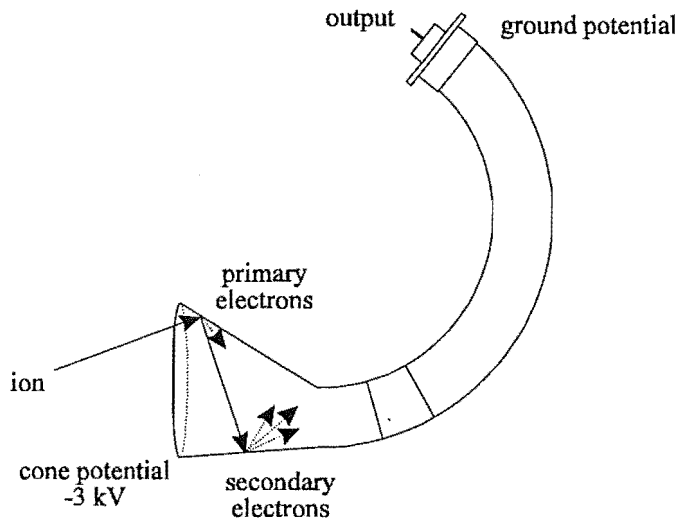

Figure 2.5.3: Ions are attracted to the cone of the electron multiplier by a high negative potential. On impact electrons are emitted from the surface which cause emission of secondary electrons as the electrons flow towards the output at ground potential.

measures the number of counts N in a time interval Δt. The number of counts may fluctuate due to the variation in ion current with the amplitude of the fluctuations given by $\sqrt{N}$ [Scoles 1988]. It should be noted that when the measurement time becomes long consideration must then be given to experimental instabilities affecting the measurement accuracy.

Chapter 3

Molecular Beam Machine Development

The experimental development naturally progressed through three different stages of construction. Initially the machine was developed to measure the appearance potentials of cluster ions formed during the nozzle expansion, and electron impact ionised in a quadrupole mass spectrometer. The experimental configuration and results for this stage are presented in Section 3.1 and Chapter 4 respectively.

The hexapole rod assembly and scattering chamber, required for the later stages, were being constructed within the Department while appearance potentials of clusters were being measured. Following completion of the cluster experiments, the molecular beam machine was extended to incorporate the hexapole rods as discussed in Section 3.2. Preliminary characterisation of the hexapole was completed with some preliminary asymmetry results for electron impact ionisation of spatially oriented molecules also being performed. A mechanical pump failure required the cleaning of the vacuum chambers and prevented the continuation of the asymmetry experiments, at this stage, and resulted in the implementation of stage III of the molecular beam machine.

Stage III, described in Section 3.3, was designed to fulfil the perceived future requirements of ion-oriented molecule research. Stage III provided increased pumping on the nozzle chamber, increased collimation with the inclusion of a buffer chamber and larger volume scattering chamber which, in the future, could contain a rotatable quadrupole mass spectrometer. These features were not specifically required for successful electron impact ionisation asymmetry measurements but did facilitate the use of higher backing pressures and increased ease of modifications and repairs throughout the scattering region.

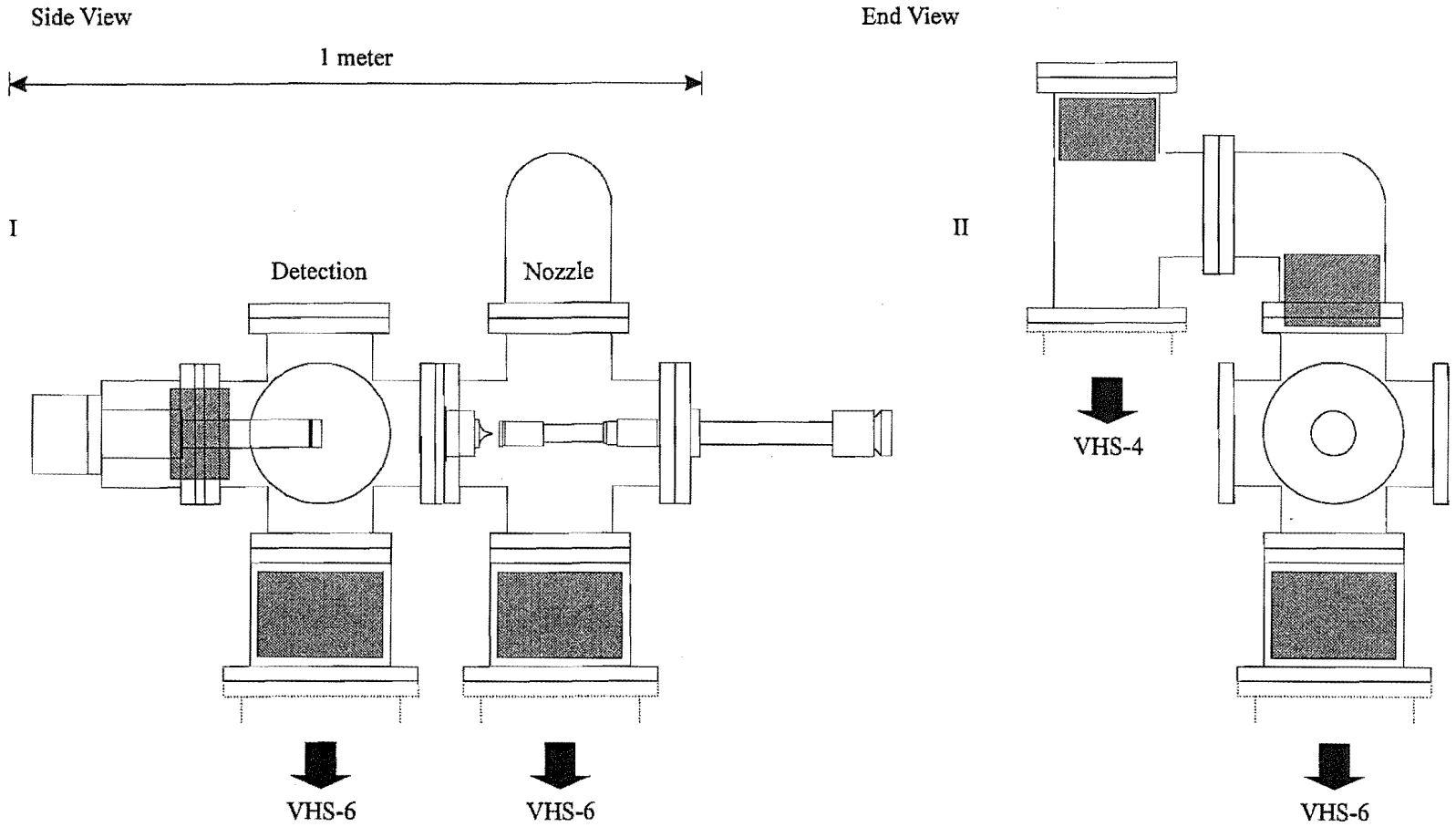

Figure 3.1.1: Vacuum system for determination of appearance potentials of small cluster ions. I) side profile of machine showing the nozzle and detection chambers, II) end profile of nozzle chamber showing the arrangement of the two diffusion pumps. The shaded regions indicate liquid nitrogen traps.

3.1 Stage I - Ionisation of Clusters

3.1.1 Vacuum System

The vacuum system used for the study of appearance potentials of cluster ions is schematically shown in Figure 3.1.1. The machine comprises two differentially pumped vacuum chambers: the nozzle chamber and the detection chamber.

The nozzle chamber was a six inch Varian stainless steel cross (four ports). The chamber was pumped by Varian VHS-6 (3000 ls^{-1}) and Varian VHS-4 (1500 ls^{-1}) diffusion pumps. The Varian VHS-6 diffusion pump was connected to the bottom port of the nozzle chamber and the Varian VHS-4 was connected to the top port of the nozzle chamber via a six inch tubular U-bend arrangement (Figure 3.1.1). The two diffusion pumps were backed by a tandem arrangement of mechanical pumps consisting of Edwards E2M40 (700 $lmin^{-1}$) and EDM20 (342 $lmin^{-1}$) mechanical pumps.

Additional cryogenic pumping of the nozzle chamber was facilitated by three custom built stainless steel liquid nitrogen traps. One trap was situated in the cavity directly above the VHS-4 diffusion pump (Figure 3.1.1). This was a cylindrical liquid nitrogen trap which had a plate fitted to the bottom to extend the surface area for greater pumping efficiency. A hollow doughnut shaped liquid nitrogen trap was situated above the nozzle chamber within the U-bend. The design of the doughnut liquid nitrogen traps was such that they provided adequate trapping of condensables onto their large surface area without impeding the pumping speed of the vacuum system to any great extent. The third liquid nitrogen trap was another doughnut design sandwiched between the VHS-6 diffusion pump and the bottom flange of the nozzle chamber.

The second chamber is referred to as the detection chamber. This was a Varian six inch six-way cross which housed the SXP-300 quadrupole mass spectrometer. The detection chamber was pumped by a Varian VHS-6 (3000 ls^{-1}) diffusion pump backed by a Varian SD700 (726 $lmin^{-1}$) mechanical pump. Above the VHS-6 diffusion pump was another doughnut liquid nitrogen trap with a second doughnut liquid nitrogen trap between the end of the detection chamber and the quadrupole mass spectrometer flange. These traps provided cryogenic pumping to keep the quadrupole rods free from oil and beam gas condensation. Each diffusion pump was controlled by a time proportional power controller unit to minimise backstreaming and to prevent overheating or burn out of the diffusion pump elements.

Within each chamber was a standard ion gauge (Duniway T-100-K) which monitored the pressure of the chamber on a MKS type 290 controller. The pulsed beam on-beam off pressures within the nozzle chamber were generally $1x10^{-5}$ torr and $1x10^{-7}$ torr, with the detection chamber being $1x10^{-7}$ torr and $5x10^{-8}$ torr. The pressure in the foreline for each mechanical pump was monitored by a thermocouple (various types included MKS TC-1A, Varian 0531, Duniway DST-531) with a MKS type 286 controller. Vacuum failure protection for the machine was facilitated through the setpoint relays on each of the controllers monitoring the pressure in the chambers and forelines. If a vacuum failure was detected then all diffusion pumps would be shut off

and power to the quadrupole mass spectrometer would also be shut off. The protection had a manual reset and was totally bypassed when an experiment was active because of the high beam-on foreline pressures in the nozzle chamber.

Each mechanical pump could be isolated from the system by valves within the forelines. However, the diffusion pumps could not be isolated from the vacuum system. This required the complete cooling of the diffusion pumps before any repairs could be made within the chambers.

All external seals for the chambers were either OFHC copper gasket conflat type seals or viton o-ring seals. All materials within the vacuum chambers were ultra-high vacuum compatible: 316 stainless steel, aluminium, viton o-rings, machineable glass ceramic and teflon sleeved silver wire.

3.1.2 Gas Handling

The gas preparation and handling system consisted of three independently valved freon refrigerant containers (~$5x10^{-2}$ m^3) for storage of gas mixtures to high pressure. The gas line was predominantly copper tubing (0.25 inch) connecting the storage containers to the pulsed supersonic nozzle and vacuum pump. The gas line was pumped by an Edwards ES-150 (150 $lmin^{-1}$) mechanical pump via a glass buffer volume ($1x10^{-3}$ m^3 bulb). The pressure within the gas line was continuously monitored using a 10,000 torr MKS Baratron capacitance manometer. Because of the large volume within the storage containers, compared to the volume of gas exiting the nozzle, the change in backing pressure through an experiment was minimal.

3.1.3 Supersonic Nozzle Source

A commercial electromagnetic pulsed valve (General Valve Corporation, model 9-181) was used as the pulsed supersonic source for the experiments to measure cluster ion appearance potentials. The valve was modified by the addition of a face plate which held a small aperture (JEOL SVC) to reduce the nozzle orifice diameter from 800 μm to 50 μm (Figure 3.1.2). This coincidentally provided a small stagnation volume between the valve and the orifice which produced higher cluster densities than obtained from a direct 50 μm nozzle orifice.

The nozzle was housed in an aluminium carriage assembly (Figure 3.1.2). The position of the carriage assembly could be varied by a linear motion translator (Huntington Mechanical Laboratories, model VF-156) with the carriage assembly being guided by two alignment rods either side of the nozzle. The translator allowed adjustment of the nozzle to skimmer distance from 75 mm to 5 mm with an accuracy of ±1 mm.

The power to the electromagnetic valve solenoid was supplied through a high vacuum electrical feedthrough with the electrical connections being made with vacuum rated teflon sleeved silver wire soldered at both ends. The nozzle was connected by a

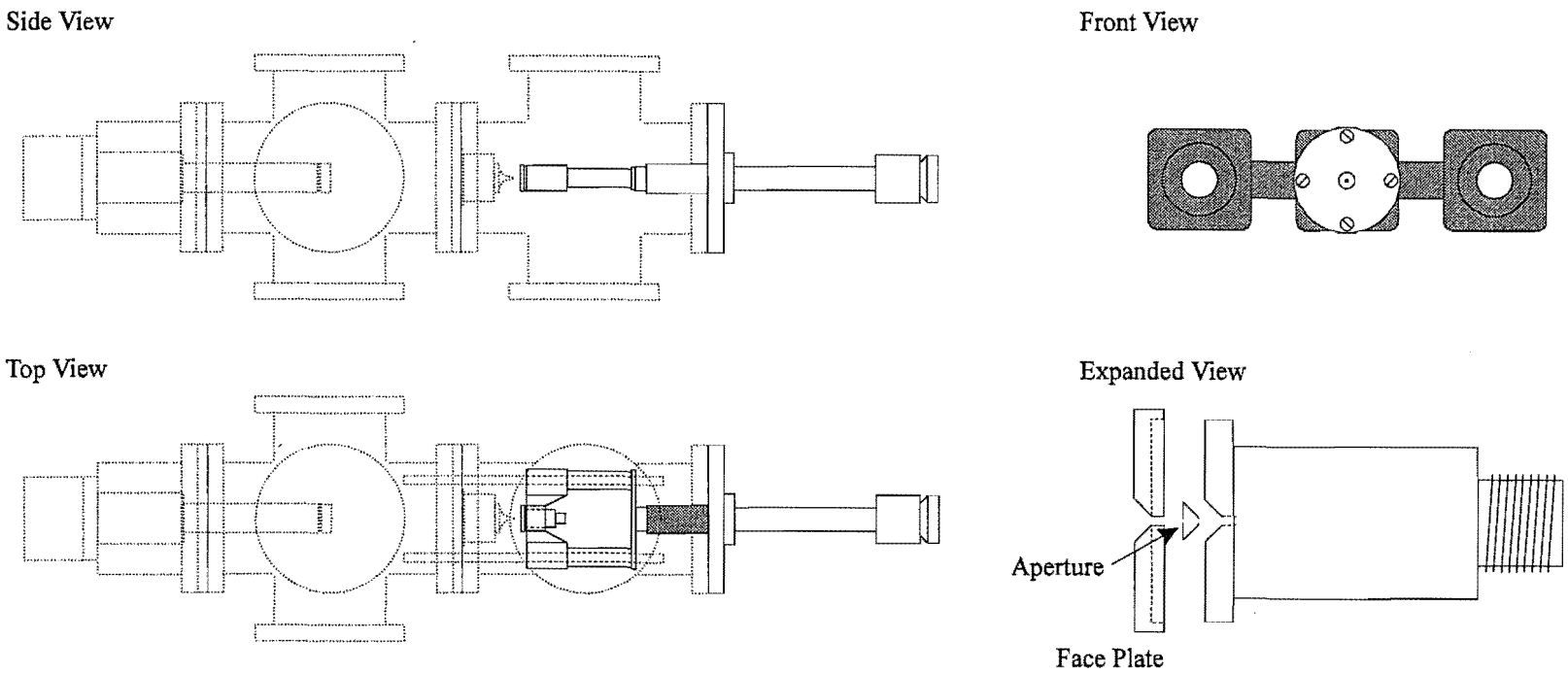

Figure 3.1.2: Side view and top view of the nozzle carriage assembly and its relation to other vacuum components. Front view of the nozzle in the carriage assembly which travels on the two alignment rods. Expanded view of the nozzle is shown to show the placement of the 50 μm aperture and face plate.

0.25 inch diameter flexible stainless steel bellows to a stainless steel Swagelok feedthrough on the nozzle chamber flange, where it joined the gas reservoir line.

3.1.4 Skimmer Assembly

Situated between the nozzle chamber and detection chamber was the skimmer assembly flange which physically divided the chambers for differential pumping. The skimmer flange is shown in Figure 3.1.3. A 1.5 mm diameter skimmer (Beam Dynamics electroformed nickel skimmer) was mounted on a machined glass ceramic holder on the top of an aluminium top hat. The top hat was screwed to the flange, which was wedged between the two chamber flanges. Pressed through the skimmer assembly flange were two alignment rods (10 mm diameter) on which the nozzle carriage assembly travels. The alignment rods were on a four inch diameter and ensured that the supersonic nozzle source and the skimmer were correctly aligned.

3.1.5 Quadrupole Mass Spectrometer

A Vacuum Generators SXP-300 quadrupole mass spectrometer, aligned on axis with the supersonic nozzle and skimmer, was used to collect all of the experimental data on the appearance potentials of cluster ions. The operating principle of a quadrupole mass filter was given in Section 2.5 so only the modifications to the commercial instrument will be discussed in this section.

The commercial unit was purchased with a relatively tight fitting stainless steel sleeve surrounding the quadrupole rods and terminating in a 2.75 inch conflat flange for fitting onto the vacuum system. This sleeve was removed and the quadrupole mass spectrometer mounted on to a six inch diameter top hat on an eight inch conflat flange (shown in Figure 3.1.1). This arrangement allowed more efficient pumping around the quadrupole rods and electron multiplier of the mass spectrometer, and allowed the inclusion of a doughnut liquid nitrogen trap to surround the quadrupole rods to prevent any contamination of the mass spectrometer.

The collection of cluster ion appearance potential data was controlled solely by computer (10 MHz 286 IBM-AT) and custom written computer programs. The mass selection and electron energy of the quadrupole mass spectrometer was controlled by 12-bit digital-to-analogue converters custom built and installed within the mass spectrometer controller unit. These were connected to a commercial driver card (PCL 8255) within the computer. A toggle switch at the back of the controller unit returned the quadrupole mass spectrometer to manual control.

3.1.6 Electronics

Throughout this research many components of electrical equipment have been required. Many times these components were either not available or were too expensive which consequently required that they must be designed and built within the Department. The major components which have been designed and built within this Department are described here and in other similar sections within this chapter.

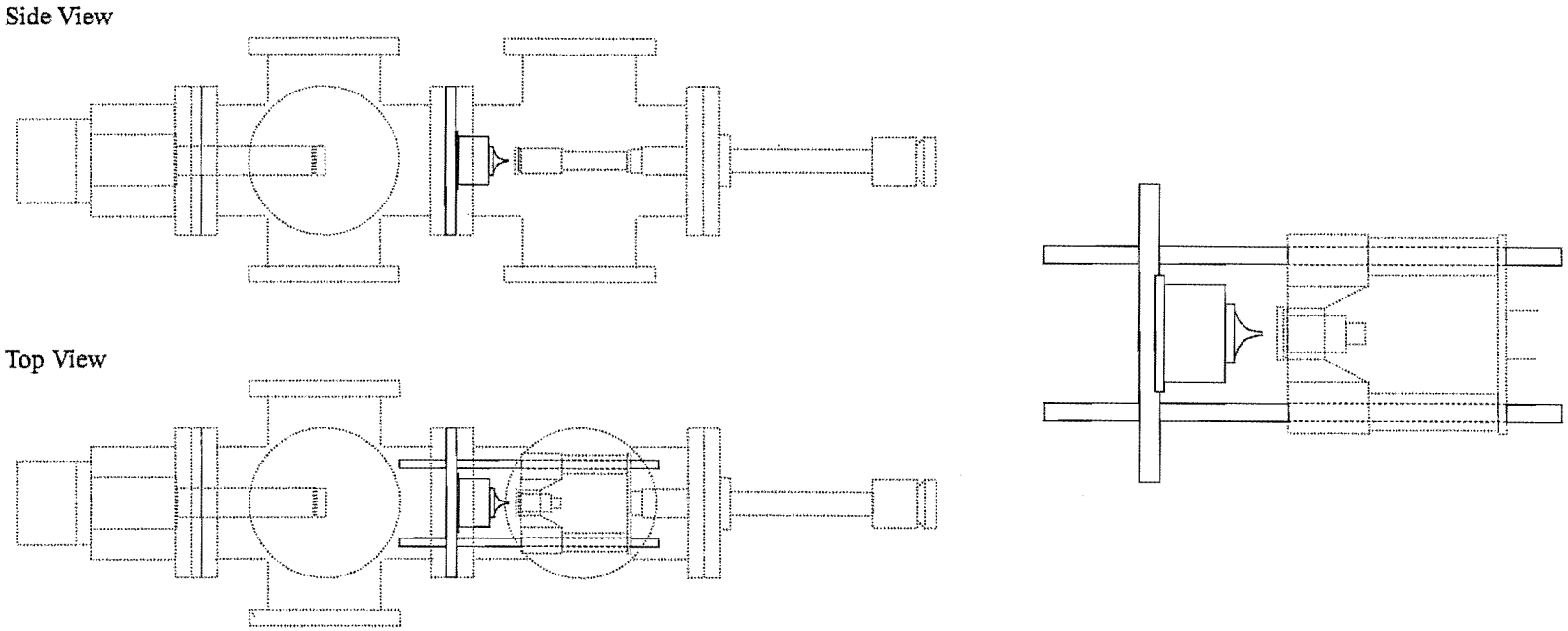

Figure 3.1.3: Side view and top view of the skimmer assembly flange and its relation to other vacuum components. The skimmer assembly flange holds the skimmer top hat and the two alignment rods.

3.1.6.1 Beam Source Driver Unit

The beam source driver unit provided a dual purpose of providing the main trigger for the pulse counting of the signal from the quadrupole mass spectrometer, and in providing the voltage pulse for the pulsed supersonic nozzle (see Figure 4.1.1).

The beam source driver was capable of providing either 12 V or 24 V pulses of variable length and delay to the nozzle solenoid. The frequency of the pulses could be adjusted and monitored from 1 Hz to 1 kHz by appropriate combinations of a three position switch and ten-turn potentiometer. The length of the voltage pulse could also be adjusted from 200 μs to 2.2 ms by another ten-turn potentiometer. For the majority of the measurements described here the pulsed supersonic nozzle was operated at 24 V, 10 Hz with an open time of typically 2.0 ms.

The beam source driver could either provide a 5 V trigger, for the data acquisition described in Section 4.1, or it could be triggered from an external 5 V trigger. If the beam source driver is triggered the delay between the trigger and the nozzle pulse could be varied between 0.2 ms and 5 ms by a ten-turn potentiometer.

The circuit diagram for a modified beam source driver unit is shown in Figure 3.2.4. The modifications from the unit described in this section are detailed in Section 3.2.5.1.

3.2 Stage II - Hexapole Characterisation

Stage II development of the molecular beam machine was a complete change in the research area from clusters to oriented molecules. Before committing completely to oriented molecule research the characterisation of the electrostatic hexapole was completed during this stage. Although there were many other components within the system such as the homogeneous field plates, electron gun, homogeneous field pulsing unit and other particle detectors, these will not be discussed here since any characterisation of those components were repeated and are discussed in Section 3.3. The experiments described in Chapter 5 to determine the asymmetry of electron impact ionisation were attempted at this stage to no great success. They would have been continued at this stage if not for a mechanical pump failure which resulted in the complete cleaning of the vacuum system and hence the premature change from stage II to stage III.

Stage II is very similar to that described in Section 3.1 for stage I. Those components that are identical to stage I are not directly mentioned in this Section.

3.2.1 Vacuum System

The vacuum system for stage II is shown in Figure 3.2.1. The length of the electrostatic hexapole was 833 mm which required two additional chambers compared to

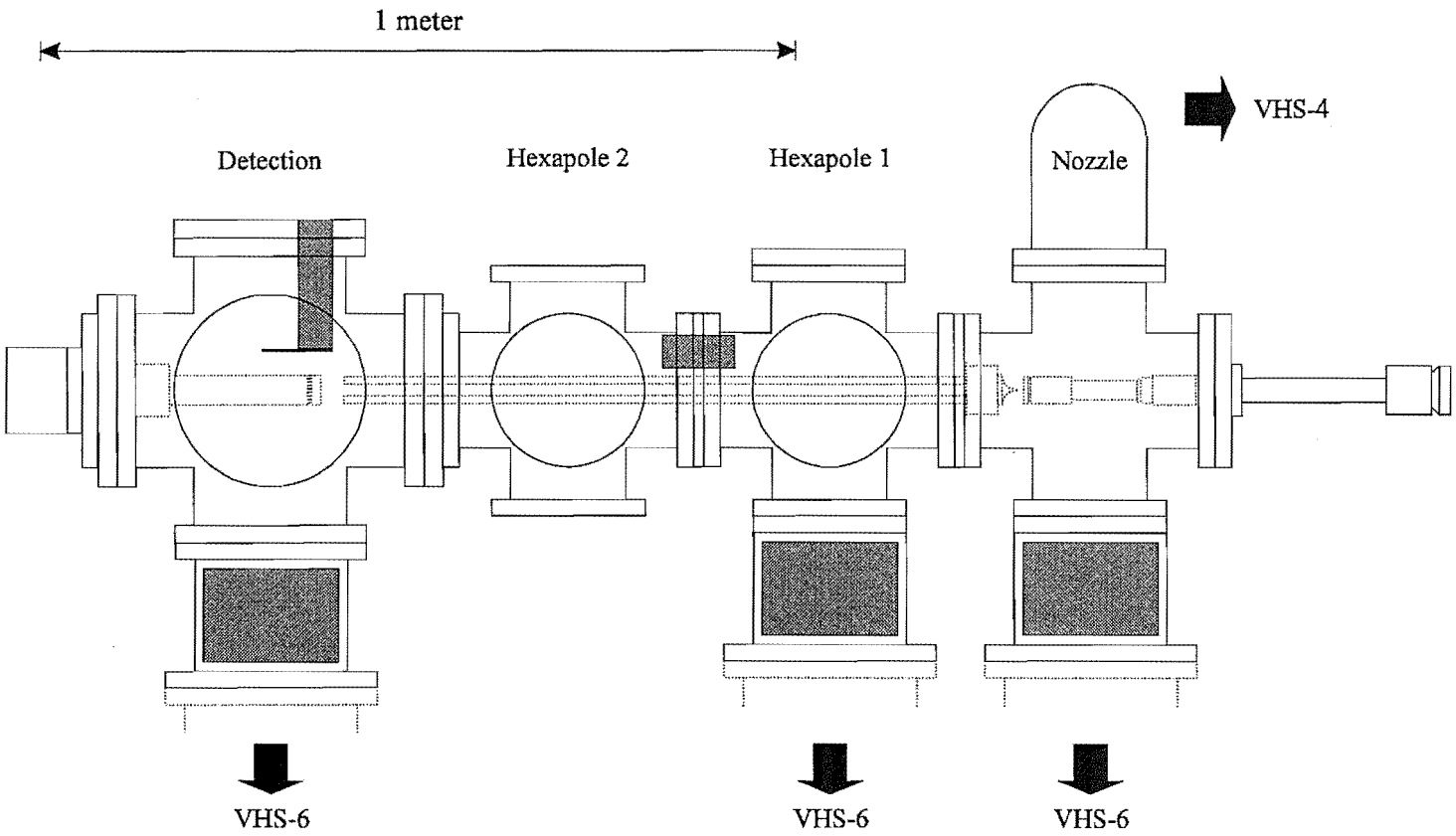

Figure 3.2.1: Vacuum system for characterisation of the hexapole electrostatic filter. The shaded areas indicate liquid nitrogen traps. The extension to the nozzle chamber for the VHS-4 diffusion pump is not shown but is identical to that of Figure 3.1.1.

stage I. The chambers are referred to as: nozzle chamber, hexapole 1 chamber, hexapole 2 chamber and detection chamber (Figure 3.2.1).

The nozzle chamber is identical to that in stage I. It is pumped by a Varian VHS-4 (1500 ls^{-1}) and VHS-6 (3000 ls^{-1}) diffusion pumps with a dual combination of Edwards E2M40 (700 $lmin^{-1}$) and Edwards EDM20 (342 $lmin^{-1}$) mechanical pumps. The nozzle chamber has three liquid nitrogen traps for cryogenic pumping.

The hexapole 1 chamber is similar to the detection chamber of stage I. It is pumped by a Varian VHS-6 (3000 ls^{-1}) diffusion pump backed by a Varian SD700 (726 $lmin^{-1}$) mechanical pump with one doughnut shaped liquid nitrogen trap directly above the VHS-6 diffusion pump. The hexapole 1 chamber contains one of the hexapole mounts which slides onto the alignment rods of the skimmer assembly flange (Figure 3.2.2).

The hexapole 2 chamber is a six inch Varian stainless steel six-way cross which has no direct pumping. It is evacuated by the diffusion pumps either side on the hexapole 1 and detection chambers. The hexapole 2 chamber contains the Huntington feedthroughs for the hexapole high voltage and has a half moon shaped liquid nitrogen trap above the hexapole rods for the trapping of condensables away from the hexapole.

The fourth chamber is the detection chamber. This is an eight inch Varian stainless steel six-way cross and was pumped by a Varian VHS-4 (1500 ls^{-1}) diffusion pump backed by an Alcatel 2004A (75 $lmin^{-1}$) mechanical pump. Directly above the diffusion pump is a doughnut shaped liquid nitrogen trap. A cold finger liquid nitrogen trap, with a copper plate extension, was positioned above the beam crossing region. Between the detection chamber and the hexapole 2 chamber was a six inch to eight inch conflat converter flange which incorporated the second hexapole mount (Figure 3.2.2).

The pressure monitored within the nozzle chamber and hexapole 1 chamber was similar to that in stage I for the nozzle and detection chambers respectively. The pressure within the detection chamber of stage II was also monitored by an ion gauge (Duniway T-100-K) and MKS type 290 controller. This pressure typically varied between $5x10^{-8}$ torr to $5x10^{-7}$ torr when the pulsed supersonic nozzle was off and on respectively (the background pressure did vary depending on how long the system had been continuously pumping following a modification and the levels in the liquid nitrogen traps).

As with stage I, all components and seals within stage II are ultra high vacuum rated to provide the lowest possible residual background pressure.

3.2.2 Nozzle

The nozzle aperture was changed from a 50 μm diameter to a 70 μm diameter for the majority of the characterisations mentioned here. The nozzle assembly remains the same as for stage I.

3.2.3 Electrostatic Hexapole

The electrostatic hexapole was constructed from six 10 mm diameter centreless ground stainless steel rods each 833 mm in length. The inscribed radius, r_o, of the hexapole filter was 7.5 mm and was supported at either end by two perspex mounts: a fixed and floating support.

The hexapole fixed support mounted within the hexapole 1 chamber is shown in Figure 3.2.2. Each rod is held in a recessed groove by a single 3 mm screw to keep the rods equally spaced about the hexapole centre. Between the individual rods are additional keyhole shaped grooves to increase the tracking distance to prevent discharges of the high voltage. The fixed support was made to sit on the existing alignment rods of the skimmer assembly flange via a ball and socket joint shown in Figure 3.2.2. This arrangement was necessary to ensure that the nozzle source, skimmer aperture and hexapole entrance were all collinear. The hexapole rods extended approximately level with the back of the skimmer assembly flange.

The second perspex mount was the hexapole floating support shown in Figure 3.2.2. The hexapole floating support had the same design as the hexapole fixed support for attaching the hexapole rods and for prevention of high voltage discharges. The hexapole floating support is attached to the six inch to eight inch conversion flange, between the hexapole 2 chamber and the detection chamber, by four 8 mm bolts through 10 mm clearance holes. The requirement for the conversion flange to have the four 8 mm support holes and, also, to allow the passage of the hexapole fixed support, for installation of the hexapole, determined the shape of the fixed support and the shape of the internal cavity in the conversion flange. The clearance for the 8 mm screws allowed the hexapole floating support and the hexapole exit to be laser aligned. Two 12 mm holes, drilled through the hexapole floating support, allowed support and alignment of the homogeneous electric field plates discussed in Section 3.3.8. From the face of the hexapole floating support the hexapole rods extended approximately 108 mm into the detection chamber. The relative position of the two hexapole supports could be easily determined by calculation knowing the experimental arrangement.

Correct alignment of the hexapole is important as the hexapole focuses molecules onto the hexapole axis. To set the appropriate alignment a helium-neon laser was reflected through the skimmer (with the nozzle removed) and adjusted to pass through cross hairs on the detection chamber axis. The floating support was adjusted to superimpose the hexapole axis and the laser axis. Similarly, once the hexapole is aligned, the quadrupole mass spectrometer could also be aligned using the laser beam.

The electrical connections for the hexapole rods came through two Huntington high voltage feedthroughs each rated to 30 kV (one each for the positive and negative supplies). Each feedthrough has a copper braid attached to it which then connects to a copper ring by a push on clasp. The two rings encircle the hexapole rod assembly and provide the appropriate voltage, to alternate rods, through 2 mm copper studs pressed into the hexapole rods and soldered to the ring. To remove the hexapole rods each of the six studs are required to be removed initially.

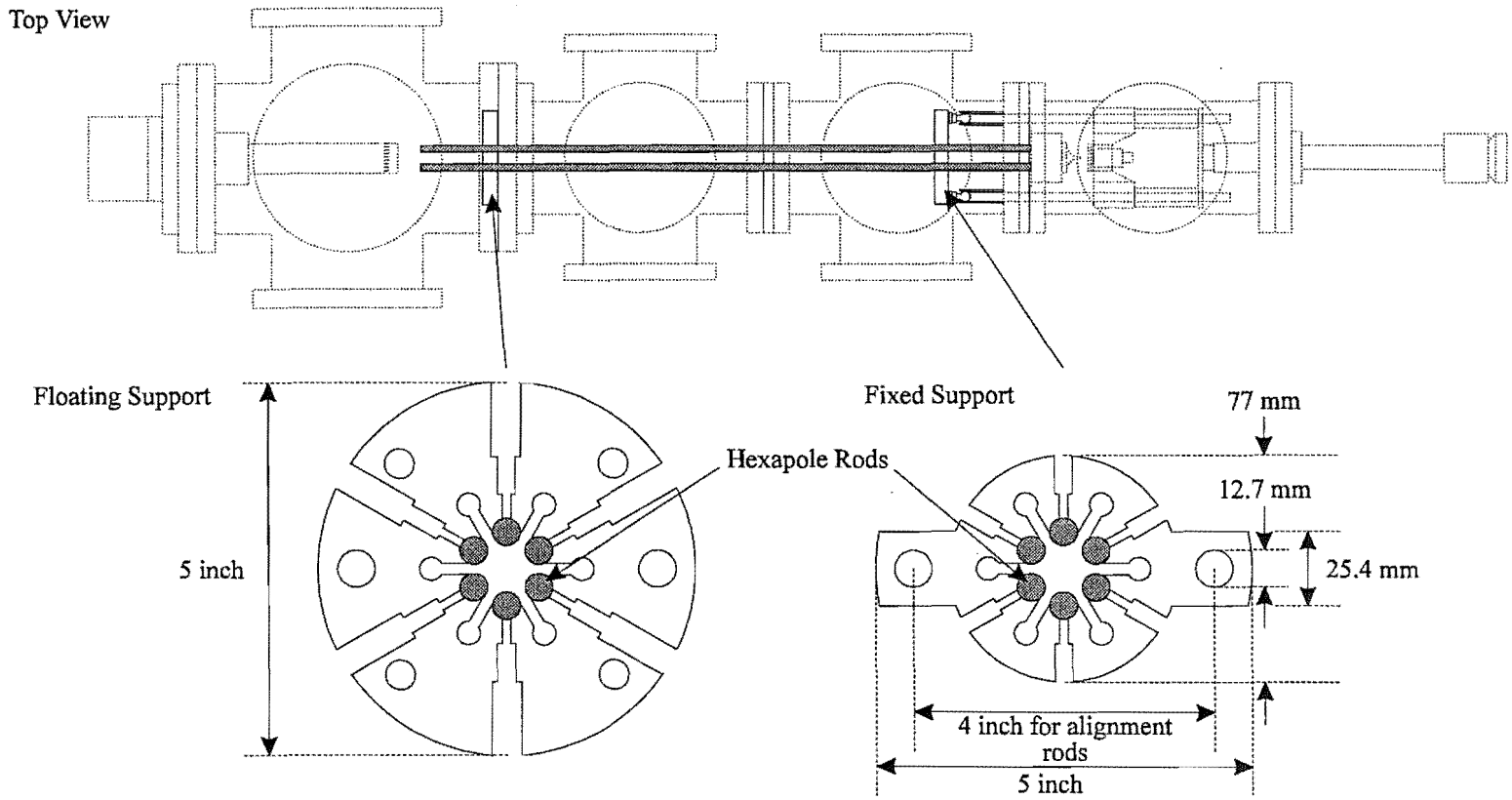

Figure 3.2.2: The hexapole fixed and floating supports. Each support is 20 mm thick perspex. The fixed support is attached to the alignment rods by two ball and socket stainless steel sleeves. The floating support is connected to the six inch to eight inch conversion flange by four bolts with enough clearance to allow correct alignment of the hexapole axis.

3.2.4 Quadrupole Mass Spectrometer

The Vacuum Generators SXP-300 quadrupole mass spectrometer was removed from the top hat arrangement of stage I and connected directly to the detection chamber as shown in Figure 3.2.1. This arrangement positioned the quadrupole ion source closer to the end of the hexapole. A cold finger liquid nitrogen trap was inserted into the detection chamber to facilitate cryogenic pumping of the detection chamber.

3.2.5 Electronics

3.2.5.1 Beam Source Driver Unit

The nozzle beam source driver unit (Figure 3.2.3) has one added feature to that described for stage I. The beam source driver was modified to accept an external voltage of 12-200 V to drive the nozzle. The opening time for the electromagnetic solenoid is dependent on the power supplied to the solenoid. By increasing the amplitude of the voltage pulse using an external supply, it was possible to reduce the opening time of the nozzle. In the experiments described here the voltage pulse to the supersonic nozzle was typically 37 V with a pulse width of between 1.2-1.6 ms. The effect of the higher voltage tended to increase the wear on the teflon poppets within the electromagnetic valve which resulted in an increased incidence of teflon flakes blocking the 70 μm aperture.

The primary trigger for data collection was now provided by the pulse counting controller (Section 3.2.5.2). The beam source driver was externally triggered by the pulse counting controller with the delay of the voltage pulse kept to the minimum setting (0.2 ms).

3.2.5.2 Pulse Counting Controller

The pulse counting controller provided the primary trigger and data collection (Figure 3.2.4). The frequency of the primary trigger could be varied between 1, 10 and 100 Hz by a three position switch, with two BNC trigger outputs for simultaneous triggering of other components. Although the frequency range was limited, all experiments were conducted at a frequency of 10 Hz as this suited the pulsing of other components.

The pulse counting controller provided the master trigger pulse which synchronised the signal gates through variable delays for an experiment. In pulse counting mode, the quadrupole mass spectrometer electron multiplier outputs a stream of narrow pulses of different heights superimposed on any noise present. The preamplifier/discriminator electronics amplifies the pulses, removes those below a set threshold level and then outputs the resultant pulses as 5 V amplitude with a width of typically 250 ns. These are the signal pulses that are input to the pulse counting controller through a BNC connector.

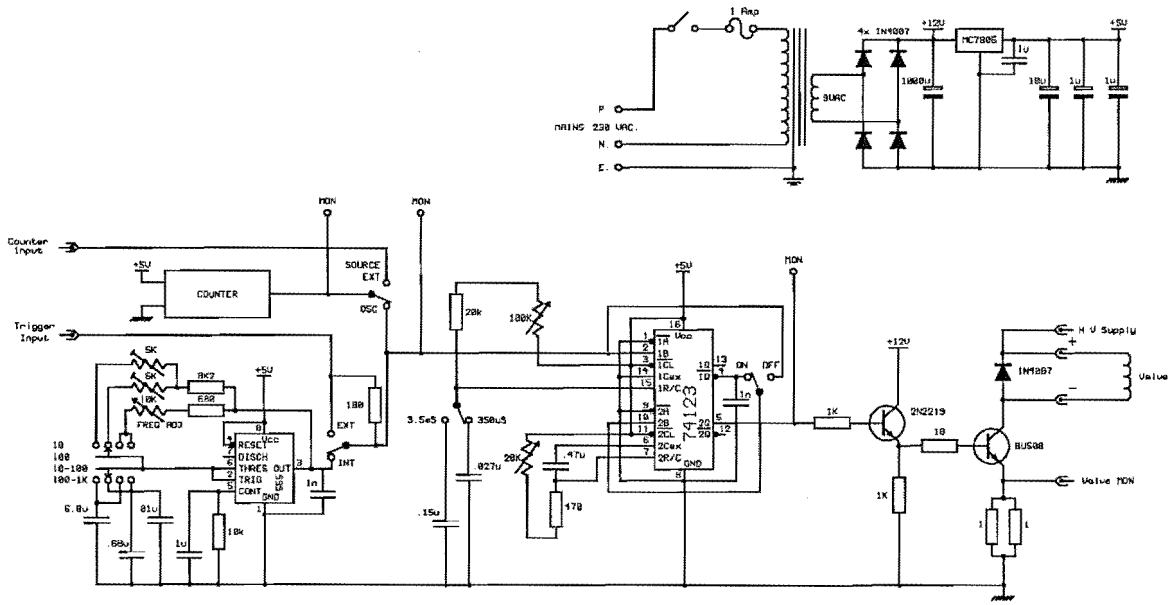

Figure 3.2.3: Beam source driver circuit diagram. The circuit shown allows control of the pulse frequency, width and delay of the supersonic nozzle electromagnetic valve. The circuit also allows the input of an external voltage to operate the electromagnetic valve.

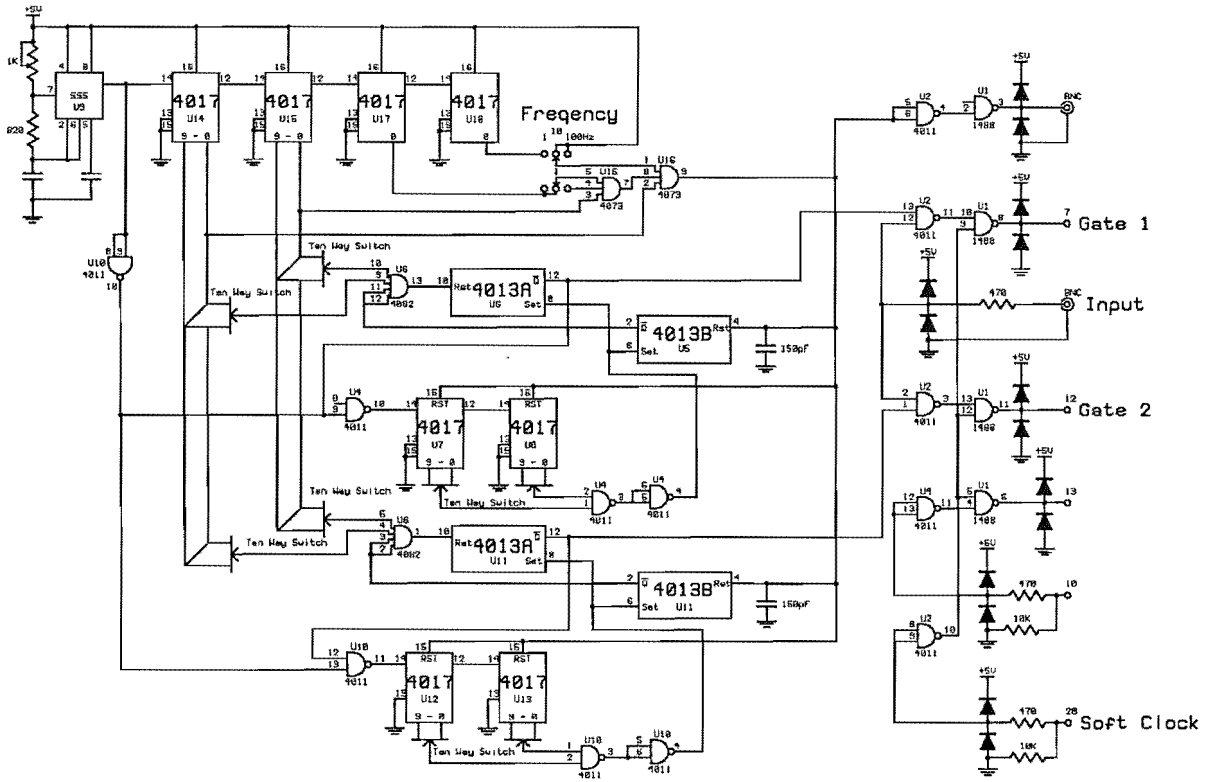

Figure 3.2.4: Pulse counting controller circuit. This circuit allows control of the width and delay of the two pulse counting gates, gate 1 and gate 2 (see text). The circuit allows input of the signal pulses to be individually and-gated with the two pulse counting gates with the resultant signals output for counting by computer.

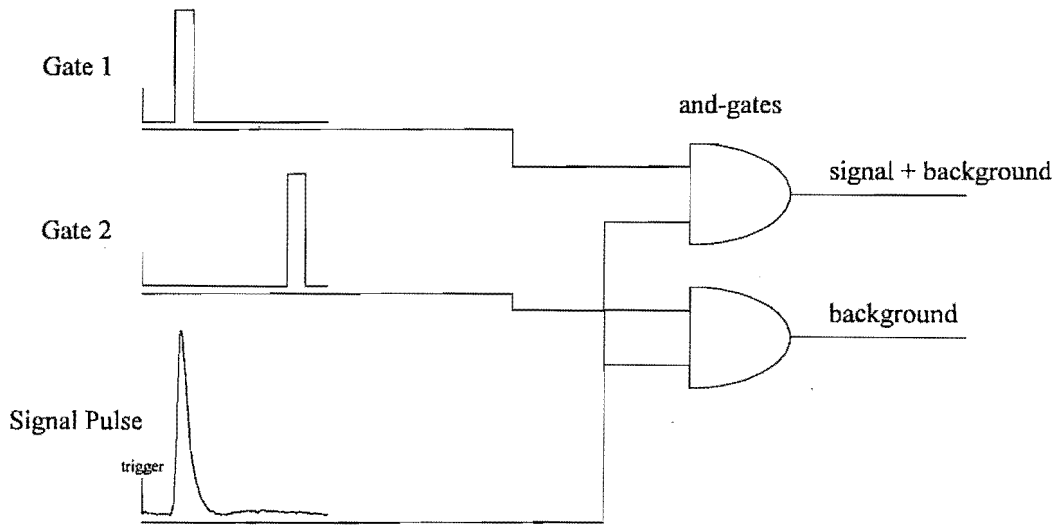

Figure 3.2.5: Gating arrangement employed to distinguish between beam signal and background pulses. The input and output to the and-gates are all discrete +5 V TTL pulses. The output from the and-gates is counted by computer.

The internal trigger of the pulse counting controller represents time zero for two TTL gates. The delay of each gate could be individually varied between 0-9.9 ms in 0.1 ms steps by the combination of two ten turn pots, one for the 1 ms divisions and one for the 0.1 ms divisions. The width of the two gates is varied by another two pots for control between 0-3.9 ms in 0.1 ms steps. The signal pulses and the voltage gates are then and-gated as shown in Figure 3.2.5. The and-gate only passes the signal when both and-gate inputs are high (+5 V). The two gates are positioned so that gate 1 covers the required signal + background and gate 2 covers only background either well before or well after gate 1. The difference between the number of pulses under each of the two gates then gives the signal. The output pulses from the two and-gates are passed by ribbon cable to a counter-timer card (8253 chip on an PCL-8255 card) and recorded via custom written interfacing software.

3.2.5.3 Hexapole

The voltage for the hexapole rods are supplied by two (one positive and one negative polarity) 30 kV power supplies (Glassman High Voltage Inc., EH series) which are both computer controlled. The control for the high voltage supplies was achieved using a custom built 12-bit digital-to-analogue converter to output a voltage between 0-10 V. The 0-10 V voltage represented a linear ramp for the high voltage supplies from zero to full scale, so that the high voltage could be set to an accuracy of ±7 V. The two voltage supplies were linked in parallel to the same digital-to-analogue converter so that each supply outputted the same high voltage magnitude. The voltages on each of the rods were periodically checked and never deviated by more than 0.5% between supplies at 900 V.

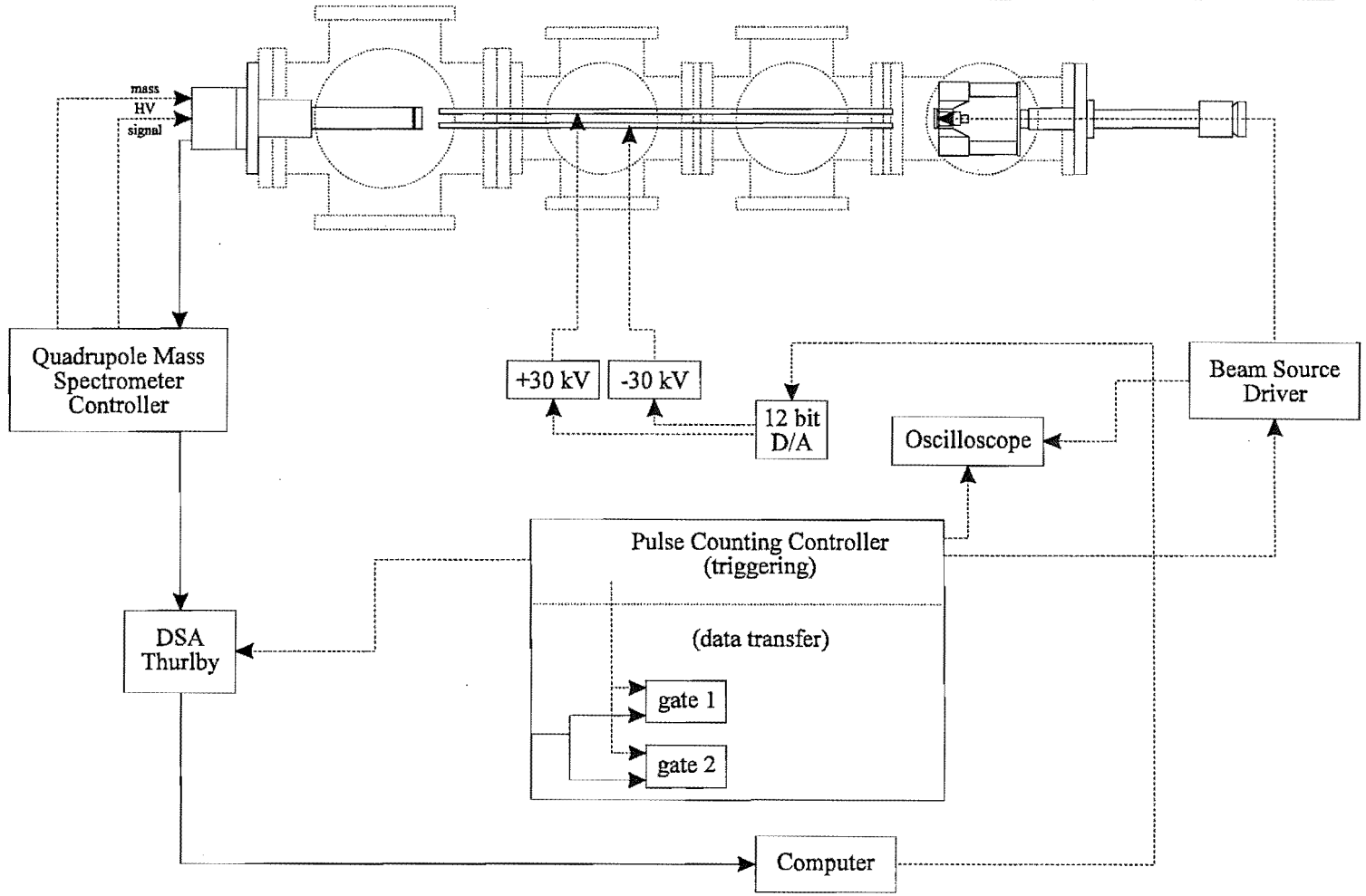

Figure 3.2.6: Experimental arrangement for the analog collection of arrival time distributions. For this arrangement the pulse counting controller provides the trigger but does not handle any data transfer.

3.2.6 Hexapole and Beam Characterisation

The characterisation of stage II involved characterising the hexapole electrostatic field and determining its effect on various symmetric top molecules. This was achieved using analogue measurement of arrival time distributions and pulse counting.

The experimental arrangement for the analogue collection of arrival time distributions is shown in Figure 3.2.6. Initially the hexapole voltage is set to the required potential and the ion mass on the quadrupole mass spectrometer is also set. The pulse counting controller provides the trigger for both the beam source driver and the Thurlby DSA524 (digital storage oscilloscope). The current pulses from the electron multiplier are returned to the mass spectrometer controller where they are amplified. The output is then recorded by the Thurlby with an average over 64 shots representing one scan. The Thurlby communicates with the computer through one of the COM ports driven by custom written software and manual control of the sensitivity. Shown in Figure 3.2.7 are arrival time distributions for CH_3Cl and 5% $(CH_3)_3CCl$/Ar at different hexapole voltages. These distributions show the focusing effect of increased signal intensity with increasing hexapole voltage. Typically these distributions have been averaged over 10 scans.

The experimental arrangement for pulse counting is shown in Figure 5.3.1. The pulse counting controller again provides the primary trigger to the beam source driver and collects the 5 V pulses from the preamplifier/discriminator where they are and-gated with gate 1 and gate 2 (Figure 3.2.5) and counted by the computer. The position of gate 1 and gate 2 of the pulse counting controller can be determined from the position of the arrival time distribution in Figure 3.2.7. Shown in Figure 3.2.8 are transmission curves recorded for CH_3Cl and $(CH_3)_3CCl$. They show that as the hexapole voltage increases the intensity observed increases as the hexapole focuses more molecules to the beam axis. No rotational state selection features are observable since the experimental conditions, aperture diameters and absence of a beam stop, were chosen to give the greatest possible transmitted signal.

The characterisation of the hexapole satisfied two requirements for future studies; (i) establishing the best conditions to achieve a good signal level with no hexapole field and (ii) achieving an acceptable increase in signal level with the maximum hexapole voltage.

The molecules characterised during this period included: CH_3Cl, CH_3I, CH_3CN, CH_3OH, $CHBr_3$, CF_3Br, $(CH_3)_3COH$, $(CH_3)_3CCl$ and $(CH_3)_3CBr$. Many of these were also characterised in seeded mixtures with argon and krypton to vary the translational energy of the symmetric top molecule. The results obtained in this section of work formed the basis of the work described in Section 3.3 for the cross beam experiments.

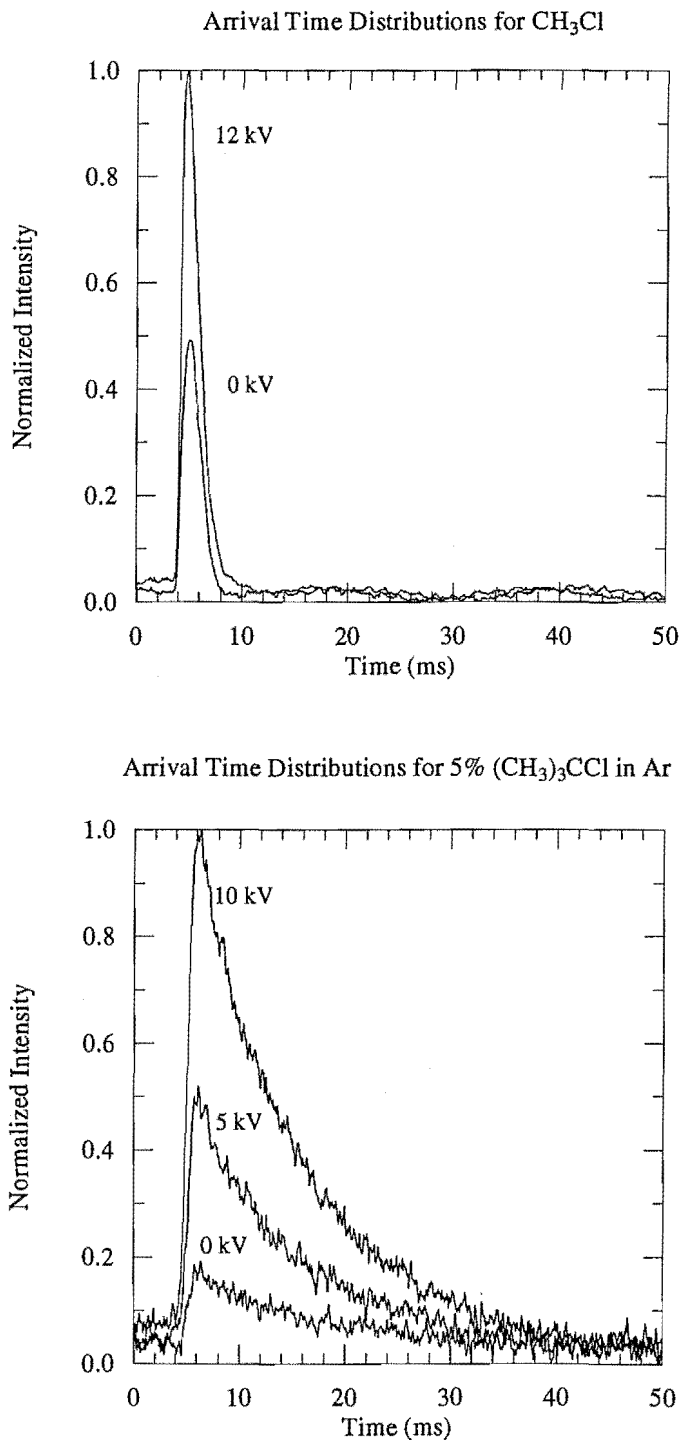

Figure 3.2.7: Arrival time distributions for CH_3Cl and 5% $(CH_3)_3CCl$/Ar. As the hexapole voltage is increased a greater number of molecules are focused onto the hexapole axis and a higher signal intensity is measured.

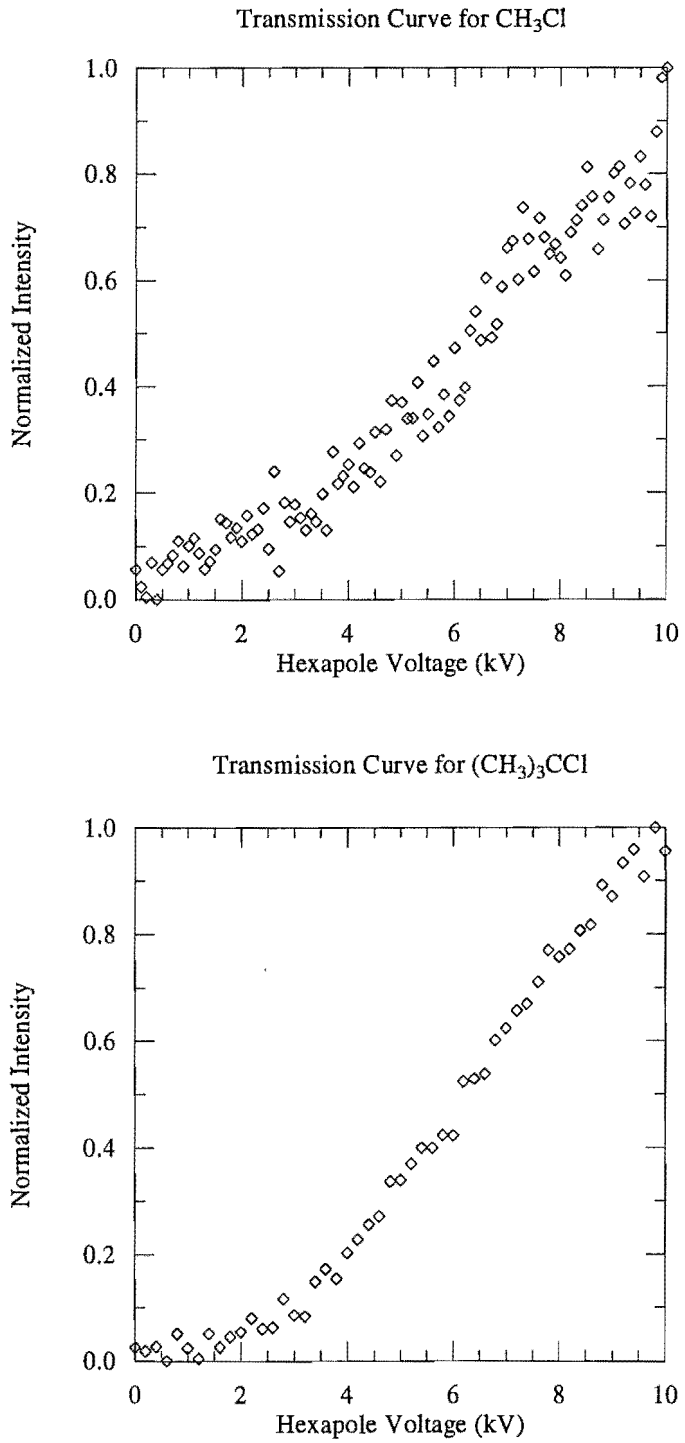

Figure 3.2.8: Transmission curves for CH_3Cl and $(CH_3)_3CCl$. As the hexapole voltage is increased a greater number of molecules are focused onto the axis which results in an increased signal intensity.

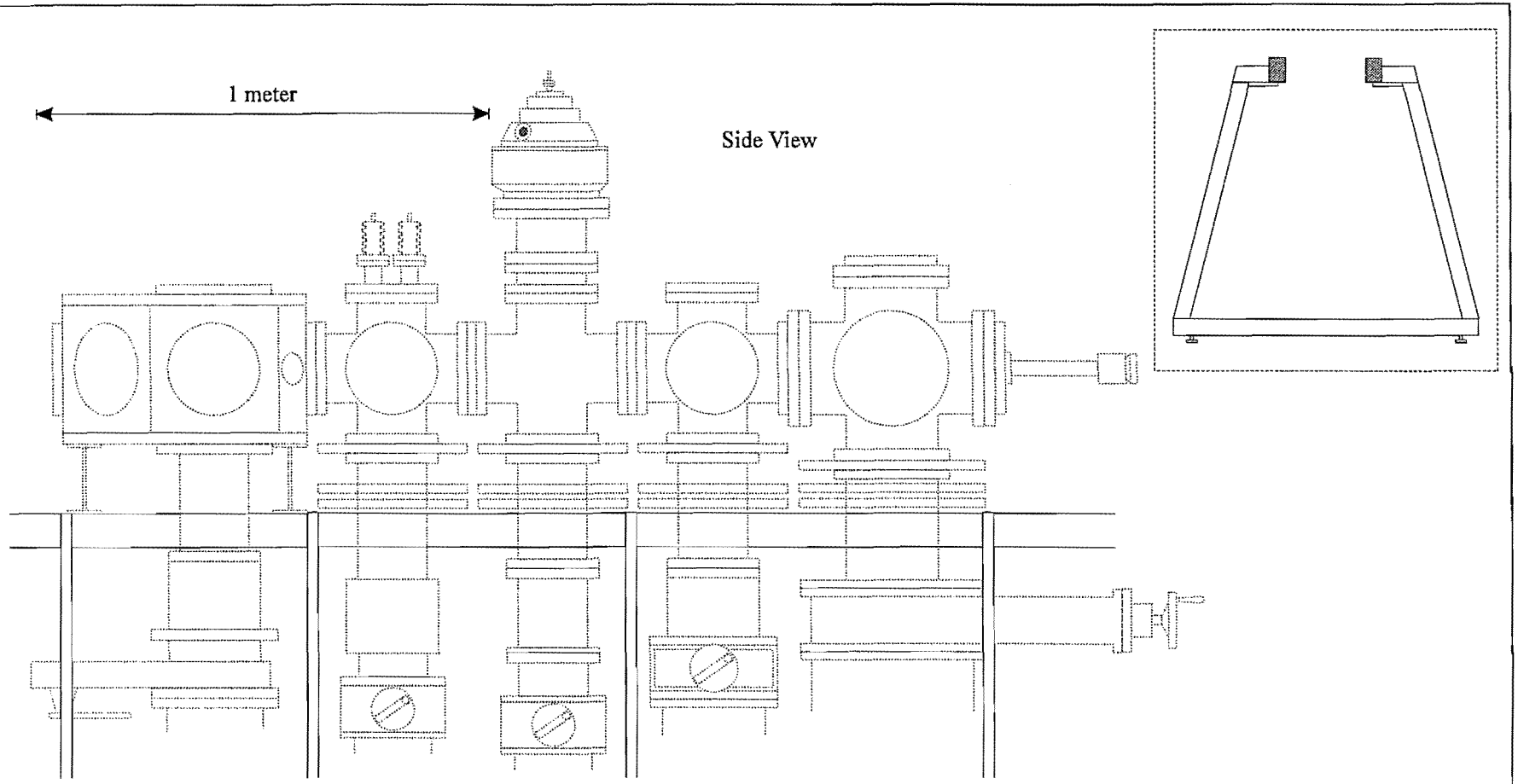

Figure 3.3.1: Location of rails and legs in relation to the vacuum system. The rails are 4 m in length with a leg at each end (not shown). Inset: general leg design to provide internal clearance for the diffusion pumps and gate valves and to provide stability with two rubber feet. The additional horizontal and diagonal supports between the legs are not shown.

3.3 Stage III - Cross Beam Experiments

Stage III of the molecular beam machine was originally designed to increase the versatility of the existing stage II design. The primary focus for stage III was the ability to study ion-oriented molecule reactions in the future. A new scattering chamber was designed and built within the Department to facilitate a rotatable mass spectrometer in future research. The new scattering chamber gave the opportunity of redesigning the vacuum system to include a larger nozzle chamber with increased pumping capacity and to include a differentially pumped buffer chamber. The perceived changes to the machine made it necessary to design a new frame and also to modify some components within the vacuum system. These changes will be described below.

3.3.1 Frame

The first consideration for the stage III development was the design of a new frame as the existing frame was not expected to be able to hold the weight of the new scattering chamber and Varian VHS-10 diffusion pump. The specific features that the new frame was required to satisfy were; strength, stability, ease of modification and accessibility.

The new frame was designed around a pair of rails mounted on a series of legs such that the chambers could move freely along the rails. The increased weight of the nozzle and scattering chambers required the rails to be constructed from 75x50 mm steel box, with the longer dimension vertical. The length of the rails was four meters which was as long as the available space allowed. The spacing between the rails was 320 mm which was the minimum distance required to remove one of the middle chambers out through the rails in the frame assembly.

Stability was a major concern in the design of the frame as any vibration, from mechanical pumps, winding of gate valves etc., could destroy the alignment of the hexapole and detectors. A series of six legs were used to support the rails. Each leg had a variable height adjustment on two rubber feet for the levelling of the rails and for prevention of vibration. The position of each leg was determined by the weight distribution and the necessity to maintain access to gate valves and foreline valves (Figure 3.3.1). The rails were held in place by an 8 mm bolt through the rail into the angle support of each leg. Additional stability was provided by horizontal supports between the rails and between adjacent legs and by angle supports connecting three adjacent legs. All components of the frame were made such that individual parts could be removed and replaced while *in situ*. The removal of a leg would not affect the overall stability of the frame but would aid in the ease of modification if a chamber was required to be moved.

An important new feature was the implementation of a roof mounted chain-pulley assembly. The pulley allowed easy raising and lowering of the scattering chamber lid for access into the scattering chamber and the ability to raise any of the middle chambers out of the assembly if required. All mechanical pumps, forelines, foreline valves and gate valve handles were all positioned on the same side of the machine to increase

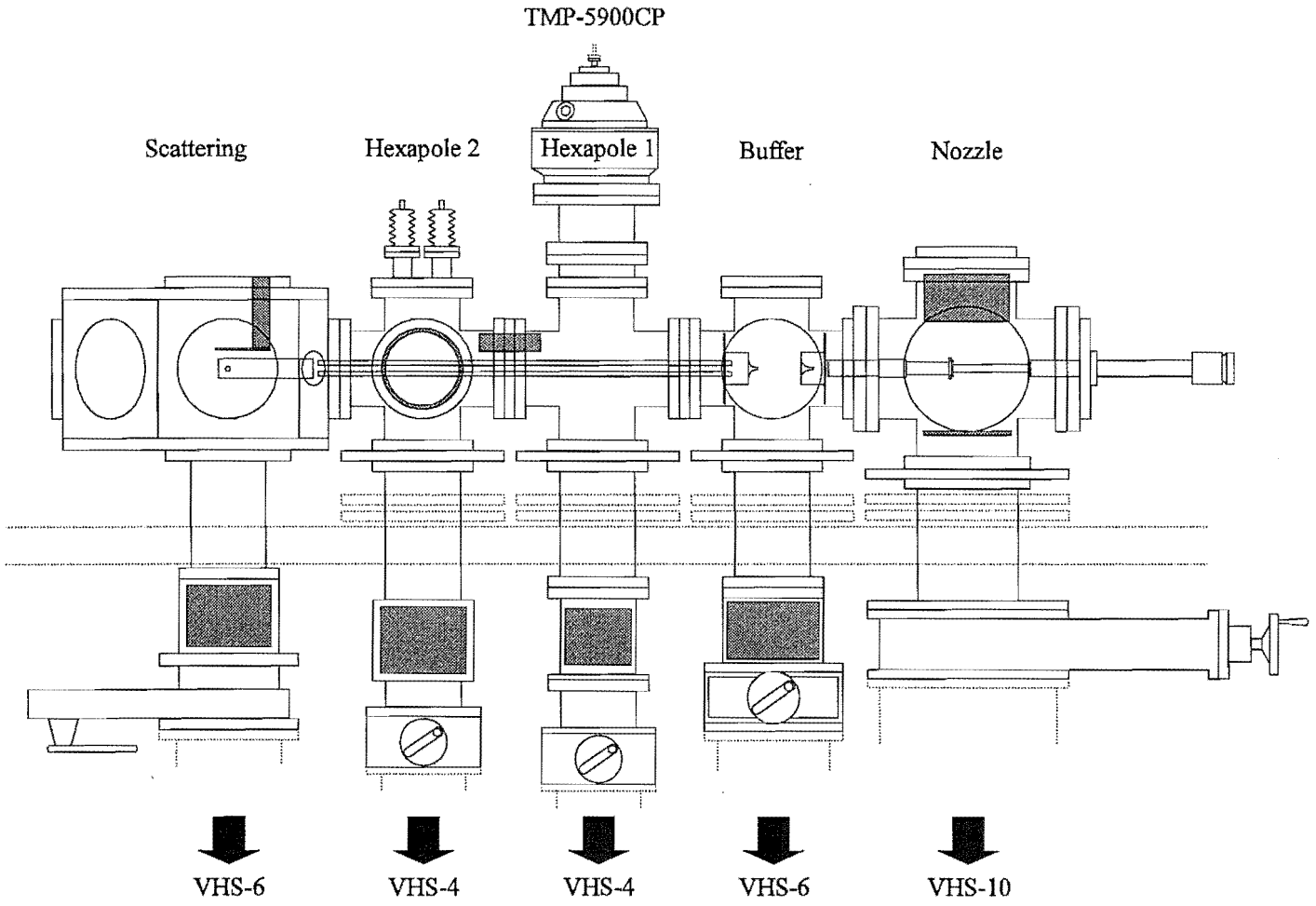

Figure 3.3.2: Vacuum system for electron impact ionisation asymmetry measurements. The frame legs and diffusion pumps are removed for clarity. The shaded areas indicate liquid nitrogen traps and the major internal components are also shown.

accessibility into the machine chambers from the opposite side. The internal components of the vaccum system were designed such that the majority of the assembly could be achieved from only one side of the machine. Additional accessibility was achieved by removing the power distribution from the machine frame (as positioned in stage I and stage II) into a dedicated frame.

The height of the rails, and subsequent heights of the legs, was determined by the minimum height requirement of the nozzle chamber. Once this height was determined the scattering chamber could be fixed in position.

3.3.2 Vacuum System

The vacuum system, excluding the frame, legs and diffusion pumps, is shown in Figure 3.3.2. The five chambers are designated; nozzle chamber, buffer chamber, hexapole 1 chamber, hexapole 2 chamber and scattering chamber (or detection chamber).

The eight inch Varian six-way cross of stage II became the nozzle chamber for stage III. It was pumped by a Varian VHS-10 (7020 ls^{-1}) diffusion pump and backed by an Alcatel 2063C (1080 $lmin^{-1}$) mechanical pump. The greater volume of the nozzle chamber and the greater pumping speed on the chamber allowed higher backing pressures, longer nozzle open times or higher duty cycles to be used for the nozzle if necessary.

The buffer chamber contained two moveable skimmer flanges and was pumped by a Varian VHS-6 (3000 ls^{-1}) diffusion pump backed by an Edwards E2M40 (700 $lmin^{-1}$) mechanical pump. The buffer chamber increased the collimation of the pulsed supersonic beam, by having a second differentially pumped chamber, and reduced the pressure of scattered beam molecules around the entrance to the hexapole to facilitate the use of higher hexapole voltages.

The hexapole 1 and hexapole 2 chambers form a continuous volume identical to that of stage II. The flanges between the chambers remained the same to keep the hexapole mounts in the same relative positions. Both chambers were pumped by individual Varian VHS-4 (1500 ls^{-1}) diffusion pumps with the hexapole 1 chamber being backed by an Edwards EDM20 (342 $lmin^{-1}$) mechanical pump and the hexapole 2 chamber backed by an Alcatel 2004A (75 $lmin^{-1}$) mechanical pump. A major modification to the hexapole chambers was the inclusion of an Alcatel turbo molecular pump (model TMP-5900CP, 880 ls^{-1}), backed by an Alcatel 2020A (373 $lmin^{-1}$) mechanical pump, to the top port of the hexapole 1 chamber. The turbo molecular pump was only used for the continued evacuation of the chambers overnight when the diffusion pumps were gated-off.

The scattering chamber was designed and constructed within the Chemistry Department. Although the scattering chamber is not charged with a heavy gas load its large volume and surface area required a large pumping capacity and it was pumped by a Varian VHS-6 (3000 ls^{-1}) diffusion pump backed by a Varian SD700 (726 $lmin^{-1}$) mechanical pump.

The scattering chamber was constructed from one inch thick type 304 stainless steel and consisted of eight sides as indicated in Figure 3.3.3a and Figure 3.3.3b. Each of the five larger sides carried an eight inch conflat seal positioned such that all the centres intersected at the scattering centre. The smaller B sides and side C have additional 2.75 inch conflat seals for electrical feedthroughs, bleed valves, ion gauges etc. Each of the internal surfaces had 8 mm tapped blind holes on a one inch grid. These were used to connect grounding shields, mounts for various components and for directing wire around the scattering chamber. Each screw in a blind hole had the central core removed for pumping of the dead space at the bottom of the blind hole.

The top flange of the scattering chamber had a ten inch conflat machined into the flange face about the scattering centre, with two 4.5 inch conflats and one 2.75 inch conflat on 48 mm and 44 mm stand-offs respectively for additional feedthroughs. The top flange was sealed by a captured viton o-ring set into the lid which was periodically smeared with diffusion pump oil, and nine 6 mm securing screws. On top of the flange was the lifting rig and lead balancing blocks for the smooth raising and lowering of the lid using the roof mounted chain-pulley.

The bottom flange was also sealed by a captured viton o-ring and securing screws. The bottom flange had a ten inch conflat seal machined on its face centred at the beam crossing centre and a 2.75 inch conflat and 4.5 inch conflat on 30 mm and 175 mm stand-offs respectively. The bottom flange of the scattering chamber was supported 157 mm from the top of the rails by two H-beams (Figure 3.3.1). A small amount of adjustment could be obtained from three screws that could tip the scattering chamber to ensure that the front face of the scattering chamber was perpendicular to the rails.

Once the scattering chamber was positioned then the other chambers could be aligned relative to it. A mounting trolley consisting of three plates was designed to provide the necessary three dimensional adjustment of the remaining chambers (Figure 3.3.4 and shown on the machine in Figure 3.3.2). The first plate could roll along the rails providing the longitudinal motion (a guiding track was fixed down the length of one rail to prevent the plate from running off-course). The second plate could run across the first plate, with two studs from the first plate as guides, and provide the transverse motion. These two plates were box-like so as they could fit over the spool for the chamber. The third plate was the connecting plate. This plate was fixed between the chamber and the spool by blind holes on either side of the plate. Four threaded one inch diameter studs were welded onto the corners of the second plate and passed through clearance holes on the connecting plate. The connecting plate then sat on four nuts threaded onto the studs and by adjusting the nut height the vertical motion was achieved. Before the chambers would be connected together each direction would be adjusted so that the face of each chamber was parallel and no undue stresses would be placed on any one seal.

Each of the chambers of stage III had gate valves directly above the diffusion pumps to gate-off the vacuum system overnight. Additional spools were constructed to position the gate valves under the rail height as shown in Figure 3.3.2. A series of liquid nitrogen traps (Figure 3.3.2) were situated throughout the vacuum chambers to increase

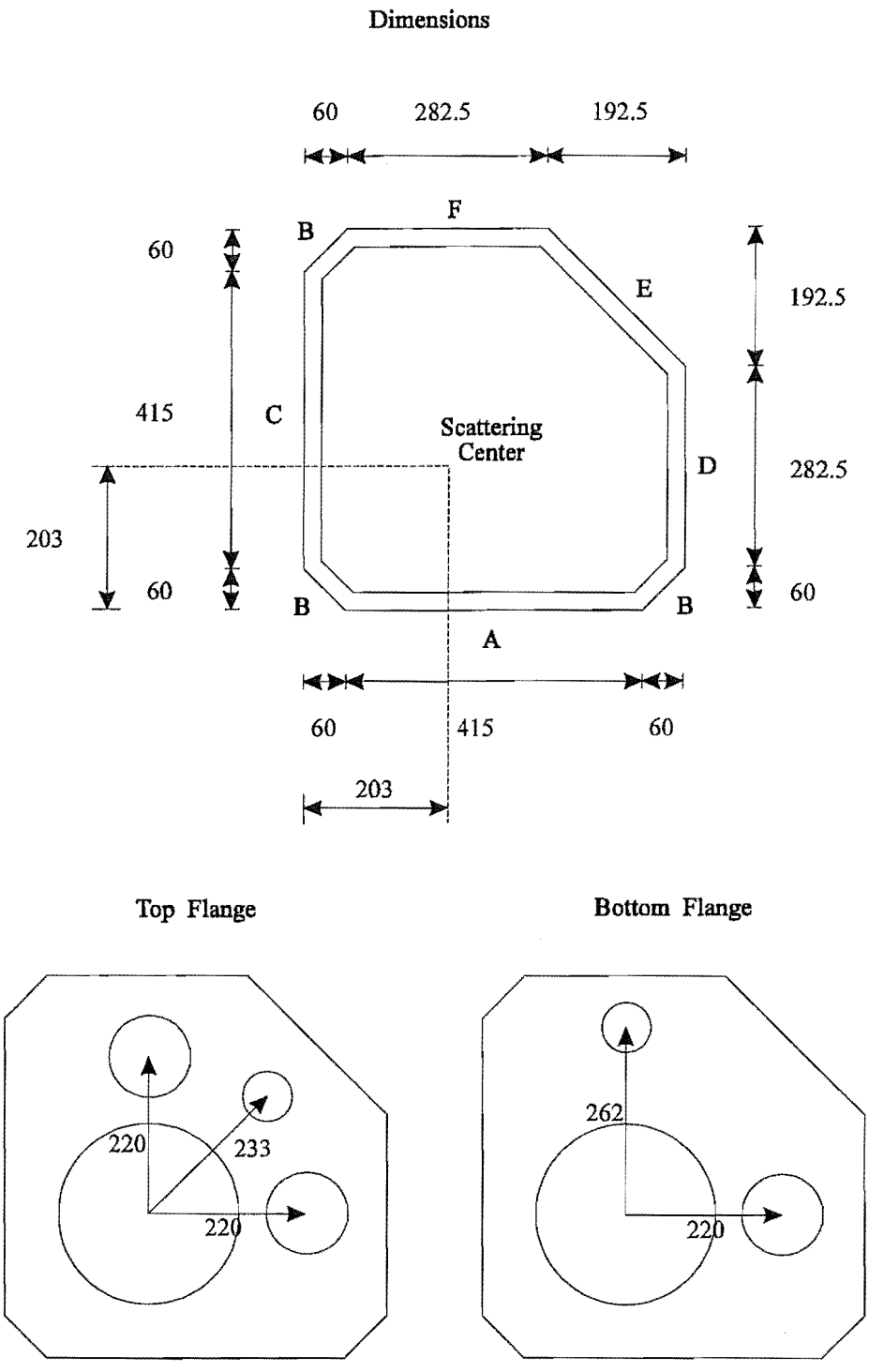

Figure 3.3.3a: Top view of the scattering chamber indicating the dimensions and letter allocation of each of the sides. The top flange and bottom flange are also shown with appropriate distances from the major conflat seal to other available ports. Each port is either a 10 inch, 4.5 inch or 2.75 inch conflat seal.

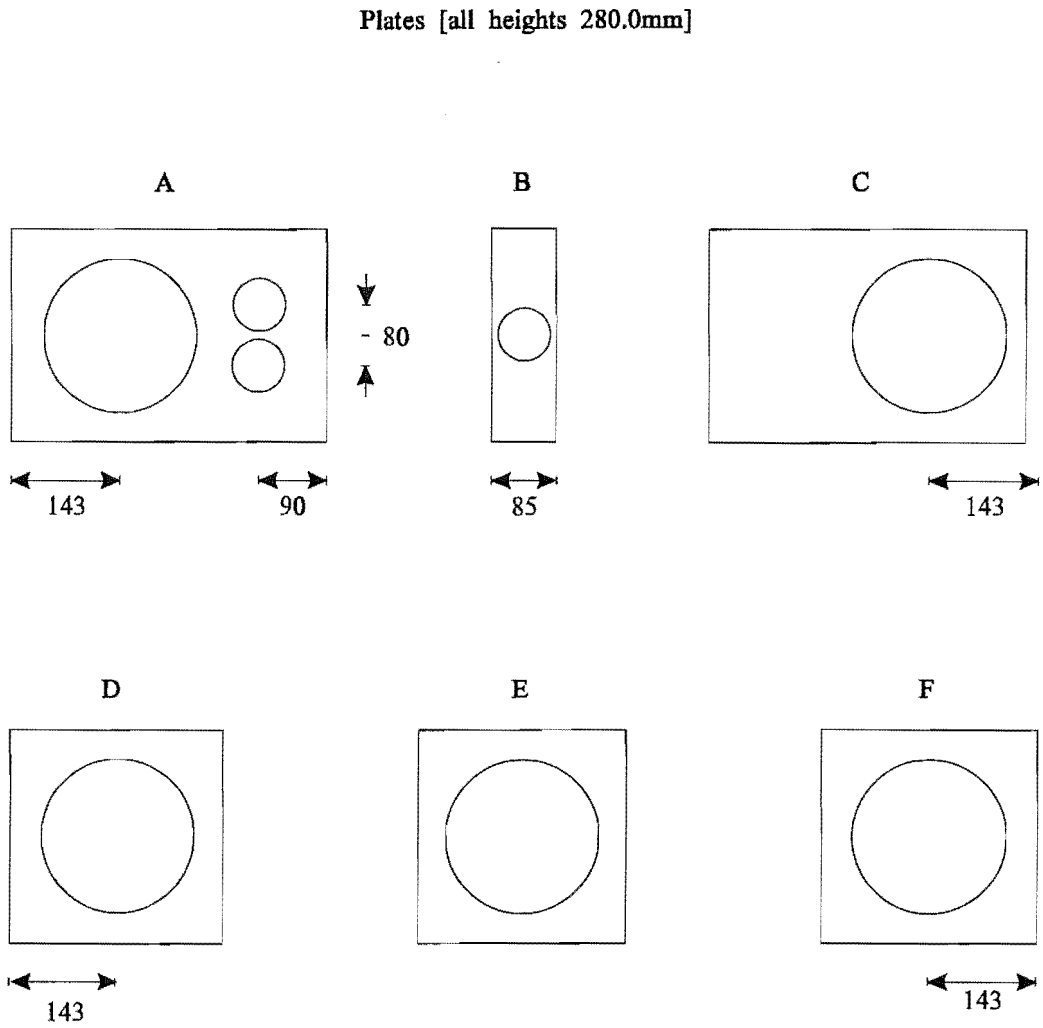

Figure 3.3.3b: Diagram of each of the side plate for the scattering chamber as labelled in Figure 3.3.3a with appropriate dimensions to the 8 inch or the 2.75 inch conflat seals.

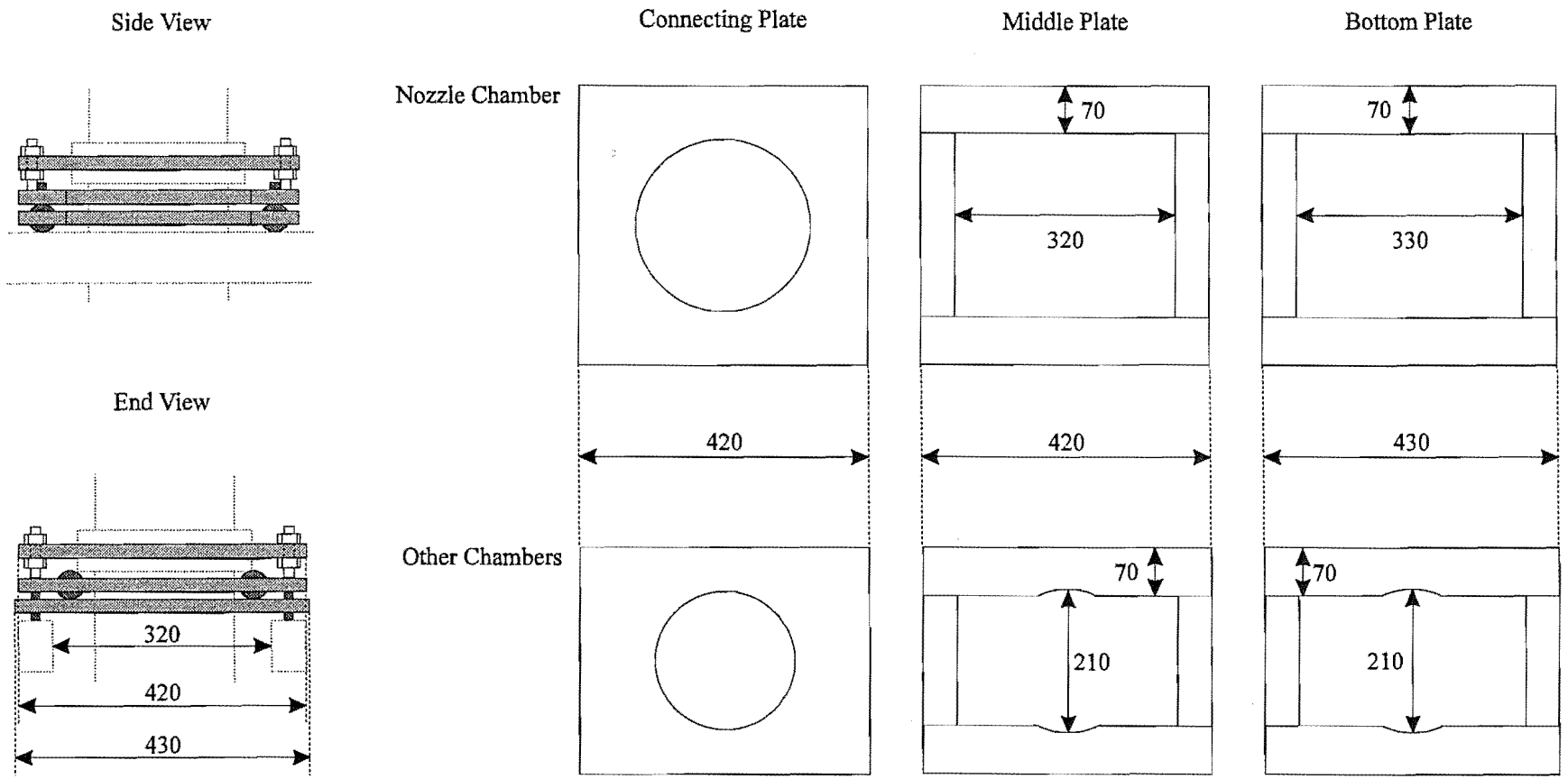

Figure 3.3.4: Three dimensional chamber mounts for the nozzle, buffer, hexapole 1 and hexapole 2 chambers. The bottom plate travels along the rails, the middle plate travels on the bottom plate perpendicular to the rails and the connecting plate provides the vertical motion. The nozzle chamber mount is larger as it requires a 10 inch conflat seal for the six-way cross. The clearance holes for the thredded studs are not shown in the connecting plate.

the cryogenic pumping of the system. Apart from the nozzle chamber each chamber had a doughnut liquid nitrogen trap directly above the diffusion pumps to trap oil vapour condensing onto the surfaces within the vacuum system. The nozzle chamber had a cylindrical liquid nitrogen trap above the chamber with a louvered plate made of copper suspended from the trap and located inside the lower port arm. The liquid nitrogen traps for the nozzle chamber were installed after substantial oil condensation had been observed within the nozzle chamber over the first month of operation. Additional liquid nitrogen traps were a half cylinder trap above the hexapole rods, a doughnut trap on one of the side arms of the hexapole 2 chamber and a cold finger trap with a copper plate attached to the bottom located in the scattering chamber which extended over the scattering volume. The liquid nitrogen traps were connected by 0.375 inch copper tubing and swagelok connectors and were fed from a 75 litre liquid nitrogen dewar (a rotation of four dewars was used) which was pressured by a cylinder of dry nitrogen.

Each of the forelines between the diffusion pumps and their associated mechanical pumps were re-built. All seals were either Alcatel NW25 or NW40 o-ring clamp seals or 2.75 inch copper conflat seals. The forelines were 1.5 inch or 2.0 inch stainless steel bellows which provided the required flexibility for correct alignment of diffusion pump and mechanical pump and provided vibration damping between the mechanical pumps and the frame. Each foreline had a valve to seal the mechanical pump from the diffusion pump, a vent valve and a thermocouple gauge head (MKS TC-1A, Duniway DST-531, Varian 0531) which was constantly monitored (MKS type 286 controller). There were three diffusion pump bypass forelines and valves for the initial pumping of the chambers, from atmosphere, one situated on the nozzle chamber, a second on the hexapole 1 chamber and the third on the scattering chamber.

The pressure in each of the chambers was monitored by ion gauge (Duniway T-100-K) and type 290 controllers. Typically (after appropriate pump down) the pressures in the nozzle, buffer, hexapole 1 and scattering chambers would be $9x10^{-8}$, $5x10^{-8}$, $9x10^{-8}$ and $4x10^{-8}$ torr with the nozzle off and $1x10^{-5}$, $5x10^{-6}$, $5x10^{-7}$ and $1x10^{-7}$ torr with the nozzle in operation.

The protection for stage III was connected to the setpoint relays on the controllers for one ion gauge and all of the foreline thermocouples. If the ion gauge relay went high then power to the pressure-sensitive electrical components such as the Amptektron particle detector, quadrupole mass spectrometer and hexapole rods, would be turned off. If the foreline setpoints went high then only that particular diffusion pump would be shut down. Additional thermocouples monitored the temperature of each of the diffusion pump bodies and were set to turn off all diffusion pumps if one thermocouple went high indicating a water cooling failure. Each of the thermocouple protection features automatically restarted the diffusion pumps once the relay had returned to low status. As with stage I and stage II the protection facility on the ion gauge could be bypassed while an experiment was being performed.

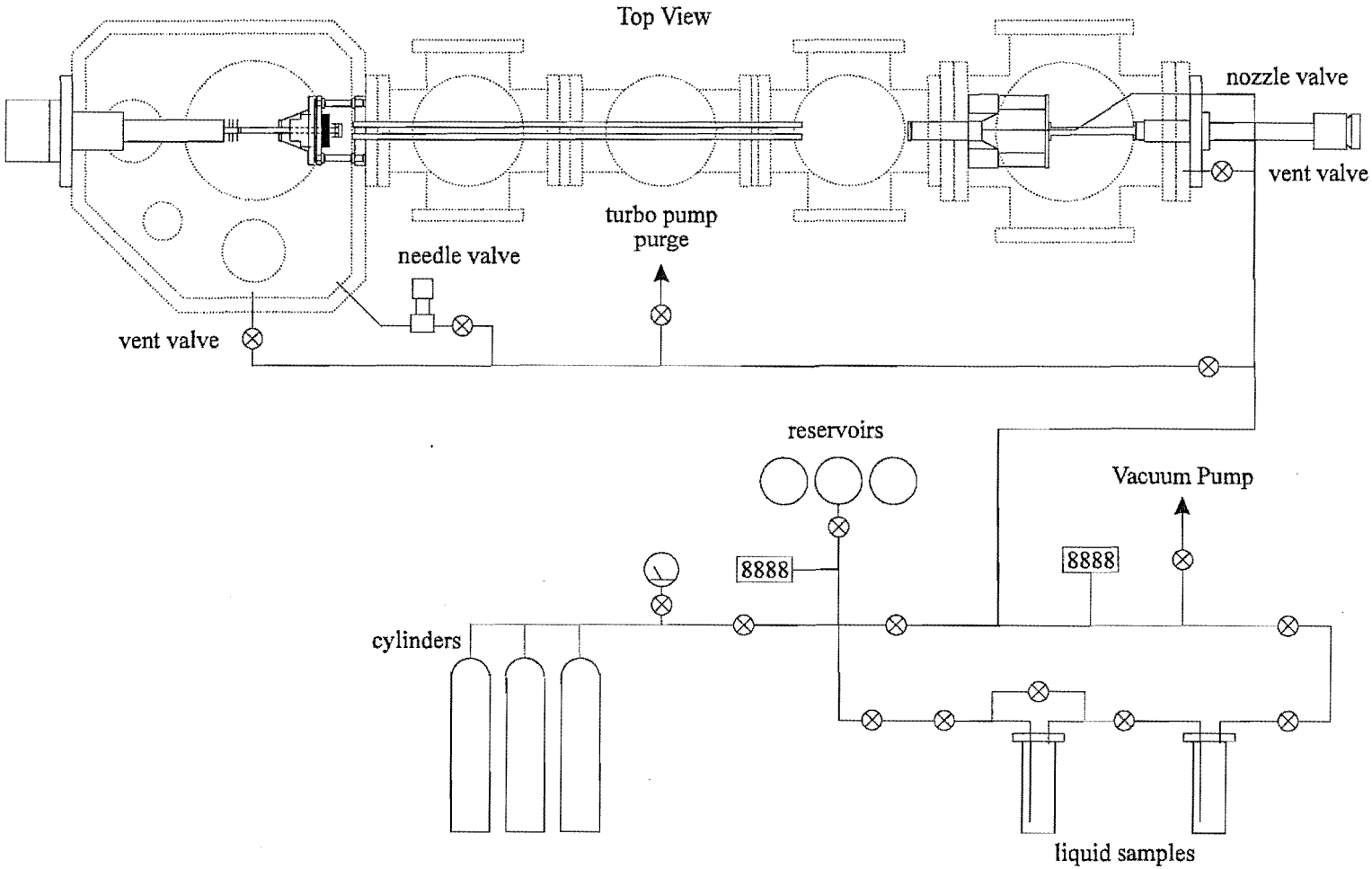

Figure 3.3.5: Gas handling line for stage III. The gas handling line could admit samples from cylinders, previously made mixtures from reservoirs or from liquid vapour pressures. At different times the single line to the nozzle provides the beam species, bleed gas into the scattering chamber, venting of the machine and the gas purge for the turbo molecular pump. Shown are the pressure monitors of two baratrons and one needle gauge.

3.3.3 Gas Handling

Most of the gas handling assembly was moved away from the machine to provide greater accessibility to the vacuum chambers. The gas line is shown schematically in Figure 3.3.5. It was mostly 0.25 inch stainless steel tubing with swagelok fittings with a section of 0.25 inch copper tubing from the cylinders to the first valve. The gas line served several functions: admission of samples directly from commercial cylinders, from previously prepared gas mixtures in storage containers and directly from a liquid vapour pressure. These various lines combined into one line to pass across to the machine. On the machine side the line was divided to the nozzle via a section of stainless steel bellows, a bleed valve into the scattering chamber and two vent valves on the nozzle chamber and scattering chamber. The gas line had three pressure measuring devices at different stages throughout the line and was pumped by an Edwards Speedivac ES-100 (100 $lmin^{-1}$) mechanical pump.

3.3.4 Nozzle Assembly

The nozzle chamber was upgraded from the Varian six inch chamber to the Varian eight inch chamber which required an extension of the nozzle carriage assembly. Two extensions were necessary: a 160 mm aluminium extension between the bellows of the linear driver and the carriage and a 101 mm hollow aluminium extension between the carriage and the pulsed electromagnetic valve or nozzle (Figure 3.3.6). All other components of the nozzle are identical to stage II.

The nozzle assembly flange was mounted on a trolley mount similar to those described in Section 3.3.2 for the vacuum chambers (refer Figure 3.3.6). The trolley mount and the 0.25 inch stainless steel bellows, from the flange gas feedthrough fitting to the gas line, allowed the nozzle assembly to be removed in one piece for easy repair or replacement of the nozzle components.

3.3.5 Alignment Rods

The larger nozzle chamber and the inclusion of a buffer chamber combined to increase the distance between the hexapole and the nozzle carriage assembly. This required a modification of the alignment rods to a system of two pairs of 10 mm diameter alignment rods the ends of one set machined down to fit into holes drilled into the second set. The rods were collinear to maintain correct alignment of the nozzle, skimmers and hexapole (Figure 3.3.7).

The original skimmer assembly flange, of stage II, was positioned between the buffer and hexapole 1 chambers and carried one set of alignment rods. The ten inch to eight inch converter flange, between the nozzle and buffer chambers, supported the second set of alignment rods. Both sets of rods were held in position by two bushells on each flange and two grub screws. The first set of rods were 450 mm in length and extended 330 mm into the nozzle chamber where the nozzle carriage assembly was mounted on the rods and translated through linear bearings. The second set of rods of length 292 mm linked with the first set of rods within the buffer chamber and extended a

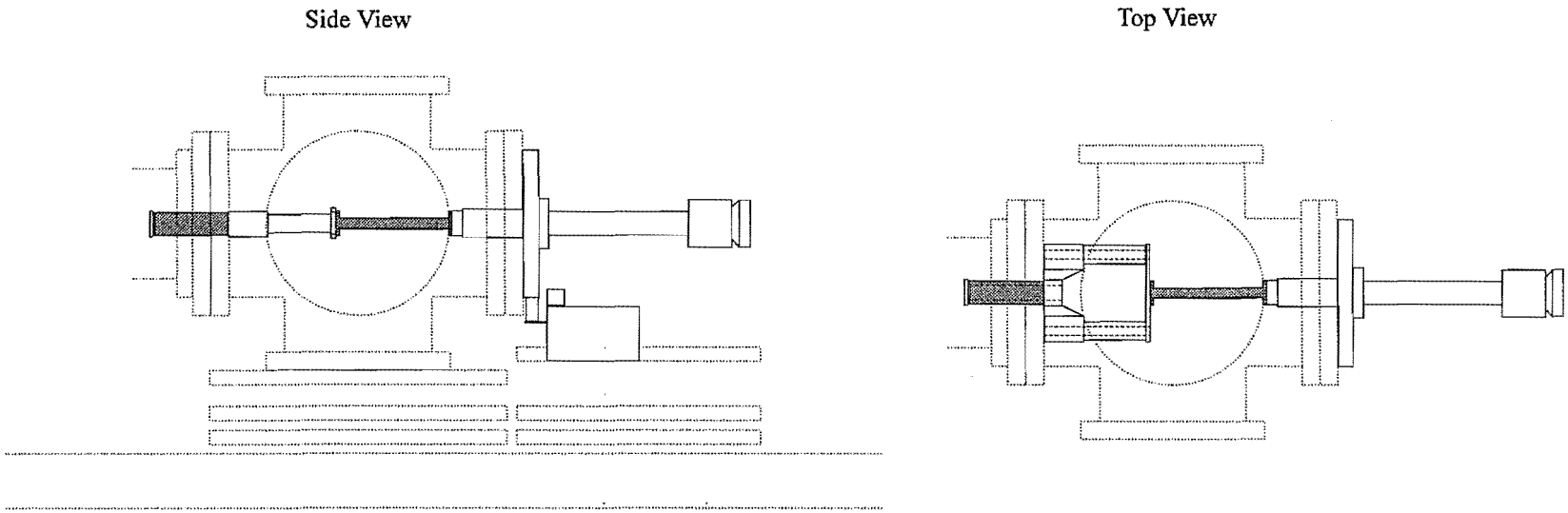

Figure 3.3.6: The required extensions (shaded) to the nozzle carriage assembly. The nozzle flange is mounted onto an xyz mount, similar to the chamber mounts, and held by a single bolt beneath the flange.

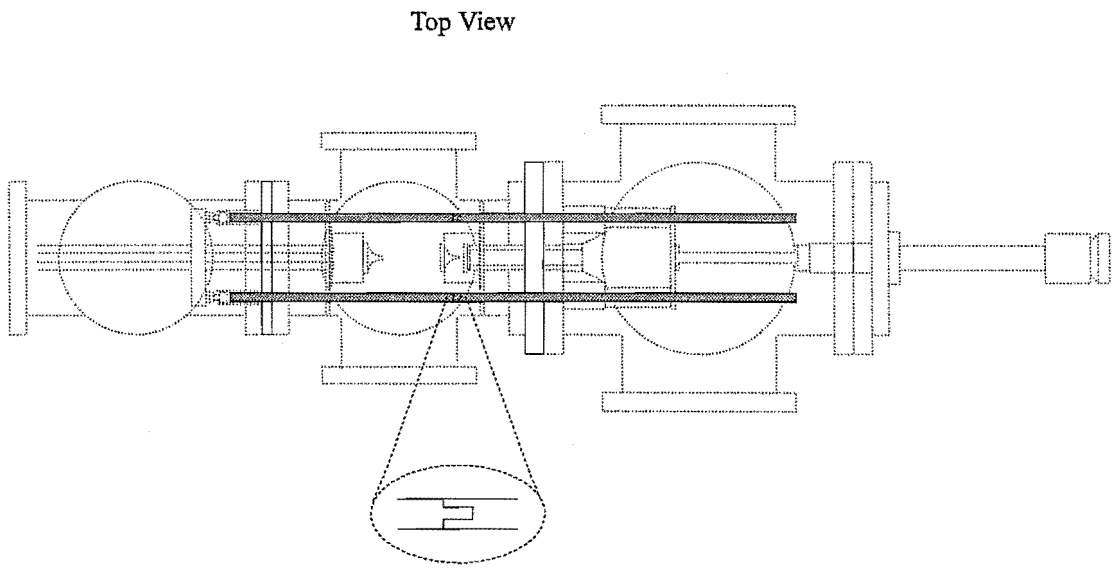

Figure 3.3.7: System of two sets of alignment rods (shaded) for correct alignment of the nozzle, skimmers and hexapole. The rods are held in each flange by bushells and grub screws (not shown) on the side of the flange. The two rods are butted together inside the buffer chamber.

further 41 mm into the hexapole 1 chamber for mounting of the fixed hexapole support.

3.3.6 Skimmer Flanges

Stage III has two skimmers aligned on either side of the buffer chamber. They are both mounted on moveable flanges which travel on the alignment rods. The diameter of the skimmer support flanges are ~1 mm less than the internal diameter of the six inch cross arms. The narrowness of the gap around the skimmer flanges allows for differential pumping between the nozzle, buffer and hexapole 1 chambers.

The first skimmer was a Beam Dynamics 1.0 mm diameter skimmer and was mounted on the internal side of a top hat welded into the skimmer support flange (Figure 3.3.8). The second skimmer was an aluminium skimmer, machined in the Chemistry Department, with a 2.0 mm diameter aperture which was subsequently widened to 3.2 mm diameter to increase signal intensity. The shape of the second skimmer was not as important as the first skimmer since no shock wave structure from the nozzle expansion is present to degrade the beam. The skimmers were centred on the skimmer flange by lathe, fixed in position and then cleaned to maintain as accurate alignment as possible. The alignment rods and skimmer flanges were installed together.

The first skimmer was positioned so that at maximum extension the face of the nozzle would be 2-3 mm from the end of the skimmer. The second skimmer was positioned so that the hexapole rods partially entered the skimmer top hat. The distance from the first skimmer to the second skimmer was 110 mm and from the second skimmer to the hexapole rods 58 mm.

3.3.7 Hexapole

With the skimmers now on moveable flanges it was possible to re-position the hexapole in the fixed and floating supports to facilitate an extension of the orienting field plates (Section 3.3.8). The hexapole was moved 102 mm along the supports towards the nozzle chamber. The fixed and floating supports remained in their original positions as with stage II. The end of the hexapole was positioned 2 mm from the inside surface of the scattering chamber (Figure 3.3.9).

During the course of stage III the hexapole mounts were altered from an inscribed radius of 7.25 mm to an inscribed radius of 6.0 mm which corresponded to a 1.0 mm separation between adjacent rods. The new hexapole mounts had the same design as those in Figure 3.2.2 but were machined from glass ceramic instead of perspex to reduce the amount of outgassing from the mounts.

3.3.8 Homogeneous Field Plates

The homogeneous field plates or orienting field plates are shown in Figure 3.3.10. From the hexapole floating support two stainless steel posts extend on which a perspex disc is mounted, 60 mm into the scattering chamber (Figure 3.3.10). A second perspex disc arrangement fits onto the first perspex disc, with a threaded sleeve extending through the first disc and a threaded perspex ring clamping the two discs

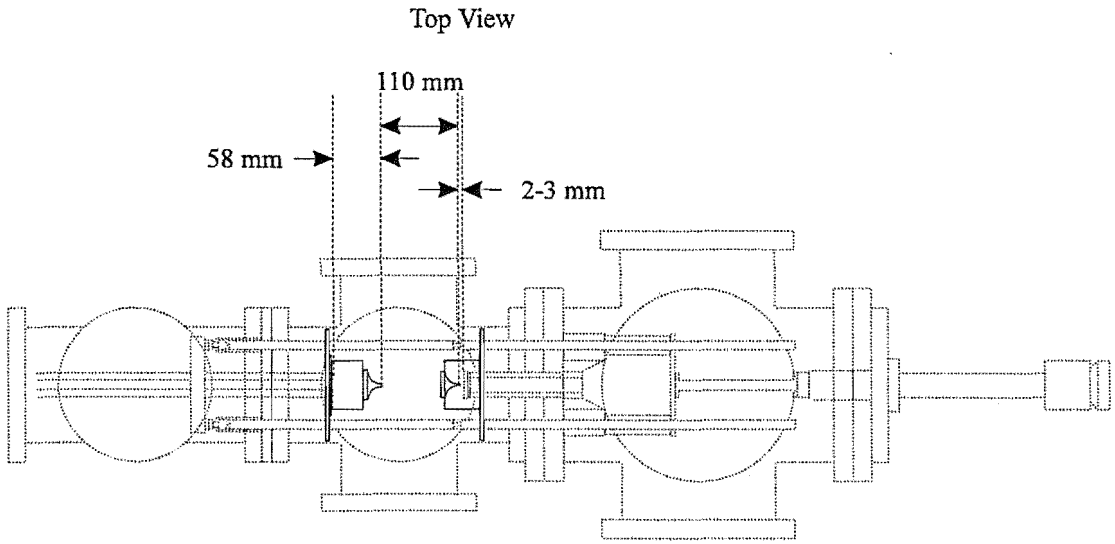

Figure 3.3.8: Positioning of the two skimmers within the buffer chamber. Each skimmer can travel along the alignment rods for correct positioning. Each skimmer is positioned on a top hat such that the skimmer flange can be positioned within the six-way cross arms for differential pumping. The distances shown are from the nozzle (at maximum extension) to the first skimmer, first skimmer to the second skimmer and second skimmer to the front face of the hexapole assembly.

Top View

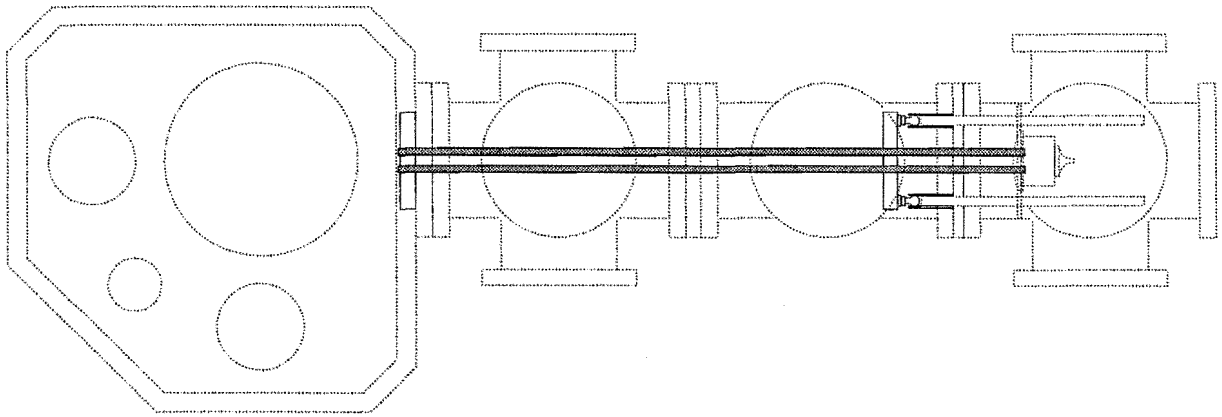

Figure 3.3.9: Diagram indicating the new position of the hexapole rods on the hexapole supports. The fixed and floating supports are similar to those of Figure 3.2.2.

together (Figure 3.3.10). The homogeneous field plates are fixed to the second perspex disc and extend from the hexapole, through the middle of the two perspex discs and through the scattering centre. An 8 mm diameter hexapole exit aperture is positioned 10 mm from the end of the hexapole rods. The homogeneous field plates were held 10 mm apart by ceramic spacers and extended 160 mm to the cross beam axis with a total length of 186 mm. Two 10 mm diameter holes were drilled through the homogeneous field plates for the cross beam.

Figure 3.3.10 shows the final design for the homogeneous field plates. In the original design the plates were 129 mm long with a 40 mm separation. With the re-positioning of the hexapole rods the plates were lengthened to 186 mm. The plate separation was progressively reduced from 40 mm to 20 mm to 10 mm to reduce the voltage required on the plates for a given electric field strength and for better definition of the scattering volume. Initially, 95% transmitting gold mesh clamped between frames were used as homogeneous field plates to reduce electron scattering. However, problems with electrical connections and cleaning of the fragile structure resulted in their demise and replacement by stainless steel plates coated in aquadag (colloidal graphite) to minimise electron scattering from the surfaces.

The second perspex disc was completely electrically shielded from the scattering chamber by a shaped grounded aluminium shim with strips of shim across the top and bottom of the homogeneous plates from the perspex disc to the detector end of the field plates. At the exit of the hexapole was a grounded aluminium mesh to prevent the hexapole high voltage from penetrating into the weak field maintained by the homogeneous field plates. In the absence of the hexapole shielding it was found that the high voltage from the hexapole affected the electron current measured at the electron collector. Above the plates was a copper plate secured to a liquid nitrogen trap for cryogenic pumping of the scattering volume. The full scattering volume arrangement is shown in Figure 3.3.15.

3.3.9 Electron Gun

The electron gun was a custom designed near-monochromatic device based on a Pierce element as shown in Figure 3.3.11. The elements were gold plated phosphor bronze and were mounted on four studs attached to a stainless steel shaft which was welded to a 2.75 inch conflat flange mounted on a Huntington xyz translator. The xyz translator could move the electron gun up to 25 mm off axis in the x and y directions and 50 mm in the z direction (collinear with the shaft).

The electron gun was mounted on an eight inch conflat flange (side A of Figure 3.3.2) perpendicular to the pulsed supersonic beam axis. The eight inch conflat and the 4.5 inch conflat of the xyz translator were joined by a conversion flange. The conversion flange had a 4.5 inch open internal top hat that extended 130 mm into the scattering chamber. Surrounding the top hat was another top hat, of slightly larger diameter, that could be manually extended up to the near homogeneous field plate. The electron beam was collimated by a 5 mm diameter, 15 mm long snout on the end of the larger top hat before passing through the homogeneous field region (see Figure 3.3.15). Typical

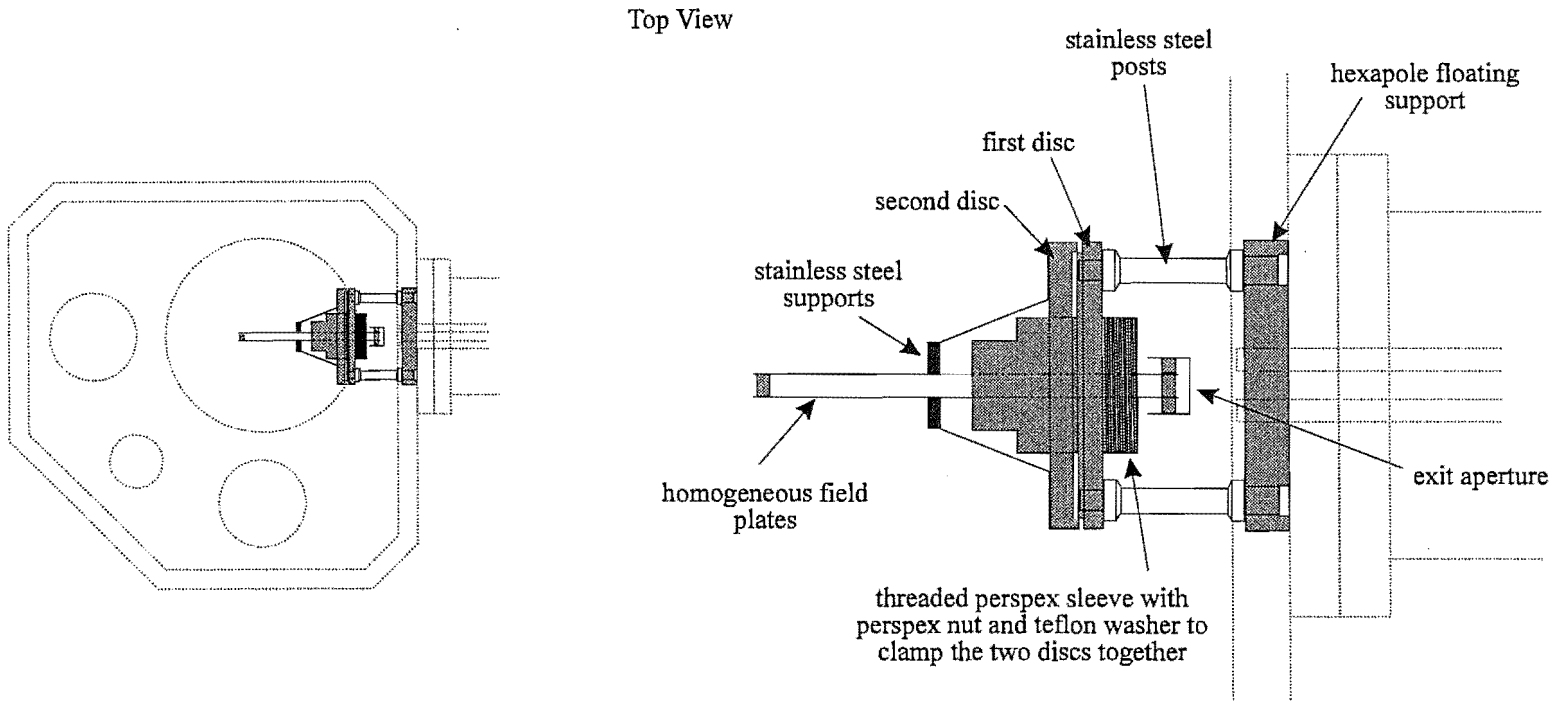

Figure 3.3.10: The alteration of the hexapole rod position allowed extension of the homogeneous field plates. The perspex mount is shown with the homogeneous field plates extending through the mount, towards the hexapole, and terminating at the exit aperture.

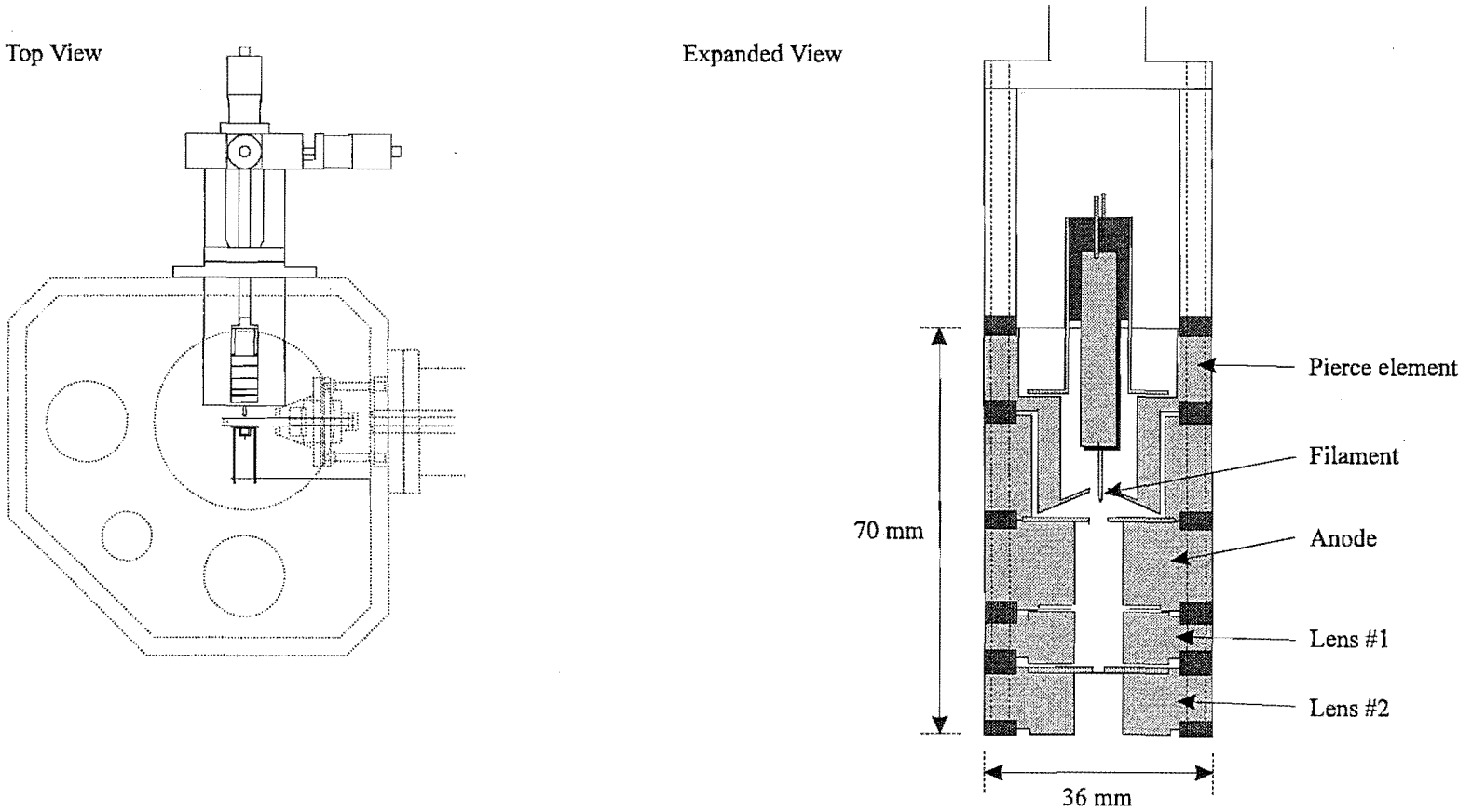

Figure 3.3.11: The position of the electron gun with respect to the homogeneous field plates and electron collector. The electron gun is mounted on a xyz translator within an internal top hat. The expanded view of the electron gun shows the individual electron gun elements and the insulating ceramic spacers. The elements are held together by four studs which extend the length of the gun. The filament was 0.007 inch rhenium wire coated with $BaZrCO_3$.

operating voltages for each of the elements is shown in Table 3.3.1 for an electron energy of 200 eV.

Lens	Voltage
Cathode	-200
Pierce	-174
Anode	105
Lens #1	-135
Lens #2	171

Table 3.3.1: Typical element voltages for an electron energy of 200 eV (see Figure 3.3.11).

Directly opposite the electron gun was the electron collector. The electron collector had various designs but for the most part involved a simple plate or cup. Shown in Figure 3.3.15 was the latest design of a cup which was electrically isolated from its surrounding grounded plate. The electron collector was mounted on a bracket from the wall of the scattering chamber and was situated 5 mm beyond the far homogeneous field plate from the electron gun.

3.3.10 Detectors

Two different detectors were employed through the course of researching the asymmetry of electron impact on spatially oriented molecules: a Vacuum Generators SXP-300 quadrupole mass spectrometer and a commercial Amptektron model MD-501L thermal ion detector.

3.3.10.1 Quadrupole Mass Spectrometer

The quadrupole mass spectrometer was mounted directly from an eight inch flange, on axis with the pulsed supersonic beam, as in stage II and as shown in Figure 3.3.12. The quadrupole mass spectrometer was used in two different modes: as an ion mass analyser with its own ion source or as a quadrupole filter with the ion source removed.

When the Amptektron particle detector was being used the quadrupole mass spectrometer retained its own ion source but was mounted further back from the scattering volume on a top hat. In this mode the quadrupole mass spectrometer was used to determine arrival time distributions as described for stage II (Section 3.2.6) and as a diagnostic tool to determine whether the pulsed nozzle was operating correctly.

For measurements of electron impact asymmetry the quadrupole mass spectrometer was used solely as a mass filter/detector with the ion source being removed and replaced by an ion lens assembly. The ion lens assembly (Figure 3.3.12) came to

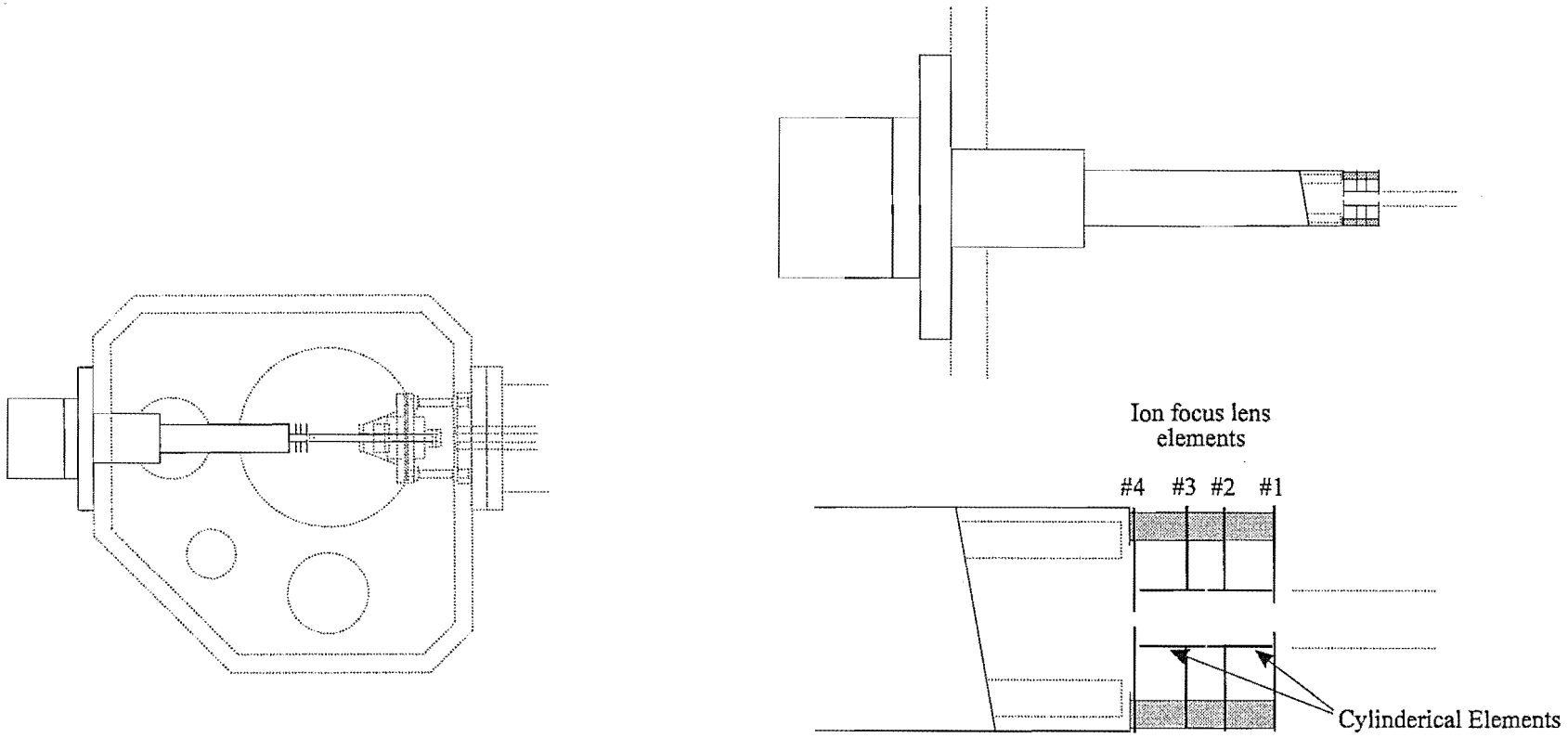

Figure 3.3.12: The quadrupole mass spectrometer arrangement when used as a mass filter/detector (ion source removed). The four lens elements extend to near the homogeneous field plates. The four lens elements consist of a front plate, two cylinderical elements and a final plate before entering the quadrupole (see Figure 3.3.13).

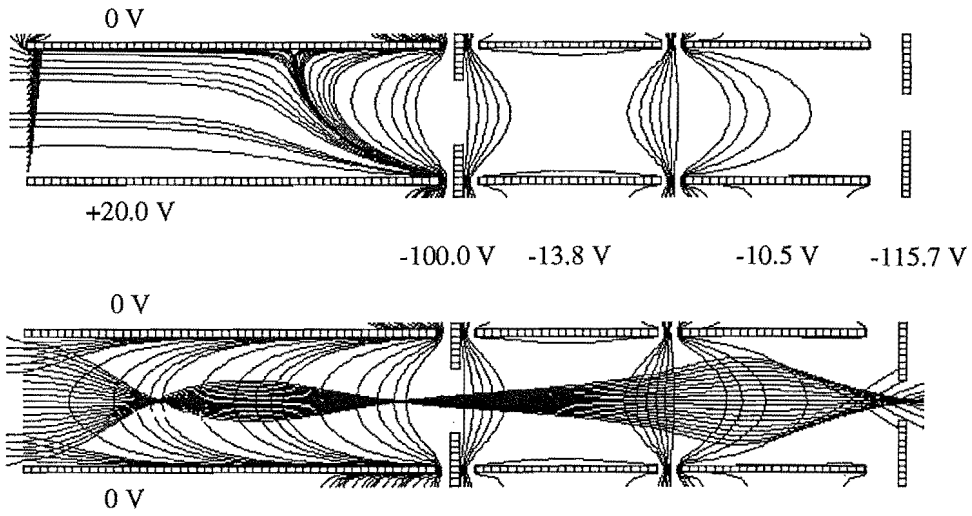

Figure 3.3.13: Simulated ion trajectories and electric field potentials for the quadrupole mass spectrometer ion lens arrangement. At left of the diagrams is the scattering volume (where ions would be formed). In the top diagram one homogeneous field plate is at 20 V and in the bottom diagram this has been switched to ground potential.

within 1.0 mm of the end of the homogeneous field plates. The ion lens plates were continuously on with the front element (nearest the homogeneous field plates) fixed at -100 V and the other three elements adjusted for maximum ion counts. The voltage on the front plate of the ion lens assembly did not disrupt the parallel orienting field while the plates were high but did attract the ions into the quadrupole mass filter once the plates had switched to ground. This is shown in Figure 3.3.13 as mathematically modelled for ion trajectories with and without an orienting electric field using a commercial package (Simion v3.1).

3.3.10.2 Amptektron Particle Detector

The Amptektron model MD-501L thermal ion detector was a fully enclosed self contained particle detector with no mass resolution. It required a stable +7-30 VDC input to provide voltages to the electron multiplier cone and the amplifiers. The output was a +5 V, negative going, 220 ns wide pulse for each ion incident on the multiplier cone which was suitable for direct pulse counting.

Two additional collimators were mounted to the case of the unit for ion focusing and to control the electric field penetration from the electron multiplier into the scattering volume (Figure 3.3.14). The outside element was grounded to the case and was located 9.0 mm beyond the end of the homogeneous field plates. The inside collimator was floatable, although, for all of the results discussed in Chapter 5, it was

fixed at ground potential. The Amptektron was mounted from the shaft of a stepping motor and could be moved out of the molecular beam path to allow the on-axis quadrupole mass spectrometer to detect the pulsed supersonic beam.

Although the design of the Amptektron was theoretically appealing there were problems encountered. Initially, the Amptektron came with a -300 V cone voltage on the electron multiplier. It was found that this was insufficient to attract and detect the ions from the molecular beam so it was returned to the factory and modified to -3000 V. During the period of operation through stage II and the beginning of stage III a series of problems occurred with the main amplifier (A101A) chip and the electron multiplier. This resulted in several return trips of the Amptektron unit and components between the factory and laboratory. After a period of uncertainty the final problem was found to be that the output line was adding a high capacitive load to the output driver, which was sent into oscillation which appeared as failure of the A101A chip in the diagnostic tests. The changing of the twisted-pair output cable to single core wire seemed to solve the problem. A further problem continuously encountered with the Amptektron was its inability to detect the molecular ions formed from heavy molecular species in the pulsed supersonic beam. For beam species CH_3Cl and Ar the measured beam flux was adequate, but for species such as CF_3Br, $CHCl_3$ and CH_3Br the measured beam flux was very small or absent. It was assumed to be due to a momentum dependent effect on the efficiency of the electron multiplier.

3.3.11 Scattering Volume

It was found that the scattering volume, and the associated region around the scattering volume, was the most sensitive component determining the success of the cross-beam experiments.

The final scattering volume configuration is shown in Figure 3.3.15 from different angles with the ion lens configuration on the quadrupole mass spectrometer of Figure 3.3.12. The homogeneous field plates were 10 mm apart with the electron beam crossing a 16 mm region from the end of the electron gun snout to the electron collector. There was grounded aluminium shims directly above and below the homogeneous field plates screening the scattering volume and a liquid nitrogen trap plate above the top shim. All of the surfaces directly facing the scattering volume were painted with aquadag which minimised ion or electron scattering from the surfaces. It was endeavoured to keep the homogeneous field plates and shields clean in order to preclude the build-up of electric charges on their surfaces from oil films. Periodically the homogeneous field plates and surroundings were removed, cleaned, re-coated with aquadag and reinstalled.

All electrical connections to the homogeneous field plates, mesh, electron collector and ion lens elements were single core silver wire, sheathed in a resin free fibre glass sleeving to prevent the wires shorting to each other or the chamber, and connected by stainless steel electrical (choc-bloc) connectors or male/female clasps.

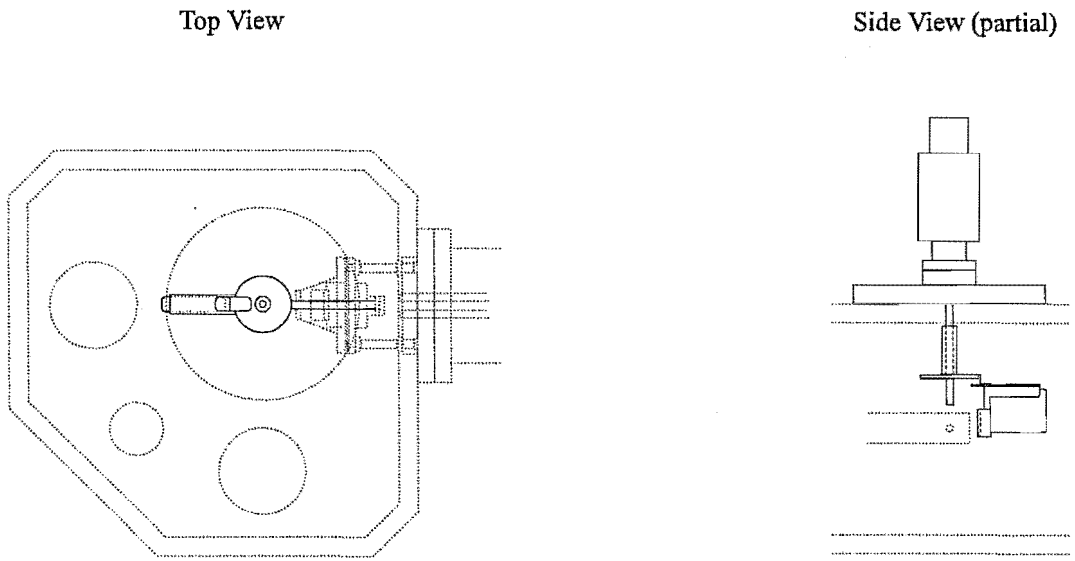

Figure 3.3.14: Amptektron MD-501L thermal ion detector mounted on the stepping motor. The position of the Amptektron allows it to be stepped out of line of the molecular beam for detection by an on-axis detector.

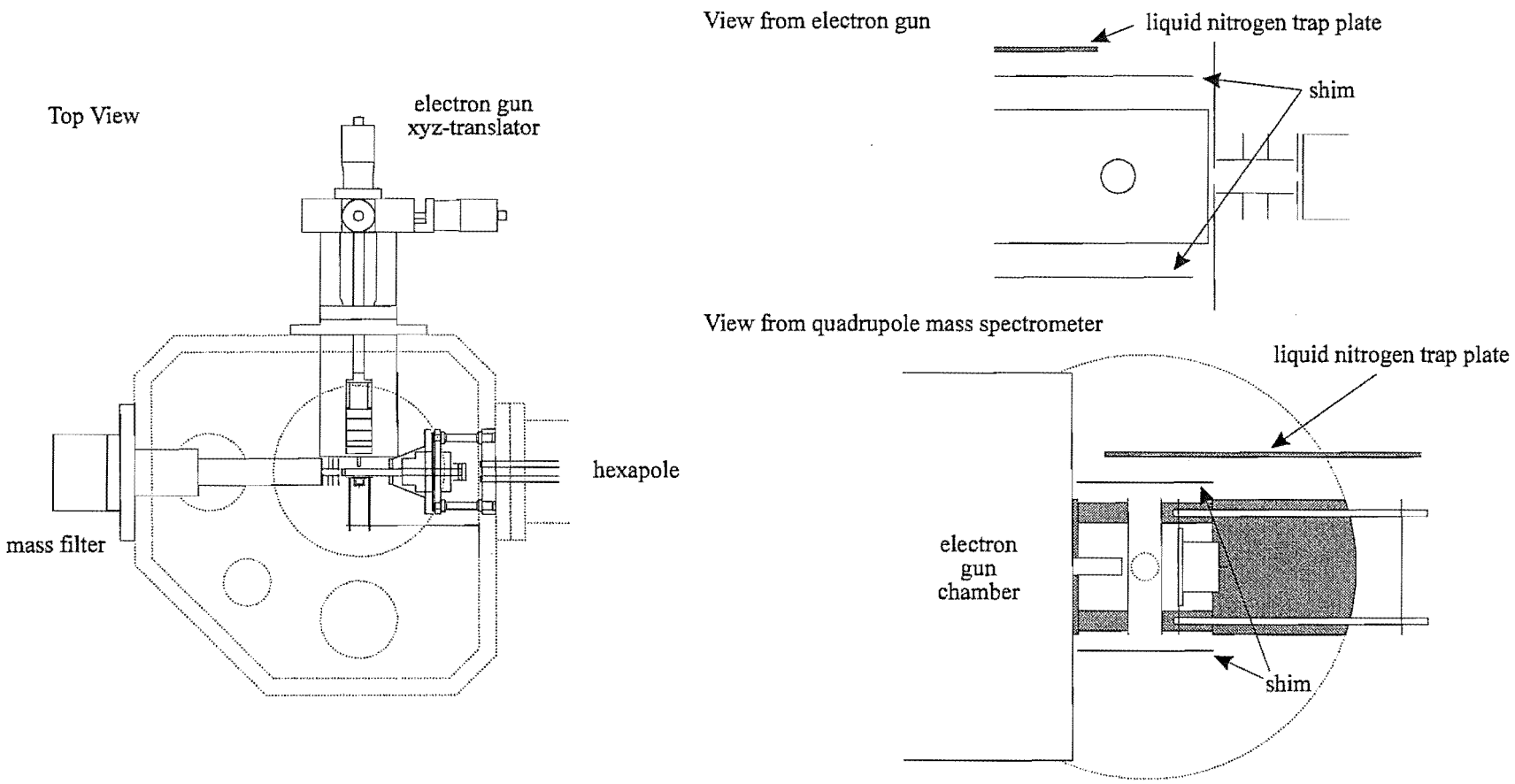

Figure 3.3.15: Views of the full scattering volume when the quadrupole mass spectrometer was the detector. The two views from the electron gun and quadrupole mass spectrometer show the grounded stainless shim, above and below the scattering volume, and the liquid nitrogen trap plate above the top shim. Also shown are the homogeneous field plates, electron gun top hat and snout, electron collector and lens elements from the quadrupole mass spectrometer.

3.3.12 Electronics

The beam source driver unit and the computer control of the hexapole high voltages were the same as in stage II Section 3.2.7. The new components considered here are the homogeneous field pulsing unit and the stepping motor controller used for the positioning of the Amptektron particle detector.

3.3.12.1 Homogeneous Field Pulsing Unit

The homogeneous field pulsing unit (Figures 3.3.16a, 3.3.16b and 3.3.16c) was a custom designed unit triggered from the pulse counting controller. It controlled the voltage amplitude, the delay time for field switching (on or off) and the time that the plates remained close to ground potential. In an experiment it was necessary to set the energised homogeneous field plate at an elevated potential with respect to the second field plate at ground potential when the pulse of gas arrived in order to physically orient the molecules. However, there must be no electric field present when the pulse of gas is ionised as the ions would follow the field and be lost to the detector (refer Figure 3.3.13). So, the energised homogeneous field plate was switched to near-ground potential after a set delay, remained at near-ground potential until both pulse counting gates have pulsed on and off and then returned to the original potential to repeat the process for the next gas pulse (see Figure 5.1.1).

The homogeneous field pulsing unit is triggered by the pulse counting unit which provides the time zero reference. The output from the homogeneous field pulsing unit could be monitored by a representative monitor pulse on an oscilloscope. The delay for the voltage drop, from the set voltage to ground, could be varied from 0.1 ms to 9.8 ms using a single turn potentiometer. The setting of this delay is an important feature of the experiment and is described more fully in Section 5.1.1. The width of the grounded portion is variable by another single turn potentiometer from 0.2 ms to 9.8 ms. The potential of the homogeneous field plates could be varied between 6.5 V and 100 V by a ten turn potentiometer. The homogeneous field pulsing unit had three independent positive pulse supplies and three independent negative pulse supplies.

The switching time from the high plate potential to <0.1 V occurred in <0.1 μs. It was important for the minimum potential to be close to ground potential and of the same polarity to preclude field inversion and possible orientation switching. Hence, an offset bias unit could be used to vary the low potential of the homogeneous field pulsing unit by between ±0.28 V to ±0.68 V in order to fine tune the low potential reference level.

3.3.12.2 Stepping Motor

When the Amptektron was used as the detector it was mounted on a stepping motor which could rotate the Amptektron about the scattering volume centre. The stepping motor was a Slo-Syn (model M061-CF-408), 200 steps per revolution, high vacuum stepping motor which received its pulses from a STD-206 crystalap motor. The motor was connected to a commercial 16-bit stepping motor card (PCL-838) in the

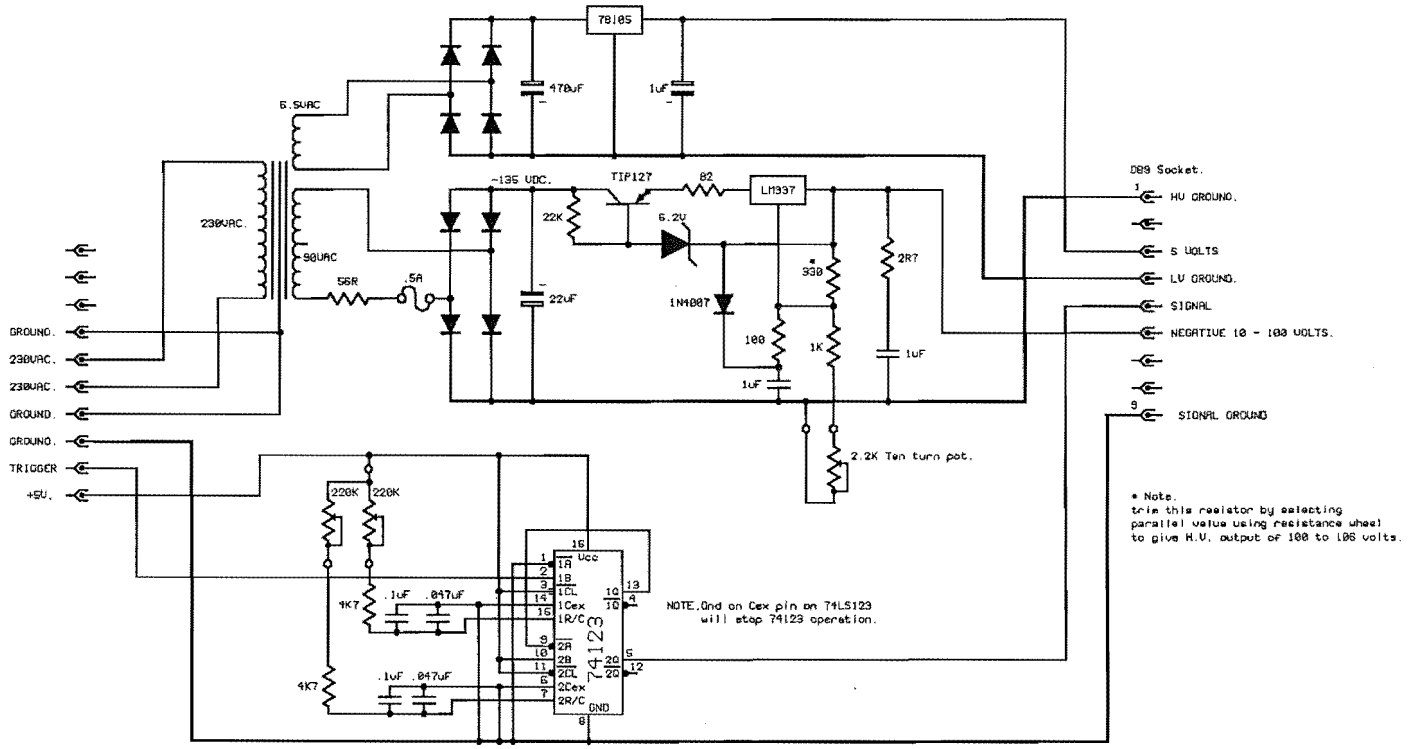

Figure 3.3.16a: Modular control unit for the switching of the homogeneous electric field potential. Each modular control unit (there are six in total) has a variable delay, width and amplitude for the potential pulse (see text) which is then supplied to the appropriate driver units (either positive or negative, see Figure 3.4.16b and Figure 3.4.16c).

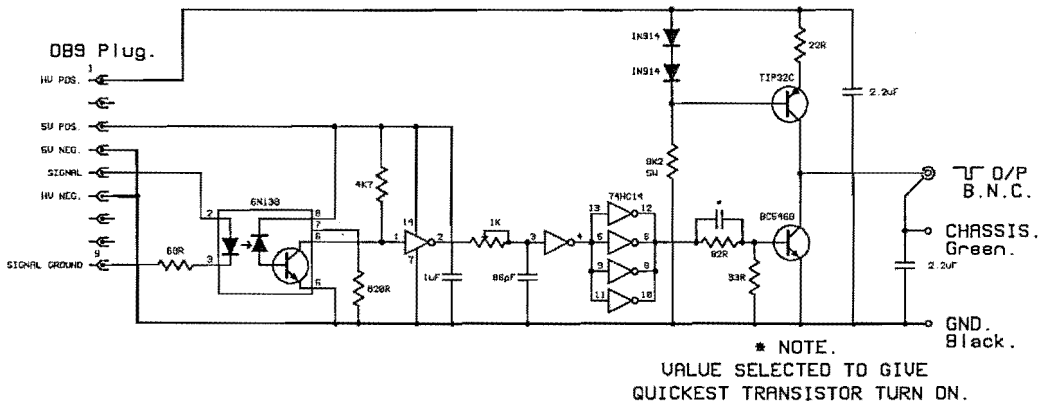

Figure 3.3.16b: Modular control driver unit for a positive potential switching on the homogeneous electric field plates.

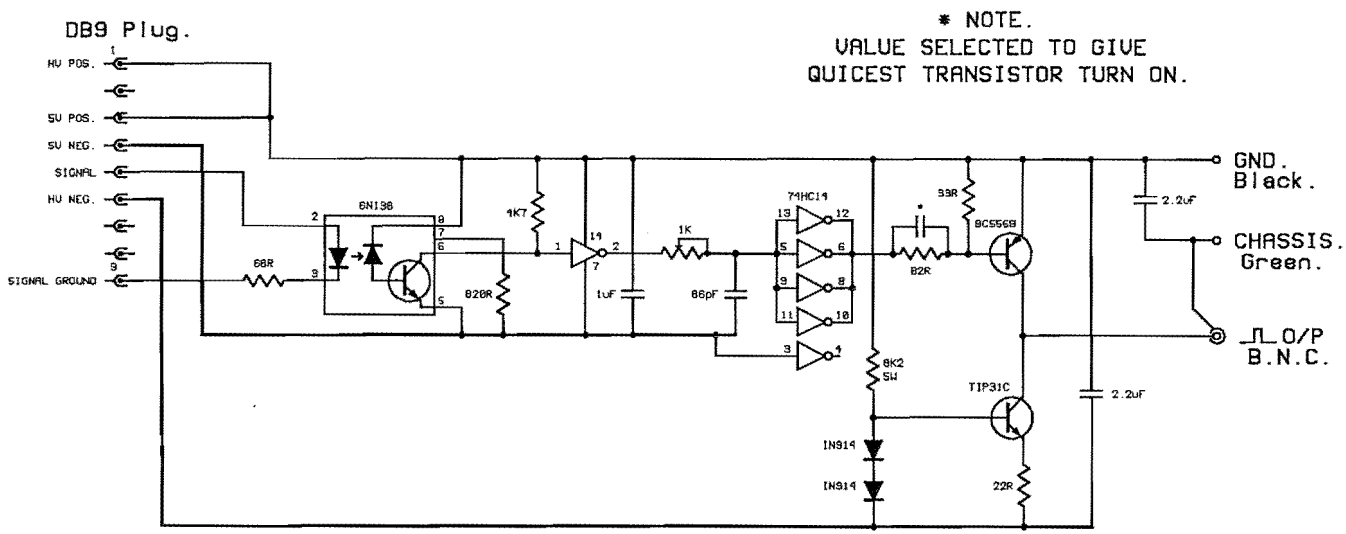

Figure 3.3.16c: Modular control driver unit for a negtive potential switching on the homogeneous electric field plates.

microcomputer (for stage III the computer had been upgraded to a 25 MHz 486sx). The control of the stepping motor was from custom written software which enabled single or multiple steps left or right of the beam axis.

3.3.13 Characterisation of Stage III

Characterisation of stage III and the new hexapole mounts were completed as described for stage II in Section 3.2.6. Arrival time distributions for symmetric top molecules were measured at various hexapole voltages as in stage II. From the arrival time distributions the gate 1 position for pulse counting could be determined. To fine tune the optimum gate 1 position, a beam arrival time profile was measured by stepping the gate 1 delay and recording the signal (gate 2 remains fixed). The measurement of an arrival time profile was required since the quadrupole mass spectrometer and Amptektron particle detector were in different spatial positions. An arrival time distribution and arrival time profile are shown for CH_3Cl in Figure 3.3.17. Once the position of gate 1 was optimised then the homogeneous field pulsing unit delay could be accurately set as described in Section 5.1.1.

Many of the components involved in the experiments to measure the asymmetry of electron impact ionisation could be independently controlled. For a successful experiment each component had to be correctly aligned and optimised. The alignment of skimmers, hexapole, electron gun and detectors was verified by He-Ne laser during the assembly of the components. The optimisation of nozzle-skimmer distance, electron gun position (using the xyz translator) and detector position, when the Amptektron was used, were performed *in situ* under experimental conditions.

The changes made to the nozzle chamber from stage II to stage III required the optimisation of the nozzle-skimmer distance for the best beam expansion conditions as described in Section 2.2. The first skimmer was positioned such that the nozzle was between 2-3 mm from the end of the skimmer at maximum extension and 73 mm from the skimmer at minimum extension. By measuring the arrival time distribution of the beam species at different nozzle-skimmer distances the optimum distance for the nozzle could be determined from the shape of the arrival time distribution (Figure 3.3.18). The nozzle-skimmer distance used in the studies described in Chapter 5 was close to 250 nozzle diameters (nozzle aperture 70 μm) in accord with previous results using this nozzle arrangement [Cameron 1993].

The 4.5 inch diameter electron gun top hat was aligned physically with the middle of the laser beam aligning the skimmers and hexapole. However, the electron gun itself could be adjusted independently under vacuum within the top hat using the xyz translator. Before the beginning of any experiment the position of the electron gun was optimised in the x and y directions in order to maximise the supersonic beam-electron beam overlap and optimise the ion signal. Shown in Figure 3.3.19 is the ion signal profile when the electron gun is translated through the y-direction perpendicular to the molecular beam. The electron gun is positioned to give the maximum ion signal and is re-optimised after each disassembly and reinstallation of the electron gun. The z-direction adjustment was fixed in order to keep the electron gun as close as possible to

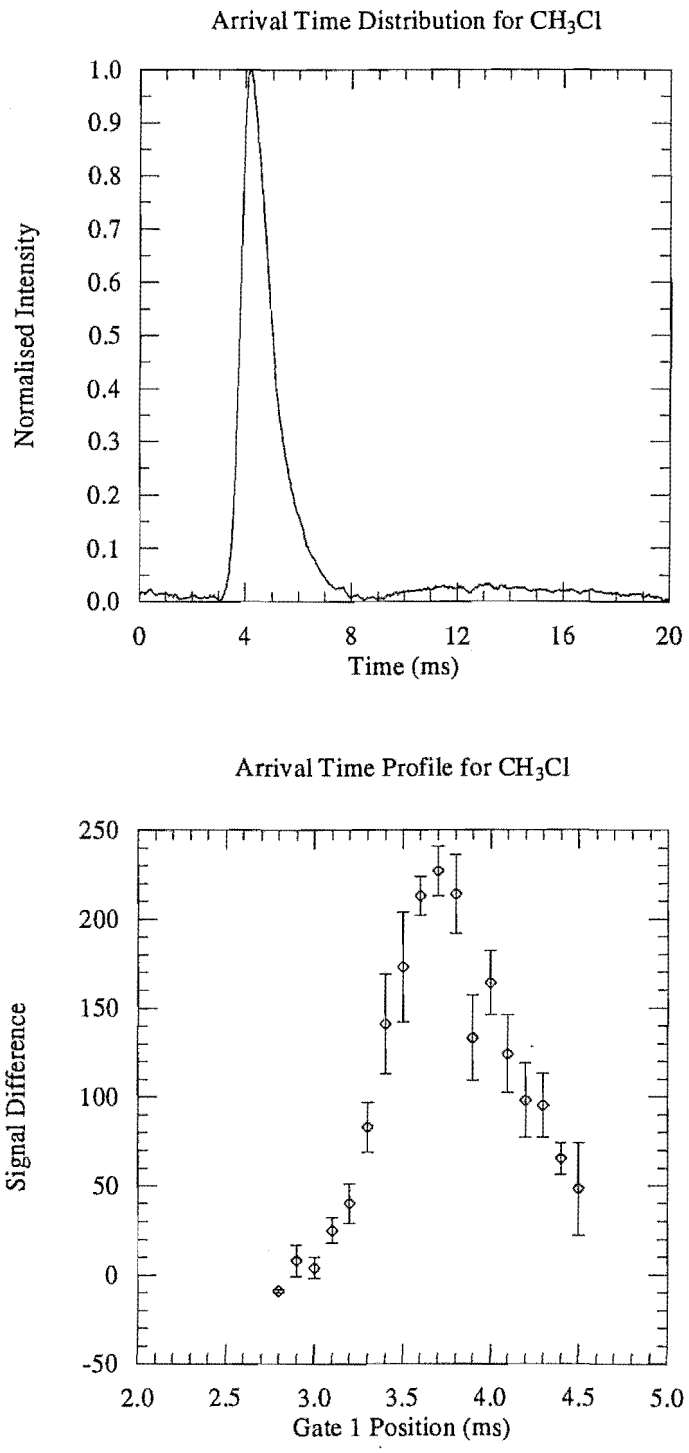

Figure 3.3.17: Arrival time distribution and arrival time profile for CH_3Cl as measured by the Vacuum Generators SXP-300 quadrupole mass spectrometer (analogue mode) and Amptektron MD-501L thermal ion detector (pulse counting mode) respectively.

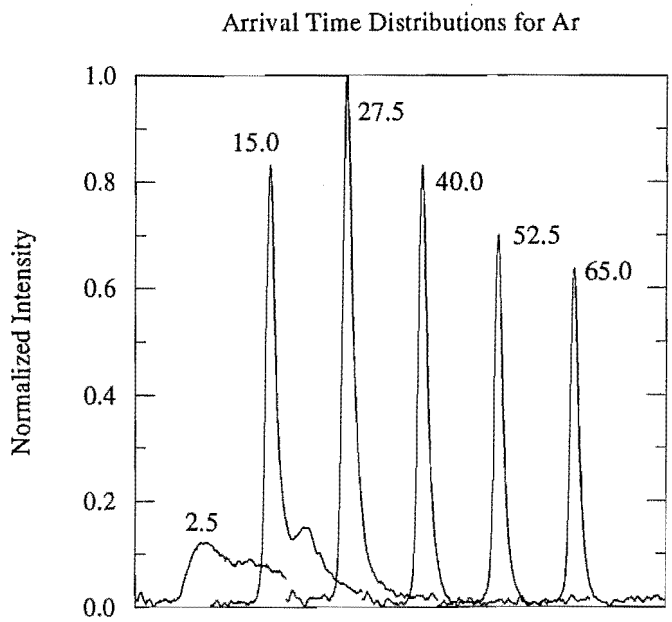

Figure 3.3.18: Arrival time distributions measured on the Vacuum Generators SXP-300 quadrupole mass spectrometer at various nozzle to skimmer distances. The numbers within the graph represent the nozzle to skimmer distance in millimetres. Each arrival time distribution has been offset from the previous distribution for clarity.

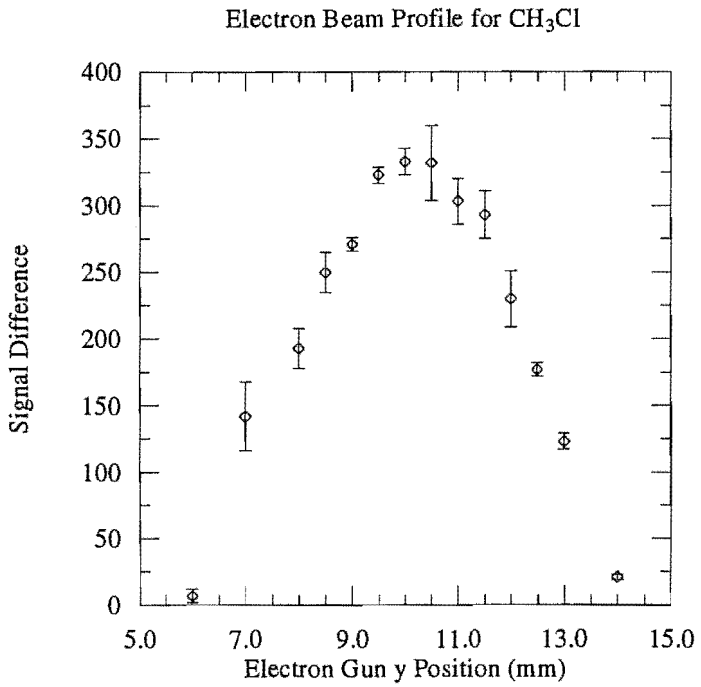

Figure 3.3.19: Beam profile for CH_3Cl when the electron gun is translated perpendicular to the molecular beam axis (molecular beam profile convoluted with the electron beam profile).

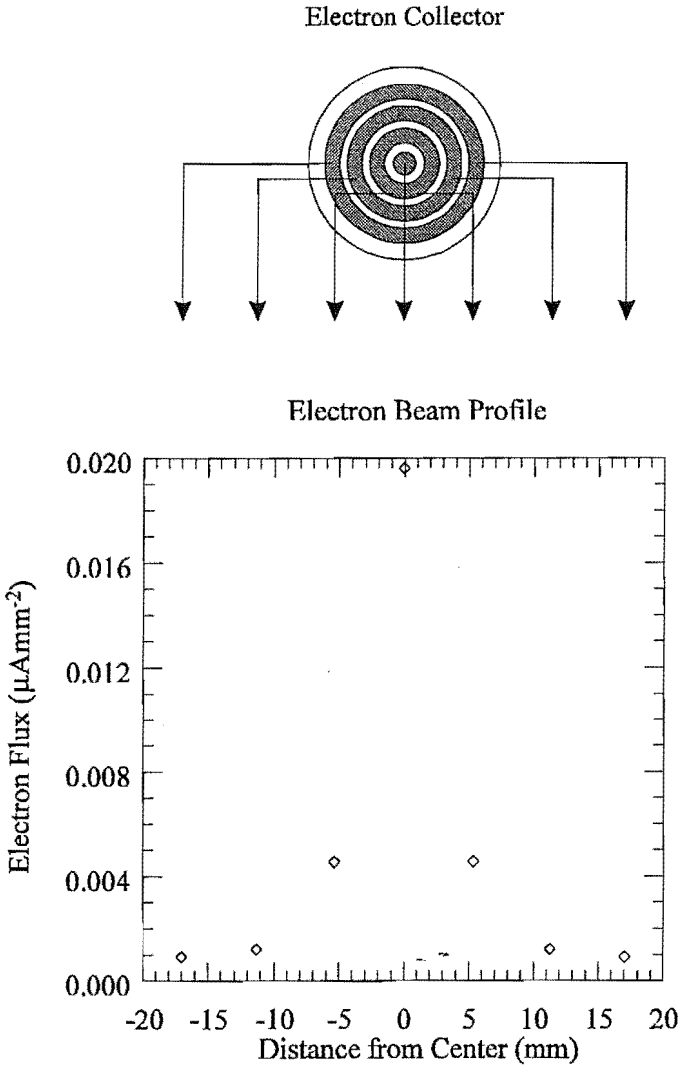

Figure 3.3.20: Electron beam profile using a four concentric ring electron detector. The shaded rings have areas 7.3, 45.2, 82.1 and 117.4 mm^2.

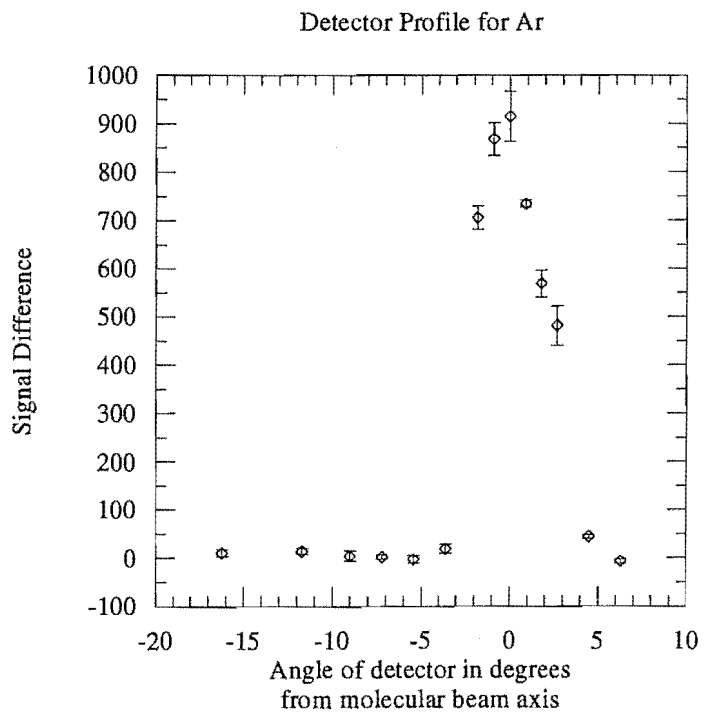

Figure 3.3.21: Amptektron MD-501L thermal ion detector profile for an argon beam as the Amptektron is stepped across the beam axis. A negative angle represents movement of the Amptektron towards the electron collector as viewed in Figure 3.3.14.

the field plates and optimise the electron beam current. Moving the electron gun back along the z-axis resulted in a linear decrease in electron current at the detector indicating that the electron beam was slightly diffuse.

During one period of the stage III research the focusing and characterisation of the electron beam was performed using a concentric ring electron current collector positioned at the scattering centre. The electron collector (Figure 3.3.20) comprised four rings of areas (in mm^2) 7.3, 45.2, 82.1 and 117.4. The electron flux measured on each element for 100 eV electron gun settings with 10 mm electron gun apertures on the top hat are also shown on Figure 3.3.20. From the flux diagram the diameter of the electron beam was determined to be between 5-6 mm. The 5 mm diameter snout on the electron gun top hat, used in the later experiments, gave additional collimation for a well defined electron beam.

When the quadrupole mass spectrometer was used as the detector no further alignment was required as the quadrupole was aligned by laser on installation. However, when the Amptektron particle detector was used further alignment was necessary. The vertical adjustment of the Amptektron on the stepping motor was achieved by measuring the height of the laser beam from the base and then adjusting the Amptektron mount to

align the Amptektron aperture with the laser beam. The horizontal centering of the Amptektron about the scattering centre could be approximated visually through a window on the scattering chamber but had to be experimentally verified before experiments. To align the Amptektron a molecular beam was used and the Amptéktron stepped either side of the centre to provide a cross section beam profile (Figure 3.3.21). The Amptektron would then be positioned where the pulse counting signal was maximum.

Once the optimisation of the nozzle, electron gun and detector was complete an experiment could be attempted, as described in Chapter 5.

Chapter 4

Ionisation of Clusters

During a nozzle expansion from a high pressure to a high vacuum the beam molecules experience a high collision frequency with a consequential lowering of the random translational and the rotational temperatures on exiting the nozzle. This can result in molecules condensing to form molecular clusters which are held together by weak van der Waals forces (see Section 2.2). Clusters represent a middle ground between the atomic or molecular state and the bulk phase state of a system. Characterisation of cluster size distributions and the determination of the properties that control cluster formation can lead to a greater understanding of the evolution process from molecular level to bulk level and also can provide information on the mechanism of such processes. A greater knowledge of these processes, which are encountered in catalysis, liquid structure or solvation, can then be obtained. Although atomic and molecular clusters have been investigated for over 30 years a complete understanding of the mechanisms of cluster formation and the factors that govern the stability of such species is still limited. The essentially collision free environment of the molecular beam provides the opportunity to investigate clusters without further aggregation and the use of a quadrupole mass spectrometer detector facilitates cluster ion specificity.

In this Chapter, the appearance energies of $(CO_2)_n^+$ $(2 \leq n \leq 4)$, $(N_2O)_n^+$ $(2 \leq n \leq 4)$, $(NH_3)_nNH_4^+$ $(0 \leq n \leq 7)$ and the cluster ion fragments $(N_2O.O)^+$ and $(N_2O.NO)^+$ are discussed. The clusters are formed in a supersonic expansion with the ionisation efficiency curves measured by electron impact ionisation in a commercial quadrupole mass spectrometer.

4.1 Experimental

The experimental configuration used to collect the ionisation efficiency curve data is shown schematically in Figure 4.1.1. The beam source driver unit provides the primary trigger to the nozzle. The beam source driver also triggers a pulse generator which is fed to a custom built pulse delay unit. The output from the pulse delay unit consists of two TTL gates of equal variable width but independent variable time delays. The two gates each represent one input for two separate and-gates.

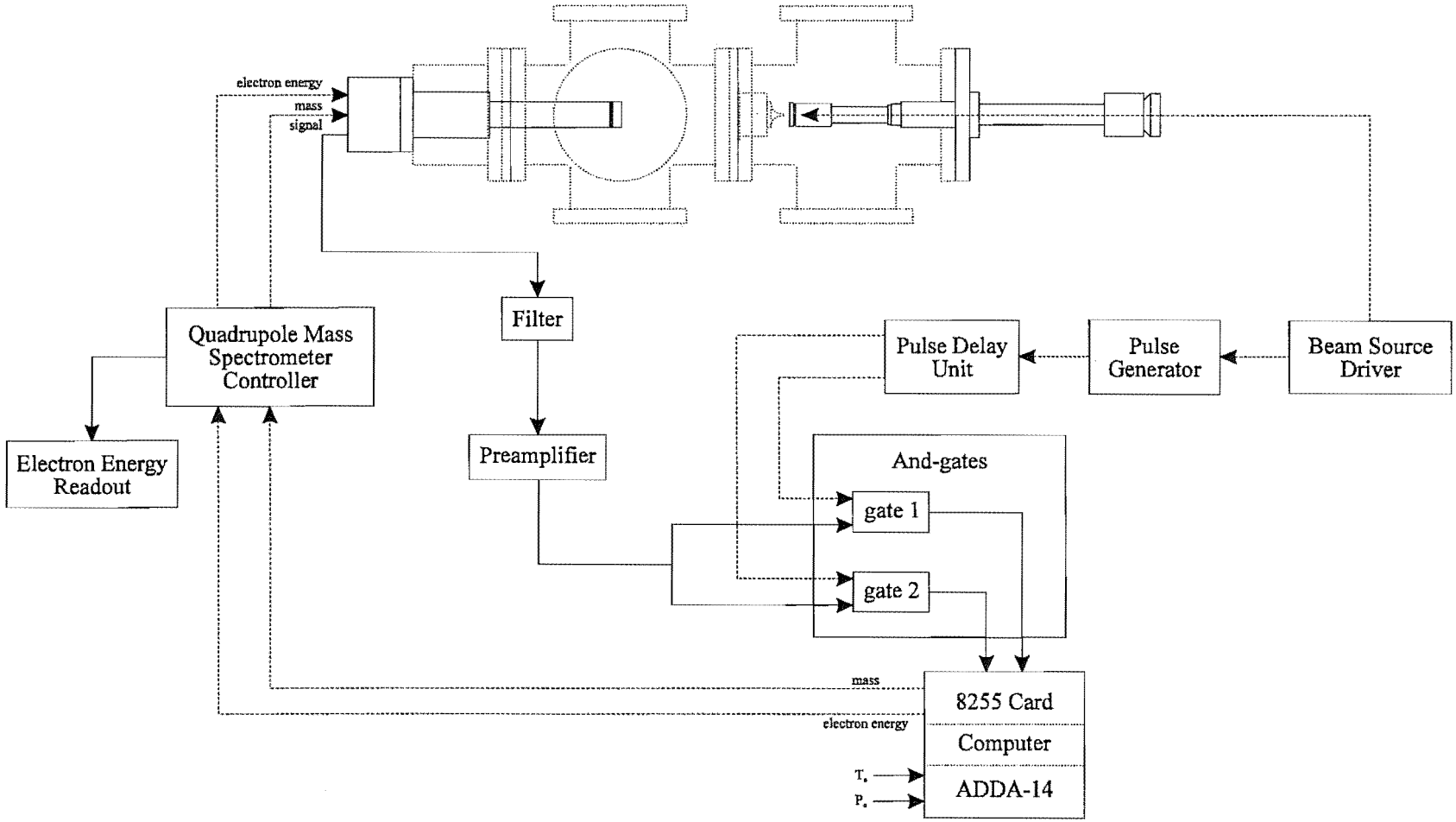

Figure 4.1.1: Experimental arrangement for the collection of ionisation efficiency curve data of small cluster ions.

The molecular beam was passed through a skimmer and allowed to enter the ion source of a Vacuum Generators SXP-300 quadrupole mass spectrometer 10 cm downstream from the skimmer assembly. The molecular beam was ionised by electron impact in the source of the quadrupole mass spectrometer, mass filtered and detected by a channeltron electron multiplier. The output pulses from the channeltron electron multiplier were passed through a high-Q 2 MHz notch filter to remove any pick-up induced from the mass spectrometer radio frequency generator and then amplified with a fast preamplifier followed by an amplifier and pulse amplitude discriminator combination. The TTL output from the pulse counting preamplifier was split and represents the second input for each of the two and-gates.

The time delay of the two TTL gates were set on the oscilloscope such that the first gate covered the arrival time distribution of the supersonic beam pulse, and the second gate covered only background noise as shown in Figure 3.2.5. The output from the first and-gate (gate 1) consisted of both beam and background pulses and the output from the second and-gate (gate 2) consisted of background pulses only. The output pulses from the two and-gates were counted using a PCL 8255 counter-timer card occupying a 16-bit slot in the computer and recorded via custom written interfacing software.

The computer controlled both the electron energy and mass selection of the quadrupole mass spectrometer via custom built 12-bit digital-to-analogue converters incorporated into the mass spectrometer controller unit. The selected mass was displayed on the controller unit display and the electron energy was monitored using a digital voltmeter.

Neutral CO_2, N_2O and NH_3 clusters were produced by expanding gas mixtures containing 100 torr argon, 500 torr CO_2, N_2O or NH_3 and made to a total pressure of about 4000 torr with helium at a reservoir temperature of 295 K. These mixtures produced supersonic beams of sufficiently high cluster content for reliable determination of appearance energies for the cluster ions $(CO_2)_n^+$ $(2 \leq n \leq 4)$, $(N_2O)_n^+$ $(2 \leq n \leq 4)$, $(NH_3)_nNH_4^+$ $(0 \leq n \leq 7)$ and the cluster ion fragments $(N_2O.O)^+$ and $(N_2O.NO)^+$. No clusters containing helium or argon atoms were observed for any of the gas mixtures.

Ion counts were measured at up to 100 points, in 0.1 eV steps, with a typical counting period of 5 seconds at each electron energy repeated between 15 to 20 times. Average ion counts were also measured at 70 eV at the beginning and end of each run. The appearance energy of Ar^+ was measured simultaneously with each of the systems studied to provide an internal standard for the electron energy scale (the Ar^+ appearance energy was taken as 15.76±0.01 eV [Dibeler 1966] in all measurements). A typical collection period, depending on the number of ions recorded, could take between 3-4 hours. Since the nozzle or reservoir temperature and backing pressure can alter the cluster size distribution within a beam pulse [Scoles 1988] it is important that these parameters do not alter appreciably over an experimental collection period. The temperature of the nozzle was monitored by a calibrated thermocouple wedged between the nozzle and nozzle assembly. The energy difference across the thermocouple was amplified and monitored by a 14-bit analogue-to-digital conversion channel (ADDA-14

card) and custom written software. No change in nozzle temperature was observed. The reservoir pressure was monitored using an MKS Baratron (10,000 torr) connected to an MKS type 286 controller. The calibrated 0 V to 10 V output from the controller was monitored by another analog-to-digital conversion channel. Due to the small flow of gas through the 50 μm nozzle aperture, the reservoir pressure was observed to drop by no more than 2-3% over a four hour period of operation.

4.2 Results and Discussion

Electron impact ionisation techniques, although widely used for fifty years, suffer from two main problems which decrease the accuracy of the technique and which must be taken into account. The energy spread of the ionising electron beam is often significant (for these studies the spread was estimated to be 0.85 eV FWHM), and the actual mean energy of the electron beam may differ considerably from the nominal electron energy expected from the applied electrode energies. For appearance energy measurements near threshold, where the signal to noise ratio is low, extrapolation methods [McDowell 1963, Kiser 1965] can be used to determine the appearance energy. Using an accurate extrapolation method with comparison to a measured known calibrant ion appearance energy corrections can be made which minimise the errors associated with the energy spread and mean energy of the ionising electron beam. In the measurements presented here the Ar^+ ionisation efficiency curve was simultaneously measured with each cluster ion ionisation efficiency curve to provide a standard for the electron energy. The semi-log plot method [McDowell 1963, Kiser 1965] was used to determine the cluster ion appearance energies with an estimated accuracy of ±0.1 eV in all cases. These measurements are nominally less accurate than photoionisation methods but are sufficient to allow critical comparisons to be made between the present results and previous investigations. Corrections to the energy scale, based on the known appearance energy of Ar^+, were typically between 0.2 eV and 0.5 eV.

4.2.1 CO_2 Clusters

Typical ionisation efficiency curves for $(CO_2)_n^+$ $(2 \leq n \leq 4)$ are shown in Figure 4.2.1, where the observed ion count is plotted as a function of the uncorrected ionising electron energy. Corrected appearance energies for the CO_2 cluster ions are shown in Table 4.2.1 together with previously determined values.

As seen from Table 4.2.1 the appearance energy of $(CO_2)_2^+$ determined in this study was identical to that of Stephan *et al* using the same technique. Both values were considerably smaller than the values obtained from the photoionisation studies which suggests that the two methods of ionisation may yield different results. Variation in photoionisation appearance energies for the dimer ion has been attributed to the refracted ultraviolet light inducing ionisation which makes the identification of the true appearance energy difficult [Linn 1981].

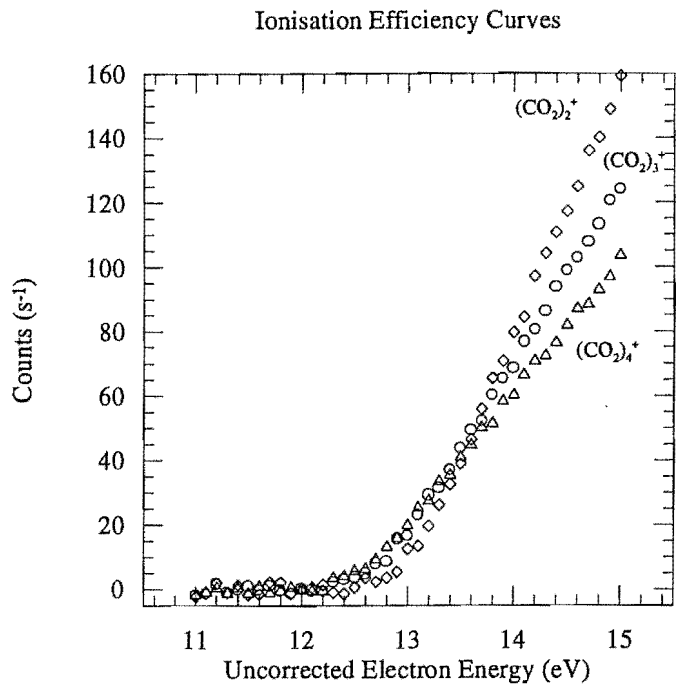

Figure 4.2.1: Measured ionisation efficiency curves for $(CO_2)_2^+$, $(CO_2)_3^+$ and $(CO_2)_4^+$. Every second point on this and other ionisation efficiency curves has been removed for clarity.

	Appearance Energy (eV)	
Cluster Ion	Present Study	Previous Studies
$(CO_2)_2^+$	13.1	13.32[a]
		13.40[b]
		13.1[c]
$(CO_2)_3^+$	12.8	13.24[a]
$(CO_2)_4^+$	12.6	13.18[a]

[a] [Linn 1981], [b] [Jones 1978], [c] [Stephan 1982a]

Table 4.2.1: CO_2 cluster ion appearance energies.

Following ionisation, extensive fragmentation of the cluster species can occur [Scoles 1988]. There was some concern that the contributions to the ionisation efficiency curve from the fragmentation of larger clusters may affect the determined ionisation threshold. Reducing the reservoir pressure (to around 2000 torr) the population of larger cluster species can be made negligible. Measurements under these conditions did not alter the appearance energies or shape of the ionisation efficiency curves observed for any of the systems studied. The fragmentation of larger clusters, to produce cluster ions of smaller sizes, would be expected to introduce changes in slope or

breaks in the ionisation efficiency curve for the cluster ion. The inability to detect any such breaks was considered to be a result of the relatively low resolution of the experimental arrangement employed.

Klots and Compton [Klots 1978] have suggested that the equilibrium geometry of van der Waals cluster ions produced by electron impact or photoionisation may be considerably different from the equilibrium geometry of the neutral precursor. In these situations the measured appearance energies may not represent the true adiabatic ionisation energy for the van der Waals cluster [Klots 1978, Stephan 1982a]. In order to determine whether or not the determined cluster ion appearance energy is close to the true adiabatic value, it is necessary to compare thermochemical data deduced from these measurements with that obtained from ion-molecule equilibrium experiments. For the generalised association reaction

$$A^+ + B + M \rightarrow BA^+ + M$$

the dissociation energy of the B-A^+ bond is equivalent to the negative enthalpy change for the reaction and may be measured directly using ion-molecule equilibrium methods. The dissociation energy may also be obtained from the appearance energy measurements according to the equation

$$D_{BA^+} = AP_{A^+} - AP_{BA^+} + D_{BA}$$

where AP_{BA^+} and AP_{A^+} are the appearance energies of BA^+ and A^+ respectively and D_{BA^+} and D_{BA} are the dissociation energies of BA^+ and BA respectively. This represents an indirect measurement of the dissociation energy which requires estimation of the neutral BA binding energy and a knowledge of the appearance energy of A^+. If a considerable geometry change occurs following ionisation the appearance energy determined for BA^+ may be too large resulting in an underestimation of the dissociation energy.

In order to calculate the bond dissociation energy of $(CO_2)_2^+$ it is necessary to know the binding energy of the neutral CO_2 dimer and the appearance energies of CO_2^+ and $(CO_2)_2^+$. The binding energy of the neutral dimer has not been determined experimentally, *ab initio* calculations by Illies *et al* [Illies 1987] determined a binding energy of 0.056 eV for the reaction

$$(CO_2)_2 \rightarrow CO_2 + CO_2$$

for the staggered parallel configuration of the neutral dimer [McKee 1990]. The appearance energy of CO_2^+ is 13.769 eV [Rosenstock 1977] which, together with the appearance energy of the dimer cluster ion measured in this study give the bond dissociation energy of $(CO_2.CO_2)^+$ as 0.73 eV. Because of the degree of translational and rotational cooling associated with the supersonic expansion it can be considered that this value will be close to the negative enthalpy change at 0 K for the association reaction

$$CO_2^+ + CO_2 \rightarrow CO_2.CO_2^+$$

which has been observed by a number of authors using high pressure mass spectrometry. The calculated binding energies for the dimer, trimer and tetramer CO_2 cluster ions are shown in Table 4.2.2 with ion-molecule results from the appropriate association reactions corrected to 0 K [Linn 1981]. Although the cluster binding energies of the neutral CO_2 trimer and tetramer species are unknown it is considered that it will remain similar to the binding energy of the neutral dimer in the initial stages of cluster formation. Each of the calculated binding energies for the clusters are in good agreement with the results from the association reactions.

	Binding Energies 0 K (eV)	
Cluster Ion	Present Study	Ion-Molecule Results
$(CO_2)_2^+$	0.73	0.675[a] 0.563[b]
$(CO_2)_3^+$	0.36	0.32[a]
$(CO_2)_4^+$	0.26	0.22[c]

[a] [Keesee 1986], [b] [Mautner 1977], [c] [Hiraoka 1988]

Table 4.2.2: CO_2 cluster ion binding energies.

4.2.2 N_2O Clusters

Ionisation efficiency curves for the cluster ions $(N_2O)_n^+$ $(2 \leq n \leq 4)$ and the cluster ion fragments $(N_2O.O)^+$ and $(N_2O.NO)^+$ are shown in Figure 4.2.2 with the corrected appearance energies for each ion species tabulated in Table 4.2.3 with other previously determined values.

	Appearance Energy (eV)	
Cluster Ion	Present Study	Previous Studies
$(N_2O)_2^+$	12.3	12.35[a] 12.394[b]
$(N_2O)_3^+$	12.1	12.29[b]
$(N_2O)_4^+$	12.0	12.26[b]
$(N_2O.O)^+$	14.6	
$(N_2O.NO)^+$	14.3	14.01[a]
	17.0	

[a] [Linn 1981], [b] [Kamke 1989]

Table 4.2.3: N_2O cluster ion appearance energies.

The appearance energy for $(N_2O)_2^+$ is in excellent agreement with the photoionisation results of Linn *et al* [Linn 1981] and Kamke *et al* [Kamke 1989]. The

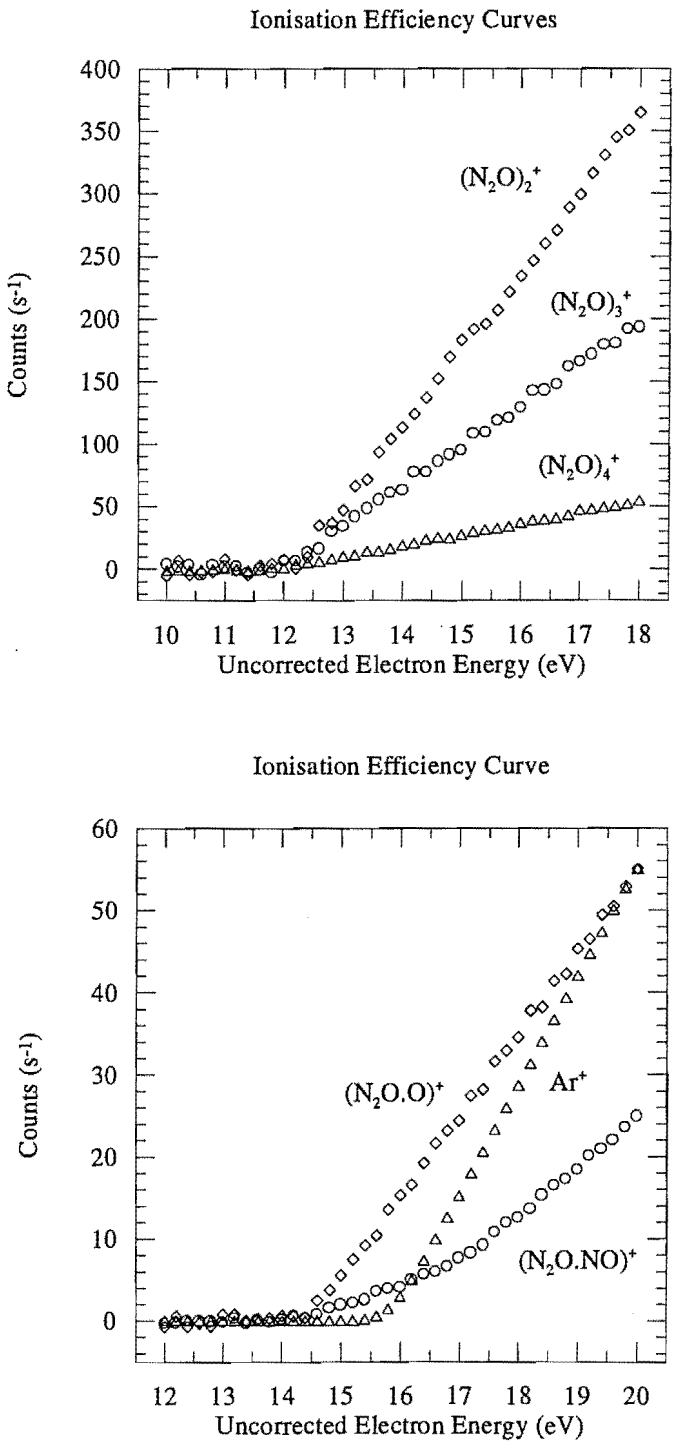

Figure 4.2.2: Measured ionisation efficiency curves for $(N_2O)_2^+$, $(N_2O)_3^+$ and $(N_2O)_4^+$ (top graph) and $(N_2O.O)^+$, $(N_2O.NO)^+$ and Ar^+ (bottom graph).

appearance energy of the $(N_2O.NO)^+$ cluster ion fragment is in reasonable accord with 14.01 eV determined by Linn *et al* [Linn 1981]. However, on examination of the ionisation efficiency curve for $(N_2O.NO)^+$ (Figure 4.2.2), there is a definite change of slope at approximately 17.0 eV suggesting the presence of a second threshold for the $(N_2O.NO)^+$ ion formation. This second threshold is also apparent on the $(N_2O.NO)^+$ ionisation efficiency curve of Linn *et al* [Linn 1981] at approximately 17.2 eV which supports the observation of a second, higher energy threshold.

In view of the good agreement between the present results and the photoionisation appearance energies of Linn *et al* for $(N_2O)_2^+$ and $(N_2O.NO)^+$, it is reasonable to expect that the appearance energies for $(N_2O)_3^+$, $(N_2O)_4^+$ and $(N_2O.O)^+$ to be equally reliable. The appearance energies determined by Kamke *et al* [Kamke 1989] for $(N_2O)_3^+$ and $(N_2O)_4^+$ are approximately 0.2 eV higher than the values determined in the present study, however, the accuracy of the Kamke *et al* results are limited by the choice of the fitting procedure for the data.

The calculation of the $(N_2O)_n^+$ cluster ion binding energies can be achieved by similar means to that for the $(CO_2)_n^+$ cluster ions in Section 4.2.1. Using the appearance energies measured for the $(N_2O)_n^+$ cluster ions from Table 4.2.3 and the appearance energy of 12.886±0.002 eV for N_2O^+ [Rosenstock 1977], with an estimated intermolecular binding energy of 0.02 eV [Johnston 1940] for the neutral dimer, the binding energies for each of the $(N_2O)_n^+$ cluster ions are calculated and shown in Table 4.2.4. The binding energies are in good agreement with ion-molecule methods apart from the photoionisation measurements of Kamke *et al* as mentioned previously.

	Binding Energies 0 K (eV)	
Cluster Ion	Present Study	Previous Studies
$(N_2O)_2^+$	0.61	0.56[a] 0.57[b] 0.512[c]
$(N_2O)_3^+$	0.22	0.124[c]
$(N_2O)_4^+$	0.12	0.05[c]
$(N_2O.O)^+$	0.71	

[a] [Linn 1981], [b] [Illies 1988], [c] [Kamke 1989]

Table 4.2.4: N_2O Cluster Ion Binding Energies

The difference in appearance energies between the $(N_2O.O)^+$ cluster ion fragment and the $(N_2O)_2^+$ cluster ion is observed to be 2.3 eV from Table 4.2.3. This seems to be in agreement with the 2.4 eV difference between the appearance energies of N_2O^+ from N_2O (12.886 eV) and O^+ from N_2O (15.29 eV [Rosenstock 1977]). A possible interpretation of this observation is to suggest that the formation of the fragment ion involves ionisation and fragmentation of one of the N_2O monomer units in $(N_2O)_2$ without significant perturbation of the second monomer unit. A similar argument can be applied for the species $(CO.CO_2)^+$ and $(NH_2.NH_3)^+$ observed by Stephan *et al* [Stephan

1982a, Stephan 1982b], although they proposed an alternative mechanism involving an internal cluster ion-molecule reaction. Independent of the mechanism involved, the binding energy of $(N_2O.O)^+$ can be calculated as 0.71 eV using the appearance energy of $(N_2O.O)^+$, the appearance energy of 15.29 eV for formation of O^+ from N_2O and the 0.02 eV binding energy for the neutral N_2O dimer.

The differences between the two threshold appearance energies for $(N_2O.NO)^+$ and for $(N_2O)_2^+$ correspond to 2.0 eV and 4.7 eV (Table 4.2.3). These are again in reasonable accord with the 2.124 eV and 4.854 eV differences between the 12.886 eV appearance energy for N_2O^+ and the thermochemical thresholds of 14.19 eV and 17.76 eV for the fragmentation processes [Rosenstock 1977]

$$N_2O + e \rightarrow N_2O^+ + 2e \rightarrow NO^+(X^1\Sigma^+) + N(^4S) + 2e$$

and

$$N_2O + e \rightarrow N_2O^+ + 2e \rightarrow NO^+(X^1\Sigma^+) + N(^2P) + 2e.$$

N_2O^+ can also undergo fragmentation leading to the formation of $NO^+(X^1\Sigma^+) + N(^2D)$ with a thermochemical threshold of 16.57 eV [Rosenstock 1977]. In this case a further break in the ionisation efficiency curve of $(N_2O.NO)^+$ would be expected between 14.3 eV and 17.0 eV. In the present study other breaks could not be detected although there is evidence of such a feature on the photoionisation efficiency curve measured by Linn *et al* [Linn 1981]. Additionally, Linn *et al* noted that the photoionisation efficiency curve measured for $(N_2O.NO)^+$ had essentially the same profile as that measured for NO^+ from fragmentation of N_2O^+, which further supports the proposal that ionisation of the neutral N_2O dimer occurs on a single monomer unit.

4.2.3 NH_3 Clusters

Ionisation of neutral ammonia clusters results in the clusters undergoing an internal ion-molecule reaction resulting in the loss of NH_2 and the formation of an NH_4^+ core [Wei 1990a, Wei 1990b]. Virtually no unprotonated ammonia cluster ions $(NH_3)_n^+$ are detected [Stephan 1982b, Wei 1990a]. In the present study the ion counts for the unprotonated cluster ion at the threshold were too low to facilitate accurate determination of the appearance energies.

Ionisation efficiency curves for the protonated ammonia cluster ions $(NH_3)_nNH_4^+$ $(0 \leq n \leq 7)$ are illustrated in Figure 4.2.3 with the corrected appearance energies listed in Table 4.2.5. The appearance energies are in general agreement with the results of Ceyer *et al* [Ceyer 1979] using photoionisation. Additionally it was possible to determine the appearance energies of the cluster ions $(NH_3)_nNH_4^+$ $(3 \leq n \leq 7)$ which have not been previously reported.

The proton affinity of ammonia can be determined from a knowledge of the NH_2-H bond strength and the appearance energies of H^+ and NH_4^+. The NH_2-H bond strength has been determined to be 4.60 eV [Bohme 1973] and the appearance energy of

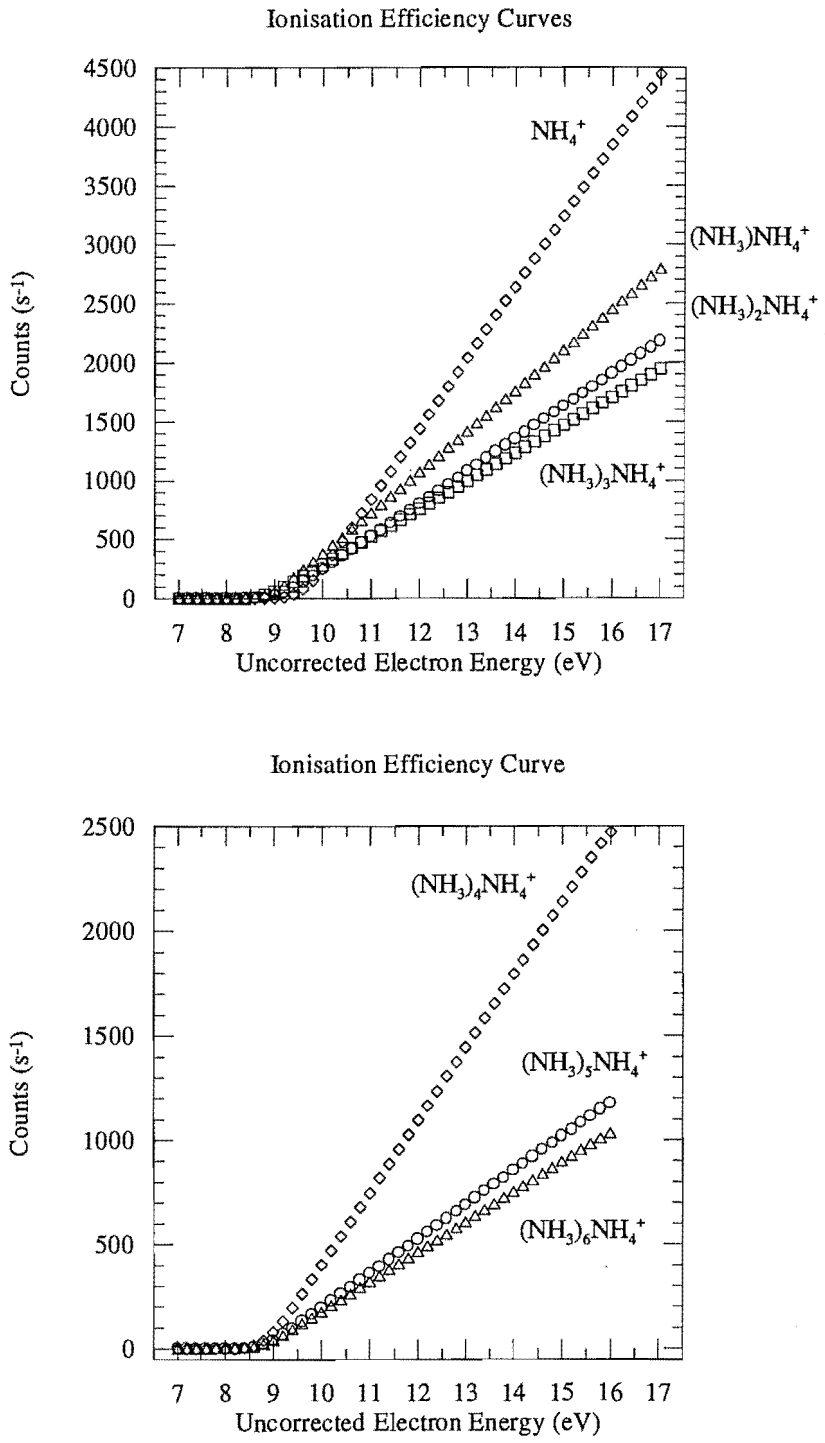

Figure 4.2.3: Measured ionisation efficiency curves for $(NH_3)_nNH_4^+$. The ionisation efficiency curve for $(NH_3)_7NH_4^+$ would be superimposed on that measured for $(NH_3)_6NH_4^+$ and has therefore been omitted. The higher signal level for $(NH_3)_4NH_4^+$ over $(NH_3)_2NH_4^+$ and $(NH_3)_3NH_4^+$ reflects the higher stability of the pentamer structure.

H^+ 13.598 eV [Rosenstock 1977]. Taking the value of 9.7 eV from Table 4.2.5 for the appearance energy of NH_4^+, the proton affinity of ammonia was estimated to be 8.5 eV at 0 K, or 8.6 eV corrected to 298 K, which is in reasonable agreement with the accepted value of 8.96±0.08 eV at 298 K [Lias 1980].

	Appearance Energy (eV)	
Cluster Ion	Present Study	Previous Studies
NH_4^+	9.7	9.59[a] 9.95[b]
$(NH_3)NH_4^+$	9.2	9.15[a] 9.50[b]
$(NH_3)_2NH_4^+$	9.0	9.03[a] 9.20[b]
$(NH_3)_3NH_4^+$	8.9	
$(NH_3)_4NH_4^+$	8.9	
$(NH_3)_5NH_4^+$	8.8	
$(NH_3)_6NH_4^+$	8.8	
$(NH_3)_7NH_4^+$	8.7	

[a] [Ceyer 1979], [b] [Stephan 1982b]

Table 4.2.5: NH_3 cluster ion appearance energies.

The enthalpy change for the hydrogen abstraction reaction

$$NH_3^+ + NH_3 \rightarrow NH_4^+ + NH_2$$

can be also determined from the binding energy of the neutral dimer and the appearance energy of NH_3^+, which are 0.15±0.04 eV [Duquette 1978] and 10.166 eV [Rosenstock 1977] respectively. These values together with the appearance energy of NH_4^+ give a negative enthalpy change of 0.62 eV which is in reasonable agreement with those of 0.45±0.3 eV [Stephan 1982b] and 0.74±0.4 eV [Ceyer 1979] from appearance energy measurements. However, all of these results are in disagreement with the ion-molecule value of 1.08 eV at 298 K [Stephan 1982b] calculated from the proton affinity of ammonia and the heats of formation of NH_3, NH_2 and H^+ [Rosenstock 1977]. Correcting the ion-molecule result to 0 K only slightly reduces the discrepancy but still indicates that none of the measured NH_4^+ appearance energies correspond to the true adiabatic ionisation threshold indicative of clusters in which the ammonia monomers do not behave as weakly coupled relatively undisturbed monomer units.

The binding energy of 0.15 eV in conjunction with the appearance energies, listed in Table 4.2.5, for the protonated ammonia clusters may be used to calculate the solvation energy of an ammonium ion by one to seven ammonia molecules. The

calculated solvation energies are presented in Table 4.2.6 together with literature values determined using ion-molecule techniques such as high pressure mass spectrometry. The agreement between this study and the ion-molecule equilibrium methods are not good indicating again that the measured appearance energy values fail to yield the true adiabatic ionisation threshold for the generation of protonated ammonia clusters from their respective neutral precursors. This inability may reflect the geometric changes that are required for the proton transfer reaction channel to occur.

	Solvation Energies $(NH_3)_nNH_4^+ \rightarrow (NH_3)_{n-1}NH_4^+ + NH_3$	
n,n-1	Present Study	Previous Studies
1,0	-0.65	-0.797[a]
		-0.931[b]
		-1.074[c]
		-1.169[d]
2,1	-0.35	-0.701[b]
		-0.758[c]
		-0.736[d]
3,2	-0.25	-0.550[e]
		-0.610[b]
4,3	~-0.2	-0.525[e]
5,4	~-0.2	-0.290[e]
6,5	~-0.2	-0.250[e]
7,6	~-0.2	-0.235[e]

[a] [Wincel 1972], [b] [Arshadi 1974], [c] [Payzant 1973], [d] [Searles 1968], [d] [Wei 1990b]

Table 4.2.6: NH_4^+ solvation energies.

4.3 Conclusion

Appearance energies have been determined for the van der Waals cluster ions $(CO_2)_n^+$ $(2 \leq n \leq 4)$, $(N_2O)_n^+$ $(2 \leq n \leq 4)$, $(NH_3)_nNH_4^+$ $(0 \leq n \leq 7)$ and the cluster ion fragments $(N_2O.O)^+$ and $(N_2O.NO)^+$ using electron impact ionisation. The appearance energies were found to be in general agreement with previously reported values with the appearance energies of $(N_2O.O)^+$ and $(NH_3)_nNH_4^+$ $(3 \leq n \leq 7)$ being reported for the first time [Cameron 1994]. A proposed mechanism for the formation of the cluster fragment ions $(N_2O.O)^+$ and $(N_2O.NO)^+$ involves the ionisation and fragmentation of one of the N_2O molecules in the neutral N_2O dimer without any significant perturbation of the accompanying molecule. Although this proposed mechanism supports the information to date alternative mechanisms cannot be discounted.

The dissociation energies for the $(CO_2)_n^+$ and $(N_2O)_n^+$ systems deduced from appearance energies were observed to be in general agreement with those obtained from ion-molecule measurements. The dissociation energies observed for the $(NH_3)_nNH_4^+$ system however, was in considerable disagreement with values obtained by ion-molecule methods indicating that electron impact ionisation measurements fail to sample the true adiabatic ionisation threshold for these species. However, electron impact ionisation efficiency curves do provide significant mechanistic information where curve breaks are found and where comparisons with monomer measurements and data collected using other techniques are available.

Chapter 5

Electron Impact Ionisation Asymmetry Results

The primary focus of this dissertation was to establish if electron impact ionisation was orientation dependent and, if so, to what extent. Since a hexapole electrostatic field and homogeneous electric field was used to select and spatially orient the molecules only symmetric top molecules were used in these studies. The resources available at the time resulted in CH_3Cl being the molecule most comprehensively studied.

5.1 Introduction

The experimental results were obtained over three different periods. After the problems with the Amptektron MD-501L thermal ion detector were resolved (Section 3.3.10.2) the first set of results were obtained using the Amptektron and the larger inscribed radius hexapole mounts. The use of the Amptektron became limited when higher mass symmetric top molecules were used as the oriented beam because of the Amptektron's reduced detection efficiency for these species. At this time the Amptektron ion detector was replaced by the Vacuum Generators SXP-300 quadrupole mass spectrometer, with an ion lens assembly replacing the ion source, as the detection device. Also at this time the hexapole mounts were reduced to the smaller inscribed radius mounts (Section 3.3.7).

The quadrupole mass spectrometer increased the versatility of the general experiment. The mass range of detectable species was increased and the fragment ions could also be measured in addition to the molecular ion. Through this period different symmetric top molecules were used with the majority of results involving CH_3Cl and the two main mass peaks of m/z=50 and 15. Continued experimentation with the quadrupole mass spectrometer was precluded by a series of electron multiplier failures and non-reproducibility of arrival time distribution intensities with new electron multipliers.

The third period of research returned to the Amptektron particle detector to concentrate on CH_3Cl and the effect of electron energy on the asymmetry effect previously established.

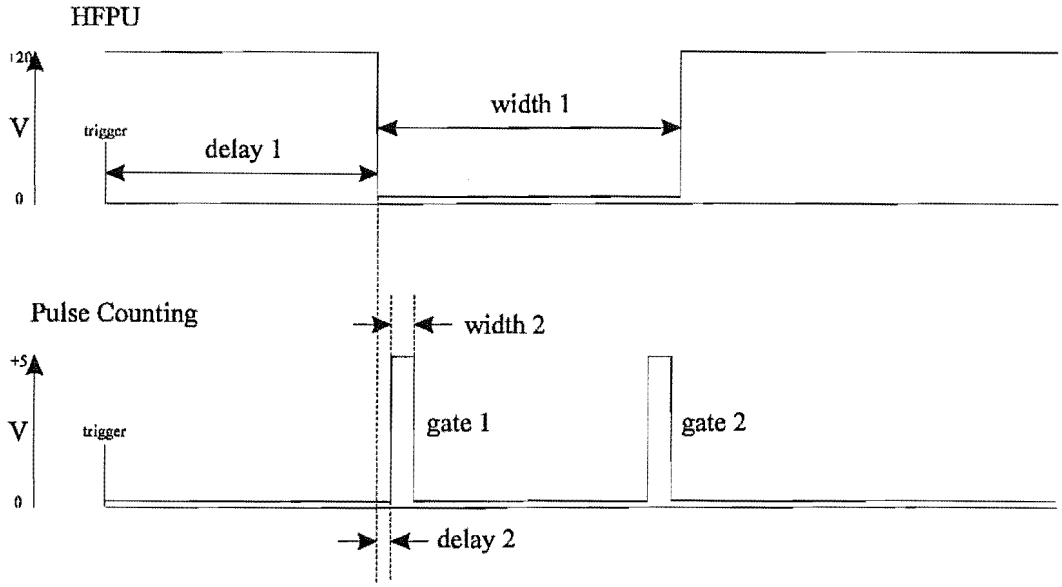

Figure 5.1.1: Timing sequence for a general experiment. The gate 1 delay (delay 1 + delay 2) for the pulse counting is set initially. The time that the HFPU switches from +20 to 0 V is set fractionally before gate 1 by an amount delay 2, which is dependent on the flow velocity of the beam (see text). The width of the HFPU (width 1) is set to encompass the gate 2 width (width 2) and delay.

For the remainder of this section the experimental procedure for setting the timing sequences, the data collection and data analysis will be explained. Individual results from each of the three different collection periods will be described with a section describing the system tests and the comparative analysis between results.

5.1.1 Experimental Timing Sequences

The timing sequence for a general experiment is shown in Figure 5.1.1. The gate 1 position is set at the optimum position from an experimentally determined arrival time profile (Figure 3.3.17), as previously described in Section 4.1, with gate 2 set to a longer delay time where there is only background gas (typically for CH_3Cl gate 1 would be set to 3.5 ms and gate 2 to 9.9 ms).

The homogeneous field pulsing unit delay is set once the gate 1 position has been determined. The time for the ions to travel from the scattering volume to the detector represents the delay that the homogeneous field pulsing unit must be set before gate 1. The distance from the scattering centre to detector is ~46 mm for the Amptektron and so for CH_3Cl (velocity 500 ms^{-1}) the homogeneous field pulsing unit would be set 0.1 ms before gate 1.

When the beam pulse reaches the scattering centre the homogeneous field is still at a high potential so that all molecules that make an adiabatic transition from the hexapole field will be oriented. At this time the homogeneous field is switched to ground potential. Assuming no de-orientation effects (Section 2.4.6) then only those molecules

already under the influence of the homogeneous field will be oriented when ionised by the electron beam. The length of the homogeneous field plates to the scattering centre is 160 mm which equates to a 0.3 ms oriented beam component for CH_3Cl. This component determines the maximum width for gate 1 and gate 2 (width 2 on Figure 5.1.1).

The ions counted by gate 2 must also be ionised in a region of ground potential. Hence, gate 2 is positioned at the latest possible time after gate 1 and the beam pulse. The width of the time period for which the homogeneous field must be at ground must encompass the delay and width of gate 2.

5.1.2 Data Collection and Analysis

The spatial orientations of the symmetric top dipolar molecules with respect to the incident electron beam are labelled $\delta+$ and $\delta-$ depending on whether the electron beam is incident on the positive or negative end of the electric dipole moment respectively. Since only higher Stark states are oriented this coincides with the homogeneous field plate of greatest positive bias being nearer or further from the electron gun respectively.

For a complete experiment four measurements are required, hexapole off and hexapole on for each of the $\delta+$ and $\delta-$ orientations. For each run the difference between the counts under gate 1 and gate 2 are recorded to give a signal intensity (i.e. gate 2 removes the background component from gate 1). The four differences, for each of the four cases, are labelled:

$\delta+_0$ hexapole off, $\delta+$ orientation,

$\delta+_{kV}$ hexapole on, $\delta+$ orientation,

$\delta-_0$ hexapole off, $\delta-$ orientation,

$\delta-_{kV}$ hexapole on, $\delta-$ orientation.

The $\delta+_0$ and $\delta-_0$ signals are recorded under similar conditions apart from the direction of the residual (near ground potential) homogeneous field at the time of measurement. The ratio between these two measurements is representative of the detection efficiency for each orientation which is dependent on the cleanliness (time since last reassembly) of the system and the effect of contact potentials and any small residual electric fields present within the scattering volume. The ratio

$$F = \frac{\delta-_0}{\delta+_0}$$

is calculated and each of the differences adjusted to correct for the different detection efficiencies.

$$\delta^a+_0 = F.\delta+_0$$

$$\delta^{a}+_{kV} = F.\delta+_{kV}$$

$$\delta^{a}-_{0} = \delta-_{0}$$

$$\delta^{a}-_{kV} = \delta-_{kV} .$$

The difference between the hexapole on and hexapole off measurements gives the number of extra ions produced from oriented molecules transmitted by the hexapole field. Hence from the adjusted differences two values of extra counts are obtained for the two orientations

$$D^{+} = \delta^{a}+_{kV} - \delta^{a}+_{0}$$

$$D^{-} = \delta^{a}-_{kV} - \delta^{a}-_{0} .$$

From these values two representations of steric effects were calculated; the G-factor and the ratio R.

The G-factor is defined as

$$G = \frac{D^{-} - D^{+}}{D^{-} + D^{+}}$$

which has a range of $-1 \leq G \leq 1$. If the negative end of the molecule was exclusively favoured, then G=1 (as $D^{+}=0$) and if the positive end of the molecule was exclusively favoured, then G=-1. If there was no orientation asymmetry $D^{-}=D^{+}$ and G=0.

The ratio R is given by

$$R = \frac{D^{+}}{D^{-}}$$

which would give R=1 in the absence of asymmetry. If an average R value is required over many different experimental runs then each of the D^{+} and D^{-} values for each of the individual measurements are added before the R value is calculated.

In a typical experiment each of the δ values are an average of 3 measurements each lasting between 60 to 200 seconds depending on the signal intensity. A single complete experiment then lasts between 12 to 40 minutes. Over this period the pressure in the 10 litre reservoir cylinder does not change significantly.

The analysis presented above does have some flaws which must be clarified. Firstly, since the hexapole on cases are being scaled in order to ensure that the two hexapole off cases are identical (in the adjusted values), it is important that the hexapole off signals are not small and significantly different. Considerable overestimation of adjusted values could be obtained under these circumstances e.g., if $\delta+_{0} = 5$ and $\delta-_{0} = 10$, then the $\delta+_{kV}$ value would be doubled to give the corrected $\delta^{a}+_{kV}$ value.

The second flaw can occur when one of the hexapole off differences has an extraneous count from higher than usual residual fields or electrical abnormalities. This would again cause overestimation of the adjusted values during the analysis.

Each of these possible errors was assessed during each analysis of the recorded results and the development of two selection criteria were formulated.

The first criterion was that the ratio of hexapole off differences ($\delta+_0$ and $\delta-_0$) not exceed 1.4 which does not preferentially select any desired asymmetry and is kept constant for all the analyses presented in this dissertation. Before an experiment the homogeneous field plate ground potential bias offset was adjusted (if needed) to give similar beam counts, independent of plate polarity, when the plates are switched to ground potential. If these counts began to differ (i.e. the ratio exceeded 1.4) then it was indicative of a high or low miscellaneous count or that residual fields are interfering with the data collection and that the homogeneous field plates need cleaning.

The second criterion originates from the analysis described above. If the extra count values, D^+ and D^-, are low then, when the G-factor and R value are calculated, any small differences between the values tends to overestimate the G-factor and R values. Similarly, if only one of D^+ or D^- is small then again overestimation can occur in the G-factor and R values. Hence a value of 100 was imposed on the D^+ and D^- values which, if not exceeded, would mean removal of that particular set of measurements. As with the first criteria this does not preferentially select any orientation and is again kept constant throughout each of the following analyses. This criterion does, however, tend to be biased against molecules that have minimal enhancement with hexapole voltage, such as Ar, SF_6, symmetric top molecules where low hexapole voltages are used or for molecules that have generally low signal levels, hence in the analyses presented in the following sections these situations are approximated to no asymmetry effect (G~0 and R~1).

5.2 Amptektron #1 Results

The results here represent the first set of results where consistency between measurements was achieved. The results are presented as averages using two analyses as described in Section 5.1.2. The numerical value for the steric ratio given by the R value provides the most simple physical picture of the ionisation asymmetry as it provides a direct ratio for the number of extra counts obtained from each end of the oriented molecule and so indicates the relative ionisation probability for electron impact on each end of the molecule.

5.2.1 Experimental

The experimental configuration using the Amptektron MD-501L thermal ion detector is shown in Figure 5.2.1.

The computer is instructed to set the high voltage required on the hexapole at the beginning of an experiment by a 12-bit digital-to-analog converter and custom written

software. The positive and negative supplies are Glassman High Voltage Inc. (EH series) capable up to 30 kV.

The pulse counting controller unit provides the primary trigger for the beam source driver unit and the homogeneous field pulsing unit. The beam source driver unit pulses the nozzle continuously throughout an experiment. The homogeneous field pulsing unit pulses the voltages on the homogeneous field plates with the delay, width and voltage set previously as described in Section 5.1.1. The pulse counting controller unit internally triggers the TTL gates for gate 1 and gate 2 (positioned as in Section 5.1.1) which are then and-gated with the Amptektron signal. The gate 1, gate 2 and the homogeneous field pulsing unit delay and width can be monitored by the oscilloscope. The and-gated signal is counted and displayed on the computer with the averages of gate 1, gate 2 and the difference between gate 1 and gate 2 recorded.

Additionally, the nozzle pressure and the electron current on the electron collector are also recorded. The backing pressure of the nozzle did not vary appreciably over an experimental period (typically the pressure dropped by about 10 torr per 20 minutes), however, between days and different runs it was variable. The reservoir for the beam species was refilled once the hexapole off differences became too small for accurate analysis. The electron current could only be recorded when the nearest homogeneous field plate to the electron gun was pulsing or when both homogeneous field plates were at ground. When the far homogeneous field plate was pulsing the electron current on the collector was too unstable as measured by the Keithley 486 picoammeter. Any effect on the asymmetry of electron impact ionisation because of the deformations in the electron beam caused by the pulsing of the homogeneous field plates should be accounted for in the analysis presented in Section 5.1.2 which accounts for the usual electron current normalisation.

Nozzle	frequency = 10 Hz, width = 1.2 ms, voltage = 37 V
Nozzle Aperture	diameter = 70 μm
Nozzle-skimmer Distance	17.5 mm (250 nozzle diameters)
Backing Pressure	1600-2200 torr
Hexapole	3-13 kV
HFPU[1]	delay = 3.4 ms, width = 7.0 ms, voltage = +20 V or -20 V
Pulse Counting	gate 1 = 3.5 ms, gate 2 = 9.9 ms, gate width = 0.3 ms
Count Time	average of 3 counts each of 100 s
Electron Energy	200 eV

[1] Homogeneous Field Pulsing Unit

Table 5.2.1: Experimental Conditions and Settings for CH_3Cl using the Amptektron MD-501L thermal ion detector.

For CH_3Cl the general experimental settings are shown in Table 5.2.1. For other molecules the gate 1 position and homogeneous field pulsing unit delay were adjusted

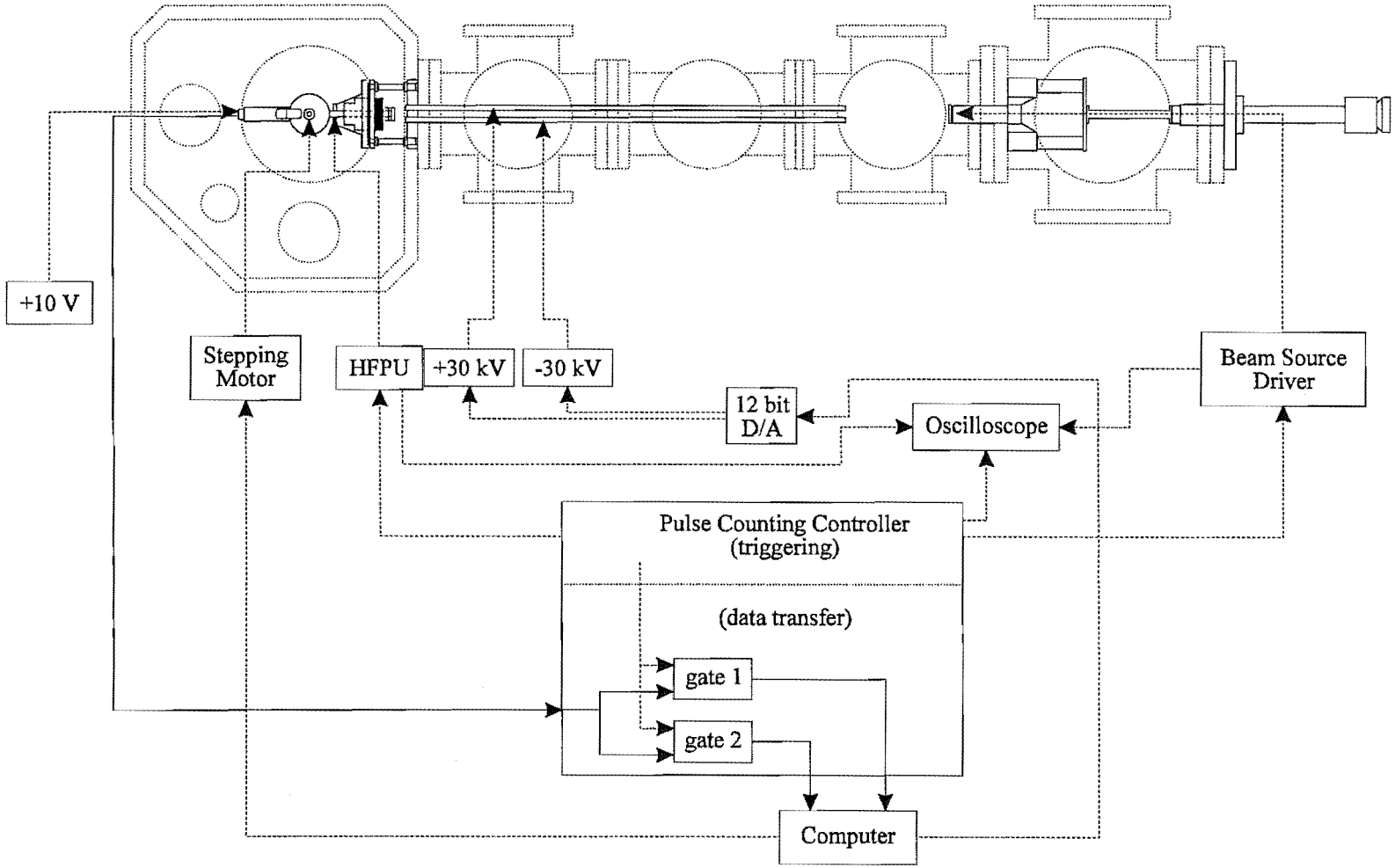

Figure 5.2.1: Experimental arrangement for the collection of data in an electron impact ionisation asymmetry experiment using the Amptektron MD-501L thermal ion detector.

according to the flow velocities.

The measurements in this period ranged over various hexapole voltages at a set electron energy. The pulsing of the homogeneous field plates was primarily from a +20V potential to ground potential while the other plate remained at ground. The -20V potential was also used in some cases to verify that any asymmetry was not dependent solely on the electric field direction. Once it was established that the negative supplies gave qualitatively identical results as the positive supplies only the positive supplies were used since it was determined that the negative potentials gave much higher variances in the measured counts. This was attributed to a stronger residual electric field in the scattering volume from the switching of the negative supplies.

5.2.2 Results and Discussion

Each of the data selection procedures described in Section 5.1.2 were applied to each of the results measured. The averages for the G-factor and R value for each molecule studied are shown in Table 5.2.2.

Molecule	Hexapole Voltage	G	R
Ar	10	0.036±0.199	1.04
SF_6	10	~0	~1
CF_3Br	10	-	-
CH_3Cl	3	-	-
	6	-0.069±0.248	1.24
	7	-	-
	8	-0.199	1.50
	9	-0.221±0.123	1.57
	10	-0.269±0.111	1.70
	11	-0.186±0.081	1.50
	11.5	-	-
	12	0.060±0.052	0.90
	12.5	-	-
	13	-	-

Table 5.2.2: Electron impact ionisation asymmetry results using the Amptektron MD-501L thermal ion detector. The results are shown with their respective standard deviation. The dashes (-) represent results that were measured but which did not pass the data selection procedures of Section 5.1.2.

For a spherical molecule, such as Ar and SF_6, no orientation effect is expected hence the G-factor and R value would be expected to be 0 and 1 respectively (for SF_6 in Table 5.2.2 these values have been assigned). The values for argon are near the

theoretically expected results with the large standard deviation indicative of results that are well spread about the mean because of the analysis used for the data. The SF_6 and CF_3Br results, in this case, did not meet the criteria for selection but repeat measurements are discussed in later sections.

The major emphasis during this period was the measurement of the asymmetry towards electron impact ionisation for CH_3Cl. The majority of the measurements were performed with a hexapole voltage of 10 kV as this gave good signal enhancement with hexapole voltage and was stable with fluctuating pressures in the hexapole chambers. The other averages were obtained only over a few measurements to gain a representative value for that hexapole voltage, hence the greater standard deviation for these results.

The CH_3Cl results at 12 kV seem to be an anomaly with these being the only results that indicate no asymmetry effect. Since the 12 kV results are so different from the trend of the surrounding results they will only be mentioned here and will not be related to the other results.

The asymmetry effect for the results from 6 kV to 11 kV are shown in Figure 5.2.2 for the G-factor and R values.

In an ideal case, where electron impact ionisation was required to occur solely at one end of a molecule, it would be expected that the maximum asymmetry towards electron impact ionisation would occur when the molecules are in the highest degree of orientation. For hexapole focusing this occurs at the threshold voltage where ideally $\langle \cos\theta \rangle = -1$. As the hexapole voltage is increased above the threshold other quantum states, not so well oriented, are ionised and so the asymmetry effect will decrease as the molecules become more broadside. A continued increase of the hexapole voltage will finally give an average degree of orientation which does not vary with any further increases in hexapole voltage and so the asymmetry will reach an equilibrium value somewhere between the threshold value and the value when there is no effect.

In the present experimental conditions, however, with no beam stop and large hexapole exit aperture, there is no state selection. Additionally there will be an ensemble of states that will be ionised at the threshold voltage that would otherwise not be ionised in the ideal case. In this situation these states would give a baseline asymmetry effect which, depending on the signal levels, would override any threshold asymmetry effect. As more molecules are focused (hexapole voltage increased) the signal level would also increase beyond the baseline signal level and so would tend towards the ideal case.

For the CH_3Cl results presented in Figure 5.2.2 it is difficult to determine whether the asymmetry effect reaches an optimum value. If the 6 kV values are ignored because of the high standard deviation then the remaining four average values tend to reach an optimum value around 10 kV. However, considering the standard deviation of each value, the average values could also be considered equal. Combining the results for 8, 9, 10 and 11 kV the average G-factor and R value become

$$G = -0.234 \pm 0.099, \; R = 1.62.$$

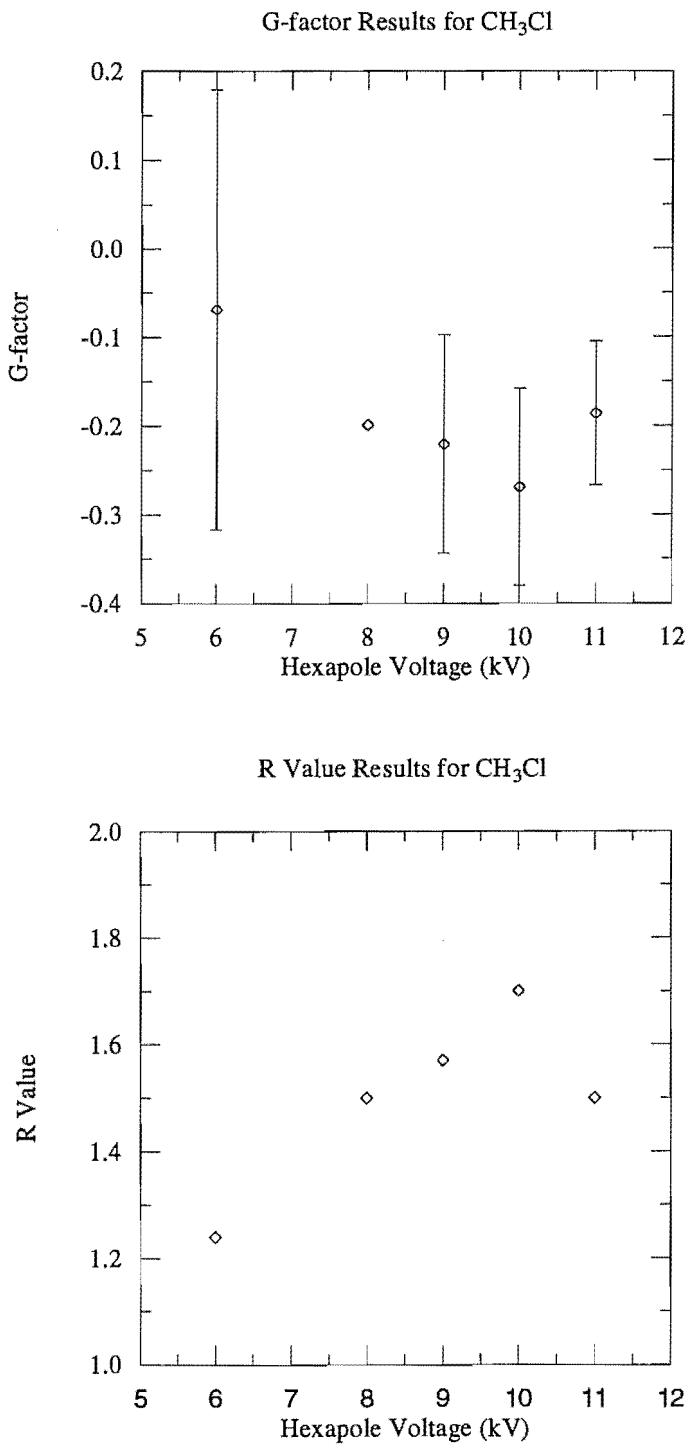

Figure 5.2.2: Electron impact ionisation asymmetry G-factor and R value results for CH_3Cl using Amptektron MD-501L thermal ion detector. A G-factor of 0 or R value of 1 indicates no asymmetry effect. The error bars represent one standard deviation.

5.2.3 Conclusion

The asymmetry effect of electron impact ionisation on the CH_3-end and Cl-end of CH_3Cl has been demonstrated. Ionisation probability at the CH_3-end of the molecule seems to be about 1.6 times greater than the Cl-end. The asymmetry effect possibly shows some dependence on the hexapole voltage used but, with the present experimental configuration, any trend cannot be reliably confirmed without further study.

5.3 Quadrupole Mass Spectrometer Results

Section 5.2 showed that there was an asymmetry effect towards electron impact ionisation for CH_3Cl. However the Amptektron MD-501L thermal ion detector was unable to determine any similar effects for other symmetric top molecules because of inadequate signal levels resulting from the inherently lower detection efficiency for heavier molecules.

The Vacuum Generators SXP-300 Quadrupole Mass Spectrometer was subsequently used as the detector with the commercial ion source replaced by an ion lens assembly. The ion lens element voltages were adjusted to give the maximum ion transmission without affecting the homogeneous electric field within the scattering volume using electric field and ion trajectory calculations as a guide (Figure 3.3.13). The quadrupole mass spectrometer provided greater specificity for product ion detection and was used continuously until unresolved problems with the electron multiplier and signal line were encountered.

5.3.1 Experimental

The experimental configuration is shown in Figure 5.3.1 for the quadrupole mass spectrometer. The timing sequences and control of the nozzle, hexapole voltage and homogeneous field plate voltage are the same as described in Section 5.2.1. The only difference between Section 5.2 and here is the detection of ions, the pulse handling and the hexapole rod dimensions.

The output pulses from the channeltron electron multiplier are passed through a 2 MHz notch filter, to eliminate radio-frequency pick-up from the quadrupole driver circuitry. They are then amplified by a fast pre-amplifier followed by an amplifier and pulse discriminator combination to give near +5 V TTL output pulses. The output pulses are input to the pulse counting controller where they are and-gated and pulse counted as in Section 5.2.1.

Between this period and the previous section of Amptektron results the hexapole rod mounts were changed to the smaller inscribed radius mounts. The inscribed radius, r_o (see Section 2.4.3), was reduced from 7.5 mm to 6.0 mm giving a 1 mm separation between adjacent hexapole rods. To obtain the same electric field strength ε with the smaller mounts a hexapole voltage of 5.5 kV must be used to correspond to 11 kV with the larger mounts (r_o^3 dependency).

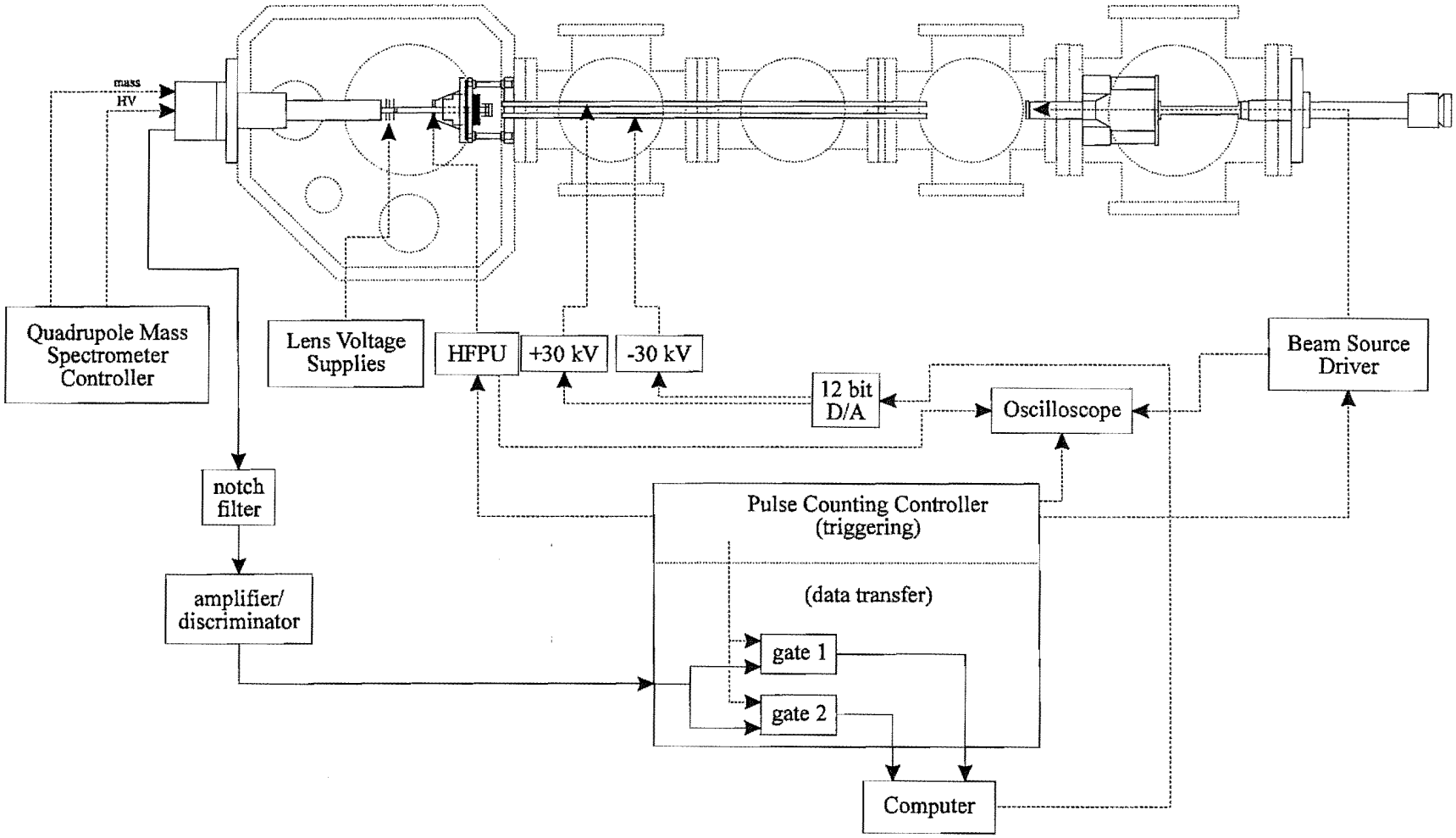

Figure 5.3.1: Experimental arrangement for electron impact ionisation asymmetry experiments using the Vacuum Generators SXP300 quadrupole mass spectrometer.

Nozzle	frequency = 10 Hz, width = 1.2 ms, voltage = 37 V
Nozzle Aperture	diameter = 70 μm
Nozzle-skimmer Distance	17.5 mm (250 nozzle diameters)
Backing Pressure	1000-1500 torr
Hexapole	5.5 kV
HFPU[1]	delay = 3.4 ms, width = 7.0 ms, voltage = +20 V or -20 V
Pulse Counting	gate 1 = 3.5 ms, gate 2 = 9.9 ms, gate width = 0.3 ms
Count Time	average of 3 counts each of either 100 or 200s
Electron Energy	150 eV or 200 eV
Electron Multiplier HV	2.1-2.3 kV

[1] Homogeneous Field Pulsing Unit

Table 5.3.1: Experimental Conditions and Settings for CH_3Cl using Quadrupole Mass Spectrometer.

The ion lens voltages were not pulsed. The element nearest the scattering volume was maintained at -100 V which was determined to be the maximum voltage that could be applied to keep the homogeneity of the electric field in the scattering volume (see Section 3.3.10.1 and Figure 3.3.13). The other three lens voltages were set externally and optimised for maximum ion counts before an experiment. The mass control and the channeltron electron multiplier high voltage were the only components controlled from the mass spectrometer controller and were again set before taking measurements. When a channeltron analogue signal was collected directly, such as for an arrival time distribution, then the internal signal sensitivity amplifier on the mass spectrometer controller was also used to amplify the signal for presentation to the Thurlby DSA524 digital storage oscilloscope.

The experimental operating conditions are shown in Table 5.3.1 for CH_3Cl. As in Section 5.2.1 slight adjustments to the gate 1 position, homogeneous field pulsing unit delay and mass were necessary for other molecular species.

5.3.2 Results and Discussion

Originally the quadrupole mass spectrometer was going to be used for the study of a range of symmetric top molecules to obtain a general comparison for the asymmetry effect over various different oblate and prolate symmetric top molecules. However, this aim was side-tracked somewhat once the asymmetry of the CH_3^+ fragment ion from CH_3Cl was measured since it gave a markedly different result compared to the molecular ion.

Over the course of this period emphasis was initially placed on the asymmetry of electron impact ionisation to form the CH_3Cl molecular ion and the CH_3^+ fragment ion from CH_3Cl with additional measurement of the asymmetry of CH_3Br, CF_3Br and $CHCl_3$

also being achieved but to a lesser degree. The results for each of the molecules are shown in Table 5.3.2.

Molecule	Ion Detected	Electron Energy	G	R
Ar	Ar^+	200	0.004	0.99
CH_3Cl	CH_3Cl^+	150	-	-
	CH_3Cl^+	200	-0.476±0.117	2.80
	CH_3^+	200	0.017±0.033	0.96
CH_3Br	CH_3Br^+	200	-	-
	CH_3^+	200	-	-
CF_3Br[1]	CF_3^+	200	-0.219±0.219	1.80
$CHCl_3$	$CHCl_2^+$	200	-0.170±0.082	1.36

[1] Results for 6.0 and 5.5 kV combined.

Table 5.3.2: Electron impact ionisation asymmetry results using the quadrupole mass spectrometer. The results are shown with their respective standard deviations. The dashes (-) represent results that were measured but which did not pass the data selection procedures of Section 5.1.2.

As in Section 5.2.2 the results for Ar agree with the theoretically expected result. This result gives confidence that electric field conditions were similar to that of the Amptektron #1 results of Section 5.2. The low signal intensity encountered at 150 eV resulted in no comparison able to be made between these measurements and measurements at 200 eV. The effect of electron energy on the asymmetry effect is studied further in Section 5.4.

The following discussion only concerns those results for the symmetric top molecules CH_3Cl, CH_3Br, CF_3Br and $CHCl_3$ recorded at 200 eV. The discussion has been divided into two sections: one based on CH_3Cl and CH_3Br and the other based on CF_3Br and $CHCl_3$. It should be noted that only relative trends can be discussed at the present time as any definitive analysis must be left until more accurate results are obtained.

5.3.2.1 CH_3Cl and CH_3Br

CH_3Cl and CH_3Br were both studied in relation to formation of both the molecular ion and the CH_3^+ fragment ion since, for CH_3Cl, the two ions gave markedly different asymmetry results.

The molecular ion result for CH_3Cl indicated a large asymmetry effect which is over two standard deviations from the theoretical null effect value. The electron impact ionisation of CH_3Cl, to form the molecular ion, is about 2.8 times more likely to occur if the electron impinges on the positive CH_3-end of the molecule, than on the negative Cl-end.

The asymmetry results for the electron impact ionisation of CH_3Br to form the molecular CH_3Br^+ ion unfortunately give no results that fulfil both of the data selection procedures. The results prior to the selection procedures for CH_3Br^+ were G=-0.085±0.117, R=1.21 and for CH_3^+, from CH_3Br, G=0.103±0.542 and R=1.04. These results indicate that the asymmetry effect is much smaller for CH_3Br than CH_3Cl. Although the standard deviation is large for CH_3Br the mean G-factor and R value indicate that electron impact on the positive CH_3-end is again slightly more favourable than electron impact on the negative Br-end.

For the CH_3X family, where X=F, Cl, Br or I, the molecular ion is the base peak in the mass spectrum. However, in changing from a Cl atom to a Br atom the asymmetry effect seems to have been reduced by half. Possible reasons for the difference in the asymmetry effect for the two molecules could range from a lesser degree of orientation for the more prolate CH_3Br making the positive CH_3-end more accessible, to electrostatic differences in electron affinity, dipole moment and polarisability causing there to be a greater probability for the pulsed disturbance generated by the passage of the bombarding electron causing an electronic transition and ionisation. Based on two average measurements, one of which has large standard deviation, a complete explanation can not be determined without a more detailed series of studies for the CH_3X family.

Possibly the most unexpected comparative aspect of the asymmetry effect for CH_3Cl was the vastly different result for the CH_3^+ fragment ion compared to the formation of the molecular ion. For both CH_3Cl and CH_3Br the results indicate that there is no preference to either orientation when the CH_3^+ ion fragment is formed from electron impact ionisation. Consideration must be given to whether this asymmetry effect is real or an effect due to the fragmentation process itself.

The fragmentation process is a rapid process occurring in much less than a rotational period such that the CH_3^+ ion would be ejected towards the positive homogeneous field plate. Since the homogeneous field plates are kept with a slight residual potential on the plates, to prevent any rapid switching of the electric field direction, the CH_3^+ ion will experience a slight positive potential as it approaches the positive homogeneous field plate which will deflect the CH_3^+ ion radially about the plate.

When the hexapole is off the detector counts the same number of ions no matter what the field polarity (otherwise the results would not be passed by the selection procedures of Section 5.2.2) and so the detection efficiency is the same for each orientation. If CH_3^+ did have a three-fold asymmetry effect similar to the molecular ion, then it would be expected that this increase would still be detected since the ions are radially deflected and the detection efficiency for each orientation is equal. Since the asymmetry effect is not apparent it indicates that only molecules that are in both orientation distributions can contribute to the CH_3^+ ion signal. Hence, only molecules that are sideways oriented (or near sideways) are ionised and fragment to give CH_3^+.

5.3.2.2 CF_3Br and $CHCl_3$

For CF_3Br and $CHCl_3$ the CF_3 and the CCl_3-groups are the negative ends of the electric dipole. Both molecules indicate that electron impact ionisation, for formation of the CF_3^+ and $CHCl_2^+$ ion fragments, is more efficient when the electron impinges on the positive Br-end or H-end of the molecule respectively.

In the previous section, where the CH_3^+ fragment ion formed from the dissociation of CH_3Cl^+ was discussed, the incident electron was argued to interact with the molecule in a broadways orientation. If this is universal then it may be anticipated that it would be required that the C-Br bond or the C-Cl bond be near perpendicular to the electron beam to form the fragment ions.

For CF_3Br it would be expected that the asymmetry effect would be similar to the CH_3Cl and CH_3Br cases for formation of CH_3^+. However, the asymmetry R values for CH_3^+ is about 1, for both CH_3Cl and CH_3Br, while that for the formation of CF_3^+ is about 1.8 which indicates that a simple broadside explanation is not sufficient. For CH_3Cl electron impact was favoured on the positive end of the molecule to form CH_3Cl^+. For CF_3Br there is no molecular ion formed, but it would still be reasonable to expect that the positive end of the molecule may be more favourable to form an excited molecular ion $(CF_3Br^+)^*$. Since no molecular ion channel is available this excited state may fragment to the CF_3^+ fragment ion which would vary the asymmetry effect measured towards a preference to the positive end of the molecule.

For formation of $CHCl_2^+$ from $CHCl_3$ there are three C-Cl sites which electron impact ionisation and fragmentation can occur. An explanation similar to the CF_3Br case above could also explain the slight preference for electron impact at the positive end of the $CHCl_3$ molecule

5.3.3 Conclusion

The quadrupole mass spectrometer has provided the opportunity to explore the asymmetry effect for electron impact ionisation and fragmentation. For CH_3Cl, there is a large asymmetry effect for formation of the molecular ion with the positive CH_3-end being 2.8 times more probable than the negative Cl-end. To form the molecular ion for CH_3Br the asymmetry effect is reduced but still favours the positive CH_3-end. For both CH_3Cl and CH_3Br there is no asymmetry effect for formation of the CH_3^+ fragment ion which indicates that a broadside orientation of the molecule is favoured. Electron impact ionisation of CF_3Br and $CHCl_3$, to form the fragment ions CF_3^+ and $CHCl_2^+$ respectively, also indicate an asymmetry effect with preference for electron impact at the positive end of the molecules but to a lesser extent than for CH_3Cl.

5.4 Amptektron #2 Results

These experiments, using the Amptektron MD-501L particle detector, were carried out to determine whether there was any effect of electron energy (wavelength) on the asymmetry effect of electron impact ionisation.

5.4.1 Experimental

The experimental configuration, triggering sequence and data collection are the same as for Section 5.2.1 and Figure 5.2.1. For this section some new components were used compared with the first set of results obtained with the Amptektron in Section 5.2. A new nozzle was installed, still retaining the 70 μm diameter aperture, which required a higher external voltage for pulsing and which seemed to introduce an extra delay in the arrival time profile of CH_3Cl and hence, a further delay in the gate 1 position and the homogeneous field pulsing unit delay. During this period the smaller hexapole mounts were also used as detailed in Section 5.3.1.

The experimental settings for the results described in this section are shown in Table 5.4.1.

Nozzle	frequency = 10 Hz, width = 1.4 ms, voltage = 46 V
Nozzle Aperture	diameter = 70 μm
Nozzle-skimmer Distance	17.5 mm (250 nozzle diameters)
Backing Pressure	1300-2000 torr
Hexapole	5.5 kV
HFPU[1]	delay = 3.8 ms, width = 7.0 ms, voltage = +20 V or -20 V
Pulse Counting	gate 1 = 3.9 ms, gate 2 = 9.9 ms, gate width = 0.3 ms
Count Time	average of 3 counts each of 60 s
Electron Energy	100 eV, 150 eV, 200 eV and 240 eV

[1] Homogeneous Field Pulsing Unit

Table 5.4.1: Experimental Conditions and Settings for CH_3Cl using the Amptektron MD-501L thermal ion detector.

5.4.2 Results and Discussion

The data collected for CH_3Cl during this period were for a fixed hexapole voltage of 5.5 kV for four electron energies: 100, 150, 200 and 240 eV. On each change of the electron energy the electron gun optics were optimised for maximum beam current (see Section 3.3.9) when the homogeneous field plates were grounded. Application of the data selection procedures, described in Section 5.1.2, gave the results shown in Table 5.4.2 which are shown graphically in Figure 5.4.1 for the G-factor and R value averages respectively.

It is difficult to predict the theoretical effect of electron energy on any asymmetry towards electron impact ionisation (Section 2.3). Experimental ionisation cross sections tend to go through a maximum around 50-100 eV and then begin to decrease as a result of diminishing frequency components in resonance with the energy change of the molecule as the electrons become faster and the wavelength decreases [Field 1957]. However, this does not necessarily mean that the asymmetry effect measured will follow

an identical trend. Assuming that each end of the molecule has a different ionisation cross section curve (i.e. different ionisation thresholds and curve shape which combine to give the experimentally determined curve for random molecules) then it is possible that at higher electron energies the ionisation cross sections, for each end, could decrease at different rates and so give an increasing asymmetry effect. In this discussion it is assumed that each end of the molecule can be represented by an individual ionisation cross section. In this case the region close to the threshold would theoretically give the greatest asymmetry effect. Below some electron energy, only one end of the molecule would produce ions. For the experimental conditions described in this dissertation electron energies near threshold were inaccessible because of the low signal intensity at low electron energies.

Molecule	Electron Energy	G	R
CH_3Cl	100	-0.106±0.012	1.24
	150	-0.153±0.115	1.36
	200	-0.101±0.081	1.23
	240	-0.182±0.114	1.45

Table 5.4.2: Electron impact ionisation asymmetry results using the Amptektron MD-501L thermal ion detector. The results are shown with their respective standard deviations.

From Figure 5.4.1 it is uncertain as to whether there is an effect on the asymmetry with increasing electron energy. The general trend seems to be a slightly increasing mean asymmetry effect with increasing electron energy however, as with the hexapole voltage effect of Section 5.2.2, further experiments are required in order to decrease the standard deviation and to obtain a more accurate mean value. Combining the results of Table 5.4.2 for 100, 150, 200 and 240 eV give averages for the G-factor and R value of

$$G = -0.134 \pm 0.100, R = 1.32$$

5.4.3 Conclusion

The effect of electron energy on the asymmetry of electron impact ionisation is, at this time, inconclusive without further experimental study. With the experimental conditions used in these studies the CH_3-end of CH_3Cl is about 1.3 times more reactive than the Cl-end. The results are consistent with there being greater probability for ionisation when the electron is incident on the CH_3-end of the molecule as measured in the previous two sections.

5.5 General Discussion

Each of the results presented in the previous three sections have been consistent over periods of many months. However, the results of each section must be shown to be

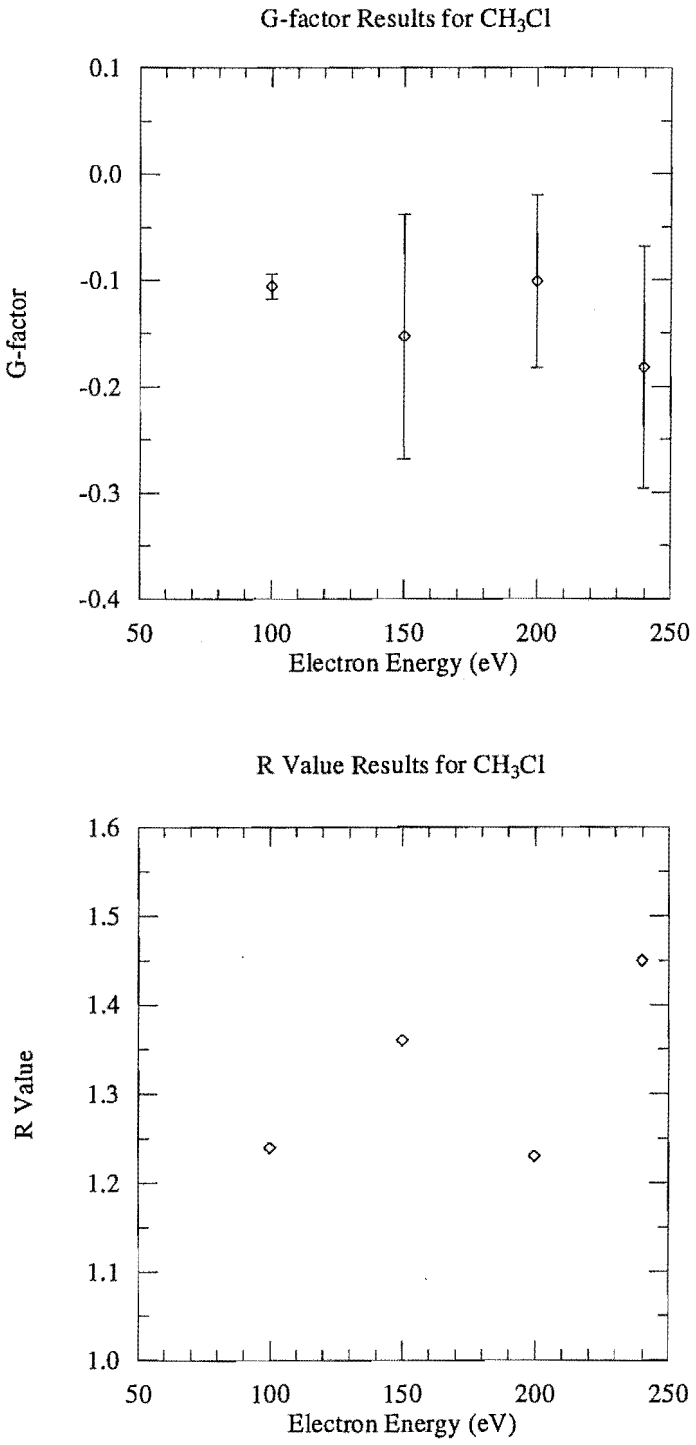

Figure 5.4.1: Electron impact ionisation asymmetry G-factor and R value results for CH_3Cl using the Amptektron MD-501L thermal ion detector. A G-factor of 0 or R value of 1 indicates no asymmetry effect. The error bars represent one standard deviation.

self consistent. In this section the results are reviewed in regard to their consistency with various experimental conditions and detector type. Before any comparative analysis is made the experimental tests that were used to verify that the asymmetry effect measured was a true effect are described.

5.5.1 System Tests

With electric fields switching to near ground potential and possible electric field penetration from high voltage sources there was reason for speculation that the asymmetry effect measured could be an electrical artefact originating from the experimental configuration. The development of the scattering volume (Section 3.3.11) was designed to reduce electric field penetration however, this did not guarantee that one of the field polarities, when the field was switched to ground potential, was being favoured above the other polarity. To this regard experimental tests were performed which would verify the asymmetry effect.

Theoretically the simplest test would be to change the homogeneous field voltage from +20 V to -20 V. This would still provide the same homogeneous electric field strength within the scattering volume and so should give the same asymmetry effect if the effect is independent of the voltage that is switched on the homogeneous field plates. As mentioned in the previous sections the consistency of the counts when the negative polarities were used was poor resulting in very few measurements passing the two selection criteria. Combining the results that did pass the selection criteria for the Amptektron #1 and #2 experimental configuration for CH_3Cl gave an average G-factor and R value of

$$G = -0.288 \pm 0.337$$

$$R = 3.43.$$

If the selected measurements from Section 5.2 and 5.4 for the positive supplies were combined then the average G-factor and R value would be

$$G = -0.162 \pm 0.111$$

$$R = 1.47.$$

The absolute averages for the two polarities do not agree, however, the main priority for the negative polarity tests was to confirm that the symmetry ratio sign did not change i.e. that the asymmetry ratio still predicted that the positive CH_3-end of CH_3Cl remained more favourable than the negative Cl-end.

In analogous CH_3Cl experiments, using the quadrupole mass spectrometer, the mass 50 raw results again indicated the positive CH_3-end was more favourable, however, no result satisfied the selection criteria. For the formation of the CH_3^+ fragment ion using the negative polarities only one result satisfied the selection criteria with a G-factor of -0.012 and R value of 1.02 which agreed with the previous results showing no

asymmetry effect for CH_3^+. Additional experiments were performed with $CHCl_3$ forming $CHCl_2^+$ which gave average raw results of

$$G = -0.186 \pm 0.128$$

$$R = 1.44$$

which agreed with the results of Section 5.3.2 using the positive supplies.

To test whether the asymmetry effect was dependent on the electric fields within the scattering volume two spherical top molecules, Ar and SF_6, were used which would show no orientation dependence and so should show no asymmetry effect under similar experimental conditions used for the CH_3Cl experiments. As shown in sections 5.2.2 and 5.3.2, the G-factors and R values for argon using the Amptektron and quadrupole mass spectrometer were G=0.036, R=1.04 and G=0.004, R=0.99 respectively. These values were measured over a range of experimental conditions and show no asymmetry effect which indicates that the asymmetry effect measured for CH_3Cl is a property of the molecule and not an electric field anomaly. The results for SF_6 are indicative of the problems encountered with the analysis in that the signal enhancement with hexapole voltage is insignificant. For SF_6 the extra counts are 17 and 21 which are virtually identical (for total counts of around 520) but which give an anomalous R value of 0.8 due to the small signals involved. The mass 15 results for CH_3Cl also indicate that the asymmetry effect is real as nothing in the scattering volume has changed yet the asymmetry effect for CH_3^+ and CH_3Cl^+ are different.

A more sophisticated test of the asymmetry result was to reset the homogeneous field switching delay in advance of the gate 1 position. The ions counted by gate 1 would not have experienced an orienting field and so could not be oriented. This experiment is similar to other groups [Kasai 1993, Bowering 1994] who use a homogeneous guiding electric field to guarantee adiabatic transitions from the hexapole inhomogeneous electric field. By switching the guiding field off the selected molecules do not make adiabatic transitions and so are not oriented. In a series of measurements with CH_3Cl the delay time for the switching of the homogeneous field was set 1.0 ms in advance of the gate 1 time. The average values obtained for the G-factor and R value for CH_3Cl were

$$G = 0.008 \pm 0.122$$

$$R = 0.98.$$

These results indicate that the asymmetry effect is only apparent when the CH_3Cl molecule has experienced the orienting field.

These asymmetry tests give confidence that the results discussed in the previous sections are a true molecular orientation effect and not an electrical or detector induced effect.

5.5.2 Comparative Analysis

Until now each of the data collection periods described in Sections 5.2, 5.3 and 5.4 have been considered as completely separate with no correspondence between each of the periods (apart from the discussion on the negative plate polarities of Section 5.5.1). However, since for each of the periods the measurement and experimental configuration are similar then there must be consistency between the periods for completeness of the results.

The two Amptektron series of experiments were performed with different hexapole geometries. The first set (Section 5.2) involved a larger hexapole radius and included measurements of the effect of hexapole voltage on the asymmetry effect. The second set (Section 5.4) involved a smaller hexapole radius and included measurements of the effect of electron energy on the asymmetry effect. For both sets the trends in the asymmetry effect were deemed independent of the variable within experimental error and an average G-factor and R value were evaluated which are shown in Table 5.5.1.

Result Set	G	R
Amptektron #1	-0.234	1.62
Amptektron #2	-0.134	1.32

Table 5.5.1: Combined G-factor and R value results for the two sets of Amptektron experiments for CH_3Cl.

For electron impact ionisation both periods indicate that the CH_3-end of CH_3Cl is favoured over the negative Cl-end with the Amptektron #2 results showing less of an effect than the Amptektron #1 results. By reducing the hexapole radius it is possible that this has also reduced the acceptance angle that is allowed for successful transmission along the hexapole rods (see Section 2.4.4.2). If this was the case then there would be molecular species that are transmitted with the larger hexapole radius but which would hit the rods with the smaller hexapole radius. The on axis direct beam signal, including those molecules with $\cos\theta = 0$, would be unaffected. Hence, the smaller hexapole radius will transmit a distribution with a different degree of orientation, than the larger hexapole radius, which could then result in a different experimentally measured asymmetry effect.

A comparison between the quadrupole mass spectrometer asymmetry results and the Amptektron #2 asymmetry results are shown in Table 5.5.2.

The quadrupole mass spectrometer asymmetry results for CH_3Cl provided the most accurate results over the three periods with the smallest standard error. If these are assumed to be accurate and taking mass spectra data for CH_3Cl fragmentation pattern as m/z(50)=100 and m/z(15)=54 then the following equalities can be written

Result Set	Ion Detected	G	R
QMS[1]	CH_3Cl^+	-0.476	2.80
QMS[1]	CH_3^+	0.017	0.96
Amptektron #2	-	-0.134	1.32

[1] Quadrupole Mass Spectrometer.

Table 5.5.2: Combined G-factor and R value results for the quadrupole mass spectrometer and Amptektron #2 experiments for CH_3Cl.

$$R_{50} = \frac{D_{50}^+}{D_{50}^-} = 2.80$$

$$R_{15} = \frac{D_{15}^+}{D_{15}^-} = 0.96$$

$$D_{50}^+ + D_{50}^- = 100$$

$$D_{15}^+ + D_{15}^- = 54$$

where 50 and 15 represent the masses of the molecular and fragment ions respectively and the D symbols are those used in Section 5.1.2. Rearranging the four equations gives an expected R value for the Amptektron results of

$$R = \frac{D_{50}^+ + D_{15}^+}{D_{50}^- + D_{15}^-} = 1.89.$$

This analysis predicts that the Amptektron result for R should be lower than the quadrupole mass spectrometer result, as observed.

5.5.3 Conclusion

In this section the experimental measurements used to verify the asymmetry effect have been described. The measurements support the asymmetry effect as a true effect and not an experimental anomaly.

The comparative analysis presented in Section 5.5.2 show that the asymmetry results from the three different periods are in agreement. It should be noted that although the experimental configuration may be identical the different detectors do have different detection efficiencies and the components of the scattering volume are continuously changing their characteristics with respect to cleanliness and electric charging effects, which can influence the experimental measurements.

5.6 Electron Impact Ionisation Model

As mentioned in Section 2.3, there is no simple model at present which adequately describes all aspects of the electron ionisation process: threshold behaviour, total ionisation cross-section, energy dependence of the cross-section, and fragmentation, in terms of simple equations that could be used confidently in a predictive manner. Investigation of the electron impact ionisation of spatially oriented molecules was initiated in order to extend the work on electron transfer, gain a deeper insight into the electron ionisation process and to provide data useful for the development of semi-empirical models of practical value. The investigation of electron ionisation is clearly in the early stages in comparison with the electron transfer studies and additional work of the influence of orientation on fragmentation will be required before a coherent pattern emerges and a model for fragmentation can be attempted.

5.6.1 Theoretical Model

A simple model [Harland 1995] which considers ionisation in terms of the Coulomb potential developed between the electron and the polar molecule and the electron transition probability reproduces the main experimental features. This model accounts qualitatively for the asymmetry effect measured and leads to simple, generally applicable, expressions for the maximum (70 eV) ionisation cross-section.

As the electron approaches the molecule an electric field is established which is described in terms of a Coulomb potential, ϕ_C. It is assumed that when the Coulomb potential reaches the electron transition energy (the ionisation potential, E_0) the orbital electron involved in the transition absorbs from the field with the efficiency of the ionisation depending on the transition probability, P_i. Neglecting the electron-induced dipole, a cross-section, σ_C, can be calculated from the interparticle separation when $\phi_C = E_0$. In order to find the maximum ionisation cross-section, σ_i, σ_C must be multiplied by the transition probability P_i:

$$\sigma_i = \sigma_C P_i .$$

The target molecule is considered in terms of the isolated electron involved in the transition, charge q, and a charge, q", determined by the dipole moment of the molecule and its orientation with respect to the electron projectile. If the molecule is non-polar then q" = 0, and the electron is considered to be incident on a molecule exhibiting zero charge (electrically neutral), if the molecule has a permanent dipole moment μ and separation of charge centres l, then $q" = \pm\mu/l$, depending on the orientation of the dipole with respect to the projectile electron. The length of the dipole, l, for prolate and oblate symmetric top molecules, CY_3X, is taken as the distance along the C-X molecular axis between the centre of atom X and the Y atom plane perpendicular to the C-X axis. So, the magnitude of the effective Coulomb potential as a function of the electron-molecule separation depends on spatial orientation according to the following cases:

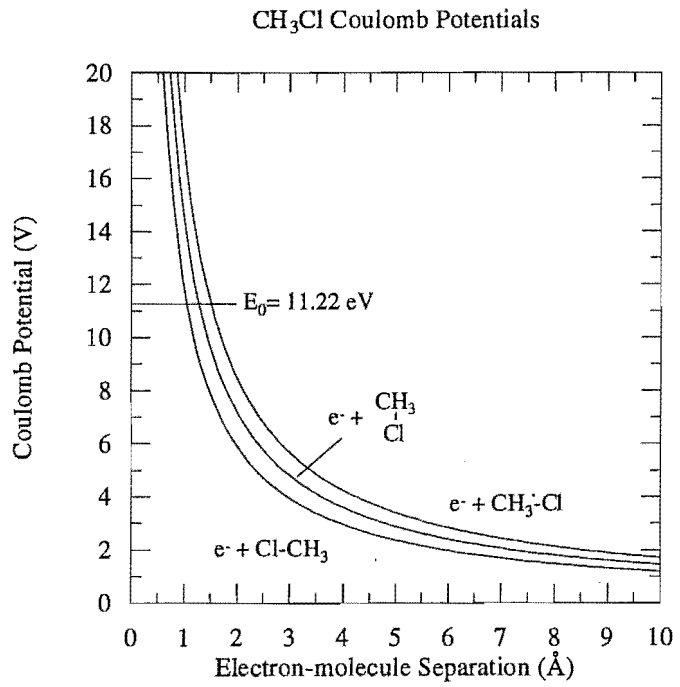

Figure 5.6.1: Coulomb potentials for CH_3Cl when electron approaches for each orientation. Curves have been plotted from Equations 5.6.1, 5.6.2 and 5.6.3.

- zero dipole moment or the dipole perpendicular to the projectile electron (broadside),

$$\phi_{C,0} = \frac{q_{eff}}{(4\pi\varepsilon_0)\, r} = \frac{q}{(4\pi\varepsilon_0)\, r} \qquad (5.6.1)$$

- as the projectile electron approaches the positive end of the dipole, the field will be higher at a given separation and

$$\phi_{C,\delta+} = \frac{q_{eff}}{(4\pi\varepsilon_0)\, r} = \frac{(q+\mu/l)}{(4\pi\varepsilon_0)\, r} \qquad (5.6.2)$$

- as the projectile electron approaches the negative end of the dipole, the field will be lower at a given separation and

$$\phi_{C,\delta-} = \frac{q_{eff}}{(4\pi\varepsilon_0)\, r} = \frac{(q-\mu/l)}{(4\pi\varepsilon_0)\, r}. \qquad (5.6.3)$$

A plot of the Coulomb potentials for an electron approaching broadside, the CH_3-end ($\delta+$) and the Cl-end ($\delta-$) for CH_3Cl, according to Equations 5.6.1 to 5.6.3, respectively, are shown in Figure 5.6.1. When $\phi_C = E_0$, $r = b_{max}$, where b_{max} is the maximum impact parameter for the electron transition process (ionisation). Then $\sigma_C = \pi b_{max}^2$, where σ_C is the calculated (Coulomb) maximum electron impact ionisation cross-section

$$\sigma_C = \pi\left(\frac{q_{eff}}{(4\pi\varepsilon_0)\,E_0}\right)^2 . \qquad (5.6.4)$$

Substituting the appropriate quantities

$$\sigma_C = 651.3\left(\frac{z_{eff}}{E_0}\right)^2 \text{ in units of Å}^2, \qquad (5.6.5)$$

where $z_{eff} = q_{eff}/q$. The model requires that ionisation is favoured at the positive end of the molecule and this has been observed to be the case for CH_3X and CF_3X, even though the positive end of the dipole corresponds to the CH_3-end for CH_3X and the X-end for CF_3X (see Section 5.3).

Considering CH_3Cl in detail, the dipole moment is 6.24 x 10^{-30} Cm (1.87 D) and the effective dipole length is 215 pm giving the charge on the dipole as ±2.90 x 10^{-20} C or ±0.18q, where q is the electron charge. Using Equation 5.6.5, the ionisation cross-sections for electron impact on the positive CH_3-end, $\sigma_{i,\delta+}$, negative Cl-end, $\sigma_{i,\delta-}$, and broadside, $\sigma_{i,0}$, orientations are calculated to be 7.2, 3.5 and 5.2 Å^2, respectively. So, these equations predict that the ionisation cross-section will be higher for electron impact on the CH_3-end of the dipole, lowest for impact on the Cl-end of the dipole and intermediate for broadside collisions. The calculated asymmetry R value $\sigma_{i,\delta+}/\sigma_{i,\delta-} = 2.1$ is close to the experimental R value of 2.80 for the CH_3Cl^+ ion (Section 5.3) and 1.47 measured using the mass insensitive detector (Sections 5.2 and 5.4 combined). Table 5.6.1 lists the calculated asymmetry values for several polar molecules. For the systems which have been studied experimentally, CH_3Cl is predicted to exhibit the highest steric asymmetry value in accord with experiment.

Molecule	μ (10^{-30} Cm)	l (pm)	R value (calculated)	R value (experimental)
CH_3Cl	6.24	215	2.1	2.8
CH_3Br	6.04	230	1.9	
CH_3I	5.40	251	1.7	
$CHCl_3$	3.37	168	1.6	1.4
$CHBr_3$	3.30	175	1.6	
CF_3Cl	1.67	220	1.2	
CF_3Br	2.17	240	1.3	1.8
HCl	3.60	129	1.8	
NO	0.62	136	1.1	
CO	0.39	121	1.1	

Table 5.6.1: Calculated and experimental asymmetry R values from Equation 5.6.5 and results presented in Section 5.4.

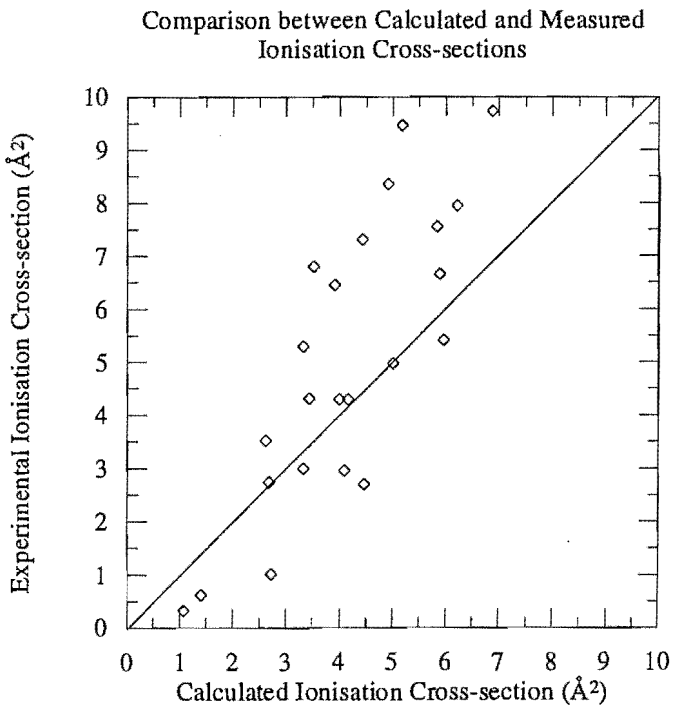

Figure 5.6.2: Comparison between measured ionisation cross-sections and those calculated from Equation 5.6.4.

The experimental electron impact ionisation cross-sections reported in the literature correspond to values for a random orientation of dipoles, $\sigma_{i,r}$. For this model, where $\Delta\phi/\Delta r \approx$constant in the vicinity of $\phi = E_0$, then $(\sigma_{i,\delta+} - \sigma_{i,0}) \approx (\sigma_{i,0} - \sigma_{i,\delta-})$ and $\sigma_{i,r} \approx \sigma_{i,0}$. Despite the simplicity of the model and its obvious limitations, the calculated cross-sections lie within a factor of two of the measured values [Lampe 1957] shown in Figure 5.6.2.

If the transition probability, P_i, is taken to be proportional to $|\mu_{if}|^2$, where μ_{if} is the orbital overlap integral for the dipole transition from state *i* (neutral molecule) to state *f* (ion), then

$$\mu_{if} = \int \psi_i^* \, \tilde{\mu} \, \psi_f \, d\tau$$

where $\tilde{\mu}$ is the electric dipole moment operator. $|\mu_{if}|^2$ is related to the quantum mechanical expression for mean molecular polarisability, α, by [Atkins 1994]

$$\alpha = \frac{2}{3} \sum_f \frac{|\mu_{if}|^2}{E_f - E_i}.$$

Assuming discrete states

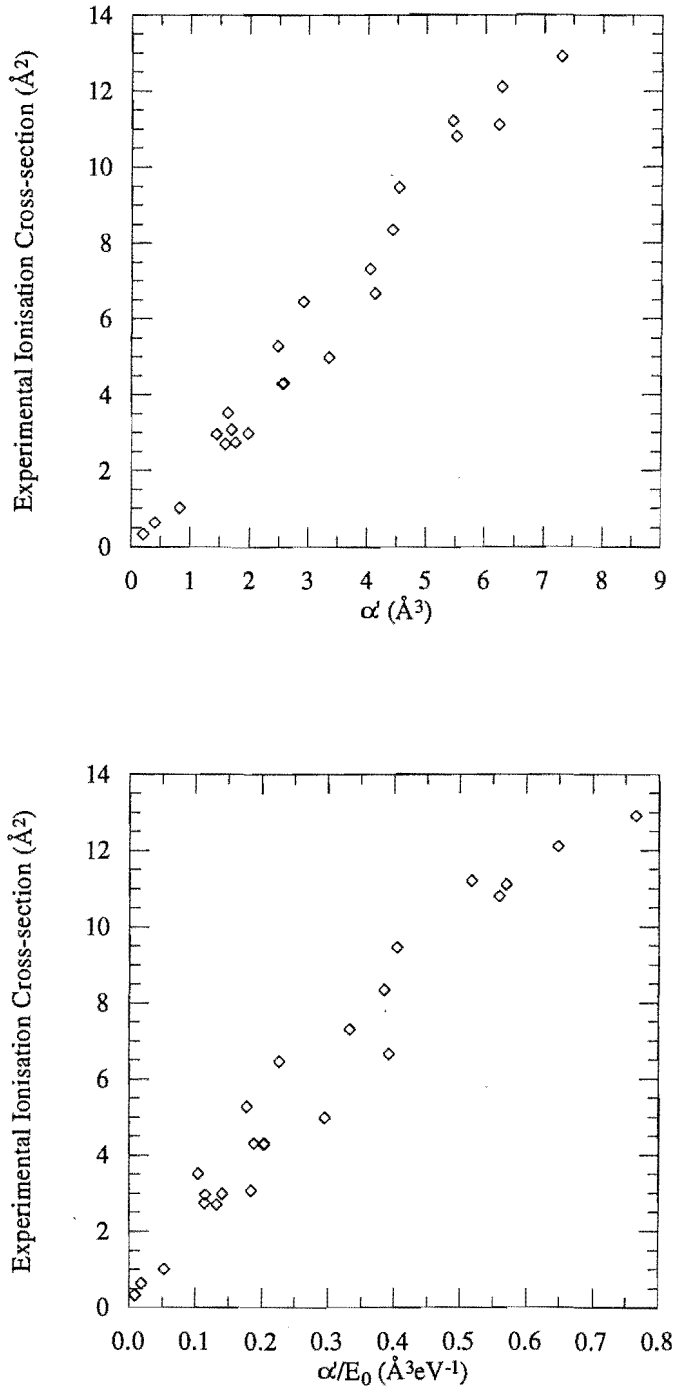

Figure 5.6.3: Correlation between experimental ionisation cross-sections and the polarisability volume (top) and polarisability volume divided by ionisation energy (bottom).

$$P_i \approx |\mu_{if}|^2 \approx \frac{3\alpha E_0}{2} = c\alpha' E_0$$

and

$$\sigma_i = \sigma_C P_i \approx c\, \sigma_C \alpha' E_0$$

where c is a constant, α' is the polarisability volume ($\alpha = 4\pi\varepsilon_0\alpha'$) and ε_0 is the permittivity of free space. Substituting from Equation 5.6.4 for σ_C,

$$\sigma_i = c'' z_{eff}^2 \alpha' / E_0$$

where c'' is a constant. The model predicts the dependence of ionisation cross-section on the polarisability volume first noted by Lampe *et al* [Lampe 1957]. Plots of the experimental 70 eV ionisation cross-sections ($z_{eff} = 1$) reported by Lampe *et al* versus α' and α'/E_0 are shown in Figure 5.6.3. The equations obtained by least squares fitting are:

$$\sigma_i = 1.947\ \alpha' - 0.309 \qquad (5.6.6)$$

$$\sigma_i = 18.79\ \alpha' / E_0 + 0.626 \qquad (5.6.7)$$

where σ_i is expressed in units of Å^2, α' in units of Å^3 and E_0 in eV.

Molecule	σ_C (Å^2) (Equation 5.6.5)	σ_i (Å^2) (Equation 5.6.6)	σ_i (Å^2) (Equation 5.6.7)	σ_i (Å^2) (experimental)
Ar	2.62 (-25.6%)	2.92 (-17.1%)	2.61 (-25.9%)	3.52
N_2	2.68 (-2.6%)	3.14 (14.2%)	2.76 (0.4%)	2.75
CH_4	4.16 (-2.3%)	4.75 (10.5%)	4.53 (5.3%)	4.30
CH_3Cl	5.17 (-45.3%)	8.34 (-11.8%)	8.06 (-14.8%)	9.46

Table 5.6.2: Calculated and experimental maximum ionisation cross-sections.

Table 5.6.2 compares the ionisation cross-sections for Ar, N_2, CH_4 and CH_3Cl calculated from Equations 5.6.5, 5.6.6 and 5.6.7 with the experimental value reported by Lampe *et al* (which are assumed to be accurate). The discrepancies between the calculated and experimental values, shown in parentheses in Table 5.6.2, are well within the uncertainties expected from experimental measurements. The goodness of fit exhibited in Figure 5.6.3, covering a factor of 20 in cross-section, gives some confidence in the model.

Chapter 6

Summary of Results

The purpose of this Chapter is to provide a summary of the results presented in Chapter 4 and Chapter 5 and to offer possible suggestions for future work. Although the conclusions for each section of results throughout Chapter 4 and Chapter 5 have previously been discussed, they are combined here to provide a single summary of the research presented in this dissertation and the significant findings of this research.

In Chapter 4 appearance energies were determined for the van der Waals cluster ions $(CO_2)_n^+$ $(2 \leq n \leq 4)$, $(N_2O)_n^+$ $(2 \leq n \leq 4)$, $(NH_3)_nNH_4^+$ $(0 \leq n \leq 7)$ and the cluster ion fragments $(N_2O.O)^+$ and $(N_2O.NO)^+$ using electron impact ionisation. The appearance energies determined for $(CO_2)_n^+$ $(2 \leq n \leq 4)$, $(N_2O)_n^+$ $(2 \leq n \leq 4)$, $(NH_3)_nNH_4^+$ $(0 \leq n \leq 2)$ and $(N_2O.NO)^+$ were all found to be in general agreement with previously reported values. The appearance energies for $(NH_3)_nNH_4^+$ $(3 \leq n \leq 7)$ and $(N_2O.O)^+$ were determined for the first time. Dissociation energies deduced from the appearance energies for the $(CO_2)_n^+$ and $(N_2O)_n^+$ systems were found to be in general agreement with values obtained by ion-molecule methods. The $(NH_3)_nNH_4^+$ dissociation energies were found to be in considerable disagreement with ion-molecule values indicating that electron impact ionisation measurements fail to sample the true adiabatic ionisation thresholds of these species. The most probable mechanism for the formation of the cluster fragment ions $(N_2O.O)^+$ and $(N_2O.NO)^+$ would appear to involve ionisation and fragmentation of one of the N_2O molecules in the neutral dimer without significant perturbation of the accompanying N_2O molecule, although alternate mechanisms can not be discounted. Measurement of electron impact ionisation efficiency curves provide significant mechanistic information where breaks in the curves are found and where comparisons to monomer measurements and data from other techniques are available.

In Chapter 5 electron impact ionisation of spatially oriented molecules were described and the asymmetry results for a range of symmetric top molecules presented. Before an experiment each variable, nozzle-skimmer distance, electron gun position, gate 1 delay and Amptektron detector position, was optimised (refer Section 3.3.13). Two detectors were used for the measurement of electron impact ionisation asymmetry. An on-axis Vacuum Generators SXP-300 quadrupole mass spectrometer (Section 5.3) and a

rotatable Amptektron MD-501L thermal ion detector (Section 5.2 and Section 5.4). In Section 5.2 the asymmetry effect for CH_3Cl was determined at various hexapole voltages. No trend with increasing hexapole voltage could be accurately determined, however the asymmetry effect consistently demonstrated that the probability for ionisation was greater when the positive CH_3-end was directed towards the electron beam. In Section 5.4 the asymmetry effect for CH_3Cl was determined over a range of electron energies. No trend of the asymmetry effect with increasing electron energy could be accurately determined, however, the asymmetry effect again indicated a greater ionisation probability when the electron beam is incident on the positive CH_3-end of CH_3Cl. In Section 5.3 the quadrupole mass spectrometer was used as the detector which offered a greater range of molecules for study. Electron impact ionisation asymmetry measurements for CH_3Cl (CH_3Cl^+ and CH_3^+ ions), CH_3Br (CH_3Br^+ and CH_3^+ ions), CF_3Br (CF_3^+ ion) and $CHCl_3$ ($CHCl_2^+$ ion) were determined. Each ion studied indicated an asymmetry effect where the positive end of the molecule (CH_3-end for CH_3Cl and CH_3Br, Br-end for CF_3Br and H-end for $CHCl_3$) gave a greater ionisation probability. The results for the CH_3^+ fragment ion from CH_3Cl and CH_3Br gave no asymmetry effect which indicated that a broadside orientation of the molecule is favoured for electron impact ionisation and fragmentation to give the fragment ion. Section 5.5 describes the various experimental tests used to determine that the asymmetry effect was real and not an experimental anomaly. Section 5.5 also combined the results from Sections 5.2, 5.3 and 5.4 to determine the consistency of the results between different detectors and between different data collection periods. Section 5.6 presents a simple model which accounts qualitatively with the asymmetry effect measured and which agrees well with measurements of electron impact ionisation cross-sections over a wide range of molecules.

Work currently being pursued in our laboratory involves the simplification of the electron gun which will reduce the monochromaticity but will provide a greater signal level and more accurate determination of the asymmetry effect. Once a higher accuracy is attainable then possible trends with hexapole voltage, electron energy and a determination of the retention of the asymmetry effect with switching of the homogeneous electric field could be determined. One of the unknowns of any experiment involving oriented molecules is the degree of orientation or the orientation distribution function for the transmitted molecular beam. Experimental determination of the orientation distribution combined with accurate electron impact asymmetry results will provide data useful for the development of theoretical models and will provide a greater insight into the electron impact ionisation process.

Appendix

A.1 Precession of a Symmetric Top Molecule

Euler angles describe the position of the triad of orthogonal vectors a,b,c fixed in a body, relative to the triad of orthogonal vectors x,y,z fixed in space. The motion of the body is known when θ, ϕ, χ are known as functions of time. The motion can also be described by the angular velocity $\omega(t)$, where in the body fixed frame

$$\omega = \omega_a + \omega_b + \omega_c .$$

Hence, expressions are required for each component of angular momentum in terms of the Euler angles and their differentials with respect to time [Zare 1988].

The angular velocity $\dot{\theta}$ along the line of nodes, has components along the a,b,c axis of

$$\dot{\theta}_a = \dot{\theta} \sin\chi$$

$$\dot{\theta}_b = \dot{\theta} \cos\chi$$

$$\dot{\theta}_c = 0.$$

Similarly, the angular velocity $\dot{\phi}$ along the z-axis has components of

$$\dot{\phi}_a = -\dot{\phi} \sin\theta \cos\chi$$

$$\dot{\phi}_b = \dot{\phi} \sin\theta \sin\chi$$

$$\dot{\phi}_c = \dot{\phi} \cos\theta$$

and the angular velocity $\dot{\chi}$ along the c-axis has components of

$$\dot{\chi}_a = 0$$

$$\dot{\chi}_b = 0$$

$$\dot{\chi}_c = \dot{\chi}.$$

Collecting each component of angular velocity for the Euler angles, gives the total angular velocity about each of the body fixed axes a,b,c. The total rotational kinetic energy is

$$T = \frac{1}{2}(I_a\omega_a^2 + I_b\omega_b^2 + I_c\omega_c^2).$$

Since for an oblate symmetric top molecule (the case is similar for a prolate symmetric top) $I_a = I_b$, then the rotational kinetic energy becomes

$$T = \frac{1}{2}I_b\left(\dot{\phi}^2\sin^2\theta + \dot{\theta}^2\right) + \frac{1}{2}I_c\left(\dot{\phi}\cos\theta + \dot{\chi}\right)^2.$$

If the z-axis is taken to be along the total angular momentum L of the molecule then the components of the angular momentum about the molecule fixed axes are

$$L_a = I_a\omega_a = I_a\left(-\dot{\phi}\sin\theta\cos\chi + \dot{\theta}\sin\chi\right)$$

$$L_b = I_b\omega_b = I_b\left(\dot{\phi}\sin\theta\sin\chi + \dot{\theta}\cos\chi\right)$$

$$L_c = I_c\omega_c = I_c\left(\dot{\phi}\cos\theta + \dot{\chi}\right).$$

The components of angular momentum can also be obtained by calculating the components of the total angular momentum (which is along the space fixed z-axis) along each of the body fixed axes

$$L_a = -L\sin\theta\cos\chi$$

$$L_b = L\sin\theta\sin\chi$$

$$L_c = L\cos\theta.$$

Equating each of the components gives

$$I_a\left(-\dot{\phi}\sin\theta\cos\theta + \dot{\theta}\sin\chi\right) = -L\sin\theta\cos\chi$$

$$I_b\left(\dot{\phi}\sin\theta\sin\chi + \dot{\theta}\cos\chi\right) = L\sin\theta\sin\chi \qquad \text{(A.1.1)}$$

$$I_c\left(\dot{\phi}\cos\theta + \dot{\chi}\right) = L\cos\theta. \qquad \text{(A.1.2)}$$

The component of angular momentum along the line of nodes is $L_N = 0$ since this is perpendicular to the total angular momentum (or z-axis). However, the line of nodes angular momentum has components

$$L_N = L_a \sin\chi + L_b \cos\chi = I_a \dot{\theta}$$

once the expressions for L_a and L_b have been replaced. This then gives the result

$$\dot{\theta} = 0$$

since I_a is not equal to zero. This means that the angle between the body fixed c-axis and the total angular momentum is constant and hence the component of total angular momentum along the molecule symmetry axis is constant.

Substitution into Equation (A.1.1) gives

$$\dot{\phi} = \frac{L}{I_b}.$$

Hence, the body axis of the symmetric top molecule precesses about the total angular momentum at a constant angular velocity.

Again, substitution into Equation (A.1.2) gives

$$\dot{\chi} = \left(\frac{L}{I_c} - \frac{L}{I_b}\right)\cos\theta$$

which indicates that the molecule rotates about its own axis with a constant angular velocity [Zare 1988].

In an electric field there are two precessions: one the natural precession of the molecule fixed c-axis about the total angular momentum and the second one being the induced precession of the electric dipole about the electric field direction caused by the torque the field exerts on the dipole.

If the symmetric top molecule is precessing around the total angular momentum then there will be a resultant average total angular momentum L_c about the molecule c-axis. The rate of change of angular momentum is equal to the torque exerted by external forces which, for an electric dipole moment in an electric field is

$$\frac{dL_c}{dt} = \tau = \mu \times \varepsilon = \mu\varepsilon \sin\theta.$$

If θ is taken as $\pi/2$ then $\tau = \mu\varepsilon$.

The torque acts perpendicular to both the dipole moment and the electric field by the right hand rule. This means that the electric dipole will precess around the electric

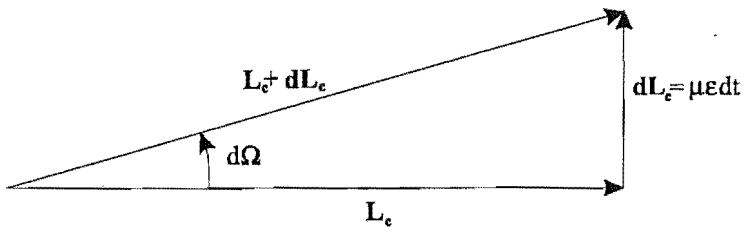

Figure A.1.1: The torque of an electric field on an electric dipole causes the dipole to rotate perpendicular to both the field and dipole direction.

field. Since $\theta = \pi/2$ the change in angular momentum will be perpendicular to the original L_c as shown in Figure A.1.1. The angular variation of the angular momentum vector in a small time is

$$d\Omega = \frac{dL_c}{L_c} = \frac{\mu\varepsilon dt}{L_c}$$

which gives the precession angular velocity of the electric dipole about the electric field, ω_ε, as

$$\omega_\varepsilon = \frac{\mu\varepsilon}{L_c} = \frac{\mu\varepsilon}{I_c\omega_c}.$$

Although this result has been obtained for $\theta = \pi/2$, the angular velocity remains unchanged when the c-axis is inclined at some arbitrary angle θ [Goldstein 1981].

References

Aitken 1994	Aitken, C.G., Blunt, D.A. and Harland, P.W., J.Chem.Phys., Vol 101, No 12, 11074, (1994).
Arshadi 1974	Arshadi, M.R. and Futrell, J.H., J.Chem.Phys., Vol 78, No 15, 1482, (1974).
Atkins 1995	Atkins, P.W., Physical Chemistry, fifth edition, Oxford University Press, Inc., (1986).
Bates 1974	Bates, D.R. and Bederson, B., Advances in Atomic and Molecular Physics, vol 10, Academic Press, Inc., (1974).
Becker 1956	Becker, E.W., Bier, K. and Henkes, W., Z.Phys., Vol 146, 333, (1956).
Bennewitz 1955	Bennewitz, H.G., Paul, W. and Schlier, Ch., Z.Phys., Vol 141, 6, (1955).
Beuhler 1966	Beuhler. Jr, R.J., Bernstein, R.B. and Kramer, K.H., J.Am.Chem.Soc., Vol 88, 5331, (1966).
Beulow 1987	Buelow, S., Radhakrishnan, G. and Wittig, C., J.Phys.Chem., Vol 91, 5409, (1987).
Bohme 1973	Bohme, D.K., Hemsworth, R.S. and Rundle, H.W., J.Chem.Phys., Vol 59, 77, (1973).
Bowering 1994	Bowering, N., Volkmer, M., Meier, C., Lieschke, J. and Fink, M., Z.Phys.D., Vol 30, 177, (1994).
Brauner 1989	Brauner, M., Briggs, J.S. and Klar, H., J.Phys.B: At.Mol.Opt.Phys., Vol 22, 2265, (1989).
Brooks 1966	Brooks, P.R. and Jones, E.M., J.Chem.Phys., Vol 45, No 9, 3449, (1966).
Brooks 1969a	Brooks, P.R., J.Chem.Phys., Vol 50, No 11, 5031, (1969).

Brooks 1969b — Brooks, P.R., Jones, E.M. and Smith, K., J.Chem.Phys., Vol 51, No 7, 3073, (1969).

Brooks 1973 — Brooks, P.R., Faraday.Discuss.Chem.Soc., Vol 55, 299, (1973).

Brooks 1976 — Brooks, P.R., Science., Vol 193, No 4247, 11, (1976).

Brooks 1979 — Brooks, P.R., McKillop, J.S. and Pippin, H.G., Chem.Phys.Letts., Vol 66, No 1, 144, (1979).

Brooks 1992 — Brooks, P.R., Harland, P.W., Phillips, L.F. and Carman. Jr, H.S., J.Phys.Chem., Vol 96, 1557, (1992).

Bulthuis 1991a — Bulthuis, J. and Stolte, S., J.Phys.Chem., Vol 95, 8180, (1991).

Bulthuis 1991b — Bulthuis, J., Milan, J.B., Janssen, M.H.M. and Stolte, S., J.Chem.Phys., Vol 94, No 11, 7181, (1991).

Cameron 1993 — Cameron, B.R., Ph.D. thesis, University of Canterbury, Christchurch, N.Z., November, (1993).

Cameron 1994 — Cameron, B.R., Aitken, C.G. and Harland, P.W., J.Chem.Soc.Faraday Trans., Vol 90, No 7, 935, (1994).

Carman 1986 — Carman, H.S., Harland, P.W. and Brooks, P.R., J.Phys.Chem., Vol 90, 944, (1986).

Ceyer 1979 — Ceyer, S.T., Tiedemann, P.W., Mahan, B.H. and Lee, Y.T., J.Chem.Phys., Vol 70, No 1, 14, (1979).

Choi 1985 — Choi, S.E. and Bernstein, R.B., J.Chem.Phys., Vol 83, No 9, 4463, (1985).

Choi 1986 — Choi, S.E. and Bernstein, R.B., J.Chem.Phys., Vol 85, No 1, 150, (1986).

Curtiss 1989 — Curtiss, T.J. and Bernstein, R.B., Chem.Phys.Letts., Vol 161, No 3, 212, (1989).

Curtiss 1990 — Curtiss, T.J., MacKay, R.S. and Bernstein, R.B., J.Chem.Phys., Vol 93, No 10, 7387, (1990).

Dibeler 1966 — Dibeler, V.H. and Reese, R.M., Advan.Mass Spectrometry, Vol 3, 471, (1966).

Duquette 1978 — Duquette, G., Ellis, T., Scoles, G., Watts, R.O. and Klein, M.L., J.Chem.Phys., Vol 68, 2544, (1978).

Ehrhardt 1986 — Ehrhardt, H., Jung, K., Knoth, G. and Schlemmer, P., Z.Phys.D., Vol 1, 3, (1986).

van den Ende 1982 — van den Ende, D., Stolte, S., Cross, J.B., Kwei, G.H. and Valentini, J.J., J.Chem.Phys., Vol 77, No 4, 2206, (1982).

van den Ende 1984 — van den Ende, D. and Stolte, S., Chem.Phys., Vol 89, 121, (1984).

Field 1957 — Field, F.H. and Franklin, J.L., Electron Impact Phenomena and the Properties of Gaseous Ions, Academic Press, Inc., (1957).

Fite 1958 — Fite, W.L. and Brackmann, R.T., Phys.Rev., Vol 112, 1141, (1958).

Fluendy 1973 — Fluendy, M.A.D. and Lawley, K.P., Chemical Applications of Molecular Beam Scattering, Chapman and Hall Ltd, (1973).

Friedrich 1991 — Friedrich, B., Pullman, D.P. and Herschbach, D.R., J.Phys.Chem., Vol 95, 8118, (1991).

Gandhi 1986 — Gandhi, S.R., Curtiss, T.J., Xu, Q.X., Choi, S.E. and Bernstein, R.B., Chem.Phys.Letts., Vol 132, No 1, 6, (1986).

Gandhi 1987a — Gandhi, S.R., Xu, Q.X., Curtiss, T.J. and Bernstein, R.B., J.Phys.Chem., Vol 91, 5437, (1987).

Gandhi 1987b — Gandhi, S.R., Curtiss, T.J. and Bernstein. R.B., Phys.Rev.Letts., Vol 59, No 26, 2951, (1987).

Gandhi 1988 — Gandhi, S.R. and Bernstein, R.B., Z.Phys.D - Atoms, Molecules and Clusters., Vol 10, 179, (1988).

Goldstein 1981 — Goldstein, H., Classical Mechanics, second edition, Addison-Wesley Publishing Company, Inc., (1981).

Harland 1989 — Harland, P.W., Carman. Jr, H.S., Phillips, L.F. and Brooks, P.R., J.Chem.Phys., Vol 90, No 9, 5201, (1989).

Harland 1990 — Harland, P.W., Carman. Jr, H.S., Phillips, L.F. and Brooks, P.R., J.Chem.Phys., Vol 93, No 2, 1089, (1990).

Harland 1991 — Harland, P.W., Carman. Jr, H.S., Phillips, L.F. and Brooks, P.R., J.Phys.Chem., Vol 95, 8137, (1991).

Harland 1995 — Harland, P.W., Private Communication, (1995).

Herschbach 1961 — Herschbach, D.R., Kwei, G.H. and Norris, J.A., J.Chem.Phys., Vol 34, 1842, (1961).

Hiraoka 1988 — Hiraoka, K., Nakajima, G. and Shoda, S., Chem.Phys.Letts., Vol 146, No 6, 535, (1988).

Hoffmeister 1987 — Hoffmeister, M., Schleysing, R. and Loesch, H., J.Phys.Chem., Vol 91, 5441, (1987).

Illies 1987 — Illies, A.J., McKee, M.L. and Schlegal, H.B., J.Chem.Phys., Vol 91, No 13, 3489, (1987).

Illies 1988 — Illies, A.J., J.Phys.Chem., Vol 92, No 10, 2889, (1988).

Jalink 1986a — Jalink, H., Harren, F., van den Ende, D. and Stolte, S., Chem.Phys., Vol 108, 391, (1986).

Jalink 1986b — Jalink, H., Parker, D.H. and Stolte, S., J.Chem.Phys., Vol 85, No 9, 5372, (1986).

Janssen 1991 — Janssen, M.H.M., Parker, D.H. and Stolte, S., J.Phys.Chem., Vol 95, No 21, 8142, (1991).

Johnston 1940 — Johnston, H.L. and McCloskey, K.E., J.Phys.Chem., Vol 44, 1038, (1940).

Jones 1970 — Jones, E.M. and Brooks, P.R., J.Chem.Phys., Vol 53, No 1, 55, (1970).

Jones 1978 — Jones, G.G. and Taylor, J.W., J.Chem.Phys., Vol 68, No 4, 1768, (1978).

Jones 1993 — Jones, S., Madison, D.H., Franz, A. and Altick, P.L., Phys.Rev.A., Vol 48, No 1, R22, (1993).

Jouvet 1987 — Jouvet, C., Boivineau, M., Duval, M.C. and Soep, B., J.Phys.Chem., Vol 91, 5416, (1987).

Kaesdorf 1985 — Kaesdorf, S., Schonhense, G. and Heinzmann, U., Phys.Rev.Letts., Vol 54, No 9, 885, (1985).

Kamke 1989 — Kamke, B., Kamke, W., Herrmann, R. and Hertel, I.V., Z.Phys.D., Vol 11, 153, (1989).

Kantrowitz 1951 — Kantrowitz, A. and Grey, J., Rev.Sci.Instrum., Vol 22, No 5, 328, (1951).

Karny 1978 — Karny, Z., Estler, R.C. and Zare, R.N., J.Chem.Phys., Vol 69, No 11, 5199, (1978).

Kasai 1989 — Kasai, T., Che, D.C., Ohashi, K. and Kuwata, K., Chem.Phys.Letts., Vol 163, No 2-3, 246, (1989).

Kasai 1993 — Kasai, T., Matsunami, T., Fukawa, T., Ohoyama, H. and Kuwata, K., Phys.Rev.Letts., Vol 70, No 25, 3864, (1993).

Keese 1986 — Keese, R.G. and Castleman, A.W., J.Phys.Chem.Ref.Data., Vol 15, 1011, (1986).

Kiser 1965 — Kiser, R.W., Introduction to Mass Spectrometry and its Applications, Prentice-Hall, (1965).

Kistiakowsky 1951 — Kistiakowsky, G.B. and Slichter, W.P., Rev.Sci.Instrum., Vol 22, No 5, 333, (1951).

Klots 1978 — Klots, C.E. and Compton, R.N., J.Chem.Phys., Vol 61, No 4, 1636, (1978).

Kramer 1965 — Kramer, K.H. and Bernstein, R.B., J.Chem.Phys., Vol 42, No 2, 767, (1965).

Kuipers 1988 — Kuipers, E.W., Tenner, M.G., Kleyn, A.W. and Stolte, S., Nature., Vol 334, 420, (1988).

Kuipers 1989 — Kuipers, E.W., Tenner, M.G., Kleyn, A.W. and Stolte, S., Phys.Rev.Letts., Vol 62, No 18, 2152, (1989).

Lampe 1957 — Lampe, F.W., Franklin, J.L. and Field, F.H., J.Am.Chem.Soc., Vol 79, 6129, (1957).

Levine 1986 — Levine, R.D. and Bernstein, R.B., Chem.Phys.Letts., Vol 132, No 1, 11, (1986).

Lias 1980 — Lias, S.G., Shold, D.M. and Ausloos, P., J.Am.Chem.Soc., Vol 102, 2540, (1980).

Linn 1981 — Linn, S.H. and Ng, C.Y., J.Chem.Phys., Vol 75, No 10, 4921, (1981).

Loesch 1990 — Loesch, H.J. and Remscheid, A., J.Chem.Phys., Vol 93, No 7, 4779, (1990).

Loesch 1991 — Loesch, H.J. and Remscheid, A., J.Phys.Chem., Vol 95, 8194, (1991).

Loesch 1992 — Loesch, H.J. and Moller, J., J.Chem.Phys., Vol 97, No 12, 9016, (1992).

Magee 1940 — Magee, J.L., J.Chem.Phys., Vol 8, 687, (1940).

Maltz 1972 — Maltz, C., Weinstein, N.D. and Herschbach, D.R., Mol.Phys., Vol 24, No 1, 133, (1972).

Marcelin 1975 — Marcelin, G. and Brooks, P.R., J.Am.Chem.Soc., Vol 97, No 7, 1710, (1975).

March 1989 — March, R.E. and Hughes, R.J., Quadrupole Storage Mass Spectrometry, John Wiley & Sons, Inc., (1989).

Massey 1969 — Massey, H.S.W., Burhop, E.H.S. and Gilbody, H.B., Electronic and Ionic Impact Phenomena, second edition, vol II, Oxford University Press, Inc., (1969).

Mautner 1977 — Mautner, M. and Field, F.H., J.Chem.Phys., Vol 66, No 10, 4527, (1977).

McDowell 1963 — McDowell, C.A., Mass Spectrometry, McGraw-Hill, New York, (1963).

McKee 1990 — McKee, M.L., Chem.Phys.Letts., Vol 165, No 2, 265, (1990).

Meier 1994 — Meier, C., Volkmer, M., Lieschke, J., Fink, M. and Bowering, N., Z.Phys.D., Vol 30, 183, (1994).

Ohashi 1988 — Ohashi, K., Kasai, T. and Kuwata, K., J.Phys.Chem., Vol 92, No 21, 5954, (1988).

Ohoyama 1987 — Ohoyama, H., Kasai, T., Ohashi, K. and Kuwata, K., Chem.Phys.Letts., Vol 136, No 3-4, 236, (1987).

Parker 1987 — Parker, D.H., Jalink, H. and Stolte, S., J.Phys.Chem., Vol 91, 5427, (1987).

Parker 1989 — Parker, D.H. and Bernstein, R.B., Annu.Rev.Phys.Chem., Vol 40, 561, (1989).

Payzant 1973 — Payzant, J.D., Cunningham, A.J. and Kebarle, P., Can.J.Chem., Vol 51, 3242, (1973).

Polanyi 1988 — Polanyi, J.C. and Williams, R.J., J.Chem.Phys., Vol 88, No 5, 3363, (1988).

Ramsey 1956 — Ramsey, N.F., Molecular Beams, Clarendon Press, (1956).

Rettner 1982 — Rettner, C.T. and Zare, R.N., J.Chem.Phys., Vol 77, No 5, 2416, (1982).

Rosenstock 1977 — Rosenstock, H.M., Draxl, K., Steiner, B.W. and Herron, J.T., J.Phys.Chem.Ref.Data 6,Suppl.1., Vol 70, (1977).

Scherer 1987 — Scherer, N.F., Khundkar, L.R., Bernstein, R.B. and Zewail, A.H., J.Chem.Phys., Vol 87, No 2, 1451, (1987).

Scoles 1988 — Scoles, G., Atomic and Molecular Beam Methods, Volume 1, Oxford University Press, Inc., (1988).

Searles 1968 — Searles, S.K. and Kebarle, P., J.Phys.Chem., Vol 72, 742, (1968).

Shirley 1963 — Shirley, J.H., J.Chem.Phys., Vol 38, No 12, 2896, (1963).

Srivastava 1988 — Srivastava, M.K. and Sharma, S., Phys.Rev.A., Vol 37, No 2, 628, (1988).

Stephan 1982a — Stephan, K., Futrell, J.H., Peterson, K.I., Castleman Jr, A.W. and Mark, T.D., J.Chem.Phys., Vol 77, No 5, 2408, (1982).

Stephan 1982b — Stephan, K., Futrell, J.H., Peterson, K.I., Castleman Jr, A.W., Wagner, H.E., Djuric, N. and Mark, T.D., J.Mass Spec. and Ion Phys., Vol 44, 167, (1982).

Stolte 1972 — Stolte, S., Reuss, J. and Schwartz, H.L., Physica., Vol 57, 254, (1972).

Stolte 1973 — Stolte, S., Reuss, J. and Schwartz, H.L., Physica., Vol 66, 211, (1973).

Stolte 1982 — Stolte, S., Chakravorty, K.K., Bernstein, R.B. and Parker, D.H., Chem.Phys., Vol 71, 353, (1982).

Tate 1932 — Tate, J.T. and Smith, P.T., Phys.Rev., Vol 39, 270, (1932).

Tenner 1988 — Tenner, M.G., Kuipers, E.W., Kleyn, A.W. and Stolte, S., J.Chem.Phys., Vol 89, No 10, 6552, (1988).

Townes 1955 — Townes, C.H. and Schawlow, A.L., Microwave Spectroscopy, McGraw-Hill Book Company, Inc., (1955).

Volkmer 1992 — Volkmer, M., Meier, Ch., Mihill, A., Fink, M. and Bowering, N., Phys.Rev.Letts., Vol 68, No 15, 2289, (1992).

de Vries 1982 — de Vries, M.S., Srdanov, V.I., Hanrahan, C.P. and Martin, R.M., J.Chem.Phys., Vol 77, No 5, 2688, (1982).

de Vries 1983 — de Vries, M.S., Srdanov, V.I., Hanrahan, C.P. and Martin, R.M., J.Chem.Phys., Vol 78, No 9, 5582, (1983).

Wei 1990a — Wei, S., Tzeng, W.B. and Castleman Jr, A.W., J.Chem.Phys., Vol 93, No 4, 2506, (1990).

Wei 1990b — Wei, S., Tzeng, W.B. and Castleman Jr, A.W., J.Chem.Phys., Vol 92, No 1, 332, (1990).

Wincel 1972 — Wincel, H., Int.J.Mass Spectrom.Ion.Phys., Vol 9, 267, (1972).

Xing 1994 — Xing, G., Kasai, T. and Brooks, P.R., J.Am.Chem.Soc., Vol 116, No 16, 7421, (1994).

Xu 1988 — Xu, Q.X., Jung, K.H. and Bernstein, R.B., J.Chem.Phys., Vol 89, No 4, 2099, (1988).

Xu 1989 Xu, Q.X., Quesada, M.A., Jung, K.H., MacKay, R.S. and Bernstein, R.B., J.Chem.Phys., Vol 91, No 6, 3477, (1989).

Zare 1988 Zare, R.N., Angular Momentum, John Wiley & Sons, Inc., (1988).